

**Structural, magnetic and dielectric studies on  $Gd_{1-x}Y_xMnO_3$**

*By*

**R M Sarguna**

**Enrolment No: PHYS02200704011**

**Indira Gandhi Centre for Atomic Research, Kalpakkam, India**

*A thesis submitted to the Board of Studies in Physical Sciences*

*In partial fulfillment of requirements*

*for the Degree of*

**DOCTOR OF PHILOSOPHY**

*of*

**HOMI BHABHA NATIONAL INSTITUTE, MUMBAI**



**August, 2014**

# HomiBhabha National Institute

## Recommendations of the Viva Voce Committee

As members of the Viva Voce Committee, we certify that we have read the dissertation prepared by R M Sarguna entitled “Structural, magnetic and dielectric studies on  $Gd_{1-x}Y_xMnO_3$ ” and recommend that it may be accepted as fulfilling the thesis requirement for the award of Degree of Doctor of Philosophy.

---

Chairman –Dr. C.S.Sundar

**Date:**

---

Guide / Convener –Dr. V. Sridharan

**Date:**

---

External examiner

**Date:**

---

Member 1- Dr. N. Subramanian

**Date:**

---

Member 2–Dr. P. Ch.Sahu

**Date:**

---

Member 3- Dr. Sharat Chandra

**Date:**

---

Final approval and acceptance of this thesis is contingent upon the candidate’s submission of the final copies of the thesis to HBNI.

I hereby certify that I have read this thesis prepared under my/our direction and recommend that it may be accepted as fulfilling the thesis requirement.

**Date:**

**Place:** IGCAR, Kalpakkam

## **CERTIFICATE**

I hereby certify that I have read this dissertation prepared under my direction and recommend that it may be accepted as fulfilling the dissertation requirement.

**Date:**

**Place:**

**(Dr. V. Sridharan)**

## **STATEMENT BY AUTHOR**

This dissertation has been submitted in partial fulfillment of requirements for an advanced degree at HomiBhabha National Institute (HBNI) and is deposited in the Library to be made available to borrowers under rules of the HBNI.

Brief quotations from this dissertation are allowable without special permission, provided that accurate acknowledgement of source is made. Requests for permission for extended quotation from or reproduction of this manuscript in whole or in part may be granted by the Competent Authority of HBNI when in his or her judgment the proposed use of the material is in the interests of scholarship. In all other instances, however, permission must be obtained from the author.

**(R M Sarguna)**

## **DECLARATION**

I, hereby declare that the investigation presented in the thesis has been carried out by me. The work is original and has not been submitted earlier as a whole or in part for a degree / diploma at this or any other Institution / University.

**(R M Sarguna)**

## List of Publications arising from the thesis

### Journal

#### Publication:

##### A. Journal publication:

1. Structural, magnetic and dielectric studies on  $Gd_{0.7}Y_{0.3}MnO_3$   
R.M. Sarguna, V. Sridharan, S. Shanmukrao, V. Ganesan, S. Bhardwaj, A. M. Awasthi, M. D. Mukadam, S.M. Yusuf, A.K. Sinha and N. Subramanian.  
*J. Phys.: Condens. Matter.* **26** 345901(2014).
2. Dielectric relaxation studies in  $Gd_{1-x}Y_xMnO_3$  ( $x = 0.2, 0.3$  &  $0.4$ ) rare earth perovskite  
R.M. Sarguna, V. Sridharan, S. Bhardwaj, A. M. Awasthi, and N. Subramanian.  
To be submitted.
3. Raman investigations of spin-phonon coupling in multiferroic  $Gd_{1-x}Y_xMnO_3$  ( $x = 0.2, 0.3$  &  $0.4$ )  
R.M. Sarguna, V. Sridharan, V. Sivasubramanian, T.R. Ravinderan and N. Subramanian.  
To be submitted

##### B. Conference Publications:

1. Structural, dielectric and magnetic studies on Y-substituted  $GdMnO_3$   
R. M. Sarguna, V. Sridharan, Suresh Bhardwaj, A. M. Awasthi, M. D. Mukadam, S. M. Yusuf and N. Subramanian  
IUMRS-ICA-2013, Dec16-20, 2014
2. Growth of multiferroic  $Gd_{1-x}Y_xMnO_3$  single crystal by optical floating zone technique.  
R M Sarguna, S Ganesamoorthy, V Sridharan and N Subramanian  
ICMCT-2014, March10<sup>th</sup>-12<sup>th</sup> 2014, held at VIT.

##### Journal Publications (Not related to thesis).

1. Raman scattering from La-substituted  $BiFeO_3$ - $PbTiO_3$   
K.K.Mishra, V. Sivasubramanian, R. M. Sarguna, T. R. Ravindran, A. K. Arora.  
*J. Solid State Chem.* **184**2381 (2011).
2. x-T phase diagram of La-substituted  $BiFeO_3$ - $PbTiO_3$   
K. K. Mishra, R. M. Sarguna, shabana khan and A. K. Arora.  
*AIP ADVANCES* **103**2126(2011).
3. Kohler's rule in  $Ba_{(1-x)}K_{(x)}Fe_2As_2$ .  
N. Ghosh, A. Bharathi, A.T. Satya, S. Sharma, Awadesh Mani, R.M. Sarguna, D. Sornadurai, V.S. Sastry and C.S. Sundar.  
*Solid State Commun.* **150** 1940 (2010).
4. The effects of strain, current, and magnetic field on superconductivity in  $Pr_{0.5}Ca_{0.5}MnO_3/YBa_2Cu_3O_7/Pr_{0.5}Ca_{0.5}MnO_3$  trilayer.  
Dipak Kumar Baisnab, M. P. Janawadkar, Shilpam Sharma, R. M. Sarguna, L. S. Vaidhyathan and A. Bharathi, *J. Appl. Phys.* **113**, 113902 (2013).

(R M Sarguna)

## ACKNOWLEDGEMENTS

The work presented in this thesis would not have been possible without help of many people who were always there when I needed them the most. I take this opportunity to acknowledge them and extend my sincere gratitude for helping me make this Ph.D. thesis a possibility. First and foremost, I would like to express my deep and sincere gratitude to my guide, Dr. V.Sridharan. He has been a true mentor during this period. I express my gratitude to Mr.V. Shankar sastry.I especially thank Dr. C. S. Sundar for his support and encouragements. I express my gratitude to Dr. N. Subramanian, Dr. P. Ch. Sahu and Dr. Sharat Chandra. I would like to thank the MSG director Mr. M. P. Janwadkar, the Center director Dr. P. R. Vasudeva Rao and CMPD division head Dr. A. Bharathifor their support. I would like to thank my collaborators Dr. A. M. Awasthi, Dr. V. Ganeasn, Dr. A.K. Sinha, Dr. S. M. Yusuf, Dr. V. Sivasubramaian, Dr. M. D. Mukudam, and S. Shanmukharao.I would like to thank Dr. S. Ganeshamoorthy and Dr. G. Raghavan for going through my thesis and providing valuable suggestions. I would like to thank my section members, Dr. D. Sornadurai, Dr. S. Kalavathi, Dr.R. Nithya for their help during this period. I have got a lot of help from my friends S. Sanjay Kumar, Dr. Dipak kumar Biasnab, Dr. V. Srihari and Mr. Meenakshi Sundaram. I would like to especially thank S. Sanjay kumar for going through my thesis.I express my heartfelt thanks to my wife Sharmila for her constant support. I would like to express my heartiest gratitude to my parents.

(R M Sarguna)

# CONTENTS

<b>TITLE</b>	<b>Page No.</b>
List of Publications arising from the thesis	v
Acknowledgements	vi
SYNOPSIS	ix
List of Figures	x
List of Tables	xii
<b>Chapter 1</b>	
INTRODUCTION	1
1.1 Introduction	1
1.2 RMnO <sub>3</sub> structure, magnetic and multiferroic properties	4
1.2.1 TbMnO <sub>3</sub>	9
1.2.2 DyMnO <sub>3</sub>	10
1.2.3Eu <sub>1-x</sub> Y <sub>x</sub> MnO <sub>3</sub>	11
1.2.4Sm <sub>1-x</sub> Y <sub>x</sub> MnO <sub>3</sub>	12
1.3 Motivation for the present study	12
References	15
<b>Chapter 2</b>	
Experimental techniques, data analysis and calculations	19
2.1 Sample preparation	19
2.2 Room temperature powder X-ray diffraction (XRD)	19
2.3 Scanning electron microscopy and energy-dispersive X-ray analysis	21
2.4 Magnetisation measurements	22
2.5 Specific heat	22
2.6 Dielectric spectroscopy	23
2.7 Low temperature XRD	24
2.8 Raman spectroscopy	26
2.9 Band structure calculation methodology	26
2.10 Rietveld refinement by GSAS	29
References	33

<b>Chapter 3</b>	
Structural magnetisation and specific heat studies on $Gd_{1-x}Y_xMnO_3$	35
3.1 Introduction	35
3.2 Sample synthesis	36
3.3 X-ray diffraction and structural studies	37
3.4 Thermomagnetisation and M-H studies	41
3.5 Specific heat studies	45
3.6 Conclusions	47
References	49
<b>Chapter 4</b>	
Dielectric and powder XRD studies at low temperature	50
4.1 Introduction	50
4.2 Dielectric spectroscopy studies	51
4.3 Low temperature XRD studies	61
4.4. Normal and inverse magneto-caloric effect	67
4.5 Conclusion	73
References	75
<b>Chapter 5</b>	
Raman studies and band structure calculation on $Gd_{1-x}Y_xMnO_3$	77
5.1 Introduction	77
5.2 Room temperature Raman studies	78
5.2.1 Low temperature Raman studies	82
5.3 Band structure and phonon density calculation	88
5.4 Conclusion	96
References	98
<b>Chapter 6</b>	
Summary and scope for future work	100
Scope for future research	104

## SYNOPSIS

Rare earth manganites exhibit a variety of interesting physical properties which can be tuned by varying the structural parameters. One such property is multiferroic, where ferroic orders coexist. Such materials have innumerable applications and open up new area for research. This thesis summarizes experimental effort undertaken towards understanding the structural, dielectric, magnetic and multiferroic properties of  $Gd_{1-x}Y_xMnO_3$  solid solution ( $x = 0.2, 0.3 \text{ \& } 0.4$ ) whose physical properties can be tuned by varying the average rare earth ionic radius. The details of the chapters are given below.

**Chapter 1:** This chapter provides a general introduction to multiferroic materials and in particular to rare earth manganites. A review of the current state of knowledge in various  $RMnO_3$  systems is presented. The variation of structural parameters with different rare earth ions and their effect on the magnetic and dielectric nature have been outlined. The chapter ends with the motivation for the present work.

**Chapter 2:** This chapter deals with the various experimental techniques used to study the physical properties.

**Chapter 3:** This chapter deals with sample synthesis, room temperature X-ray diffraction studies to find the structural parameter and magnetic measurements.

**Chapter 4:** This chapter discusses the dielectric properties, magneto-elastic properties and normal and inverse magneto-caloric effects of  $Gd_{1-x}Y_xMnO_3$ .

**Chapter 5:** This chapter discusses spin-phonon coupling present in the system by studying the Raman modes as function of temperature and composition. The phonon density of states have been calculated and compared with the experimental results.

**Chapter 6:** The thesis concludes by summarising the work done and giving direction for future scope of work.

List of figures:

Figure.1.1	Figure showing the various exchange integral a) inplane, b) inplane as well as interplane for $Pbnm$ structure $J_{ab}$ is FM while $J_{aa}$ , $J_{bb}$ , and $J_{cc}$ are AFM.	6
Figure.1.2	Phase diagram of $RMnO_3$ as a function of Mn-O-Mn bond angle.	7
Figure.3.1	SEM micrographs of $Gd_{1-x}Y_xMnO_3$ for a) $x=0$ , b) $x=0.2$ , c) $x=0.3$ and d) $x=0.4$ .	37
Figure.3.2	Room temperature XRD patterns of $Gd_{1-x}Y_xMnO_3$ ( $x=0.2, 0.3$ and $0.4$ ). The diffraction patterns are vertically shifted for clarity	38
Figure.3.3	Measured X-ray diffraction pattern of $Gd_{0.7}Y_{0.3}MnO_3$ along with fit ( $x$ ) - measured pattern, (—) - Calculated pattern; (—) - difference ( ) - position of Bragg reflection.	39
Figure.3.4	Variation in the lattice parameters $a$ , $b$ , $c$ and unit cell volume with Y concentration ( $x$ ). Lines are drawn as a guide to the eye	40
Figure.3.5	Figure showing the FC and ZFC curves and inset showing the fitting with Curie-Weiss law for a) $x=0.2$ , b) $x=0.3$ , c) $x=0.4$ and d) effective moment for all composition.	42
Figure.3.6	M-H curves at 20, 10 and 5K for a) $x=0.2$ , b) $x=0.3$ , c) $x=0.4$ and d) M-H curves for all composition at 5K.	44
Figure.3.7	$C_p/T$ vs T plot for $Gd_{1-x}Y_xMnO_3$ $x = 0.2, 0.3$ & $0.4$ .	45
Figure.3.8	$C_p/T$ vs. T plot for $Gd_{0.7}Y_{0.3}MnO_3$ with the inset showing a feeble anomaly at 18K attributed to sinusoidal to cycloidal anti ferromagnetic transition of $Mn^{3+}$ sublattice.	46
Figure.4.1	Variation of real part of dielectric permittivity with temperature $\epsilon'(T)$ for $Gd_{1-x}Y_xMnO_3$ : a) $x=0.2$ , b) $x=0.3$ c) $x=0.4$ for various frequencies, d) comparison of $\epsilon'(T)$ measured at 10 kHz for $x=0.2, 0.3$ and $0.4$ . Vertical line corresponds to magnetic transition temperatures of $Mn^{3+}$ and $Gd^{3+}$ sublattice.	52
Figure.4.2	Variation of imaginary part of dielectric permittivity with temperature $\epsilon''(T)$ for $Gd_{1-x}Y_xMnO_3$ : a) $x=0.2$ , b) $x=0.3$ c) $x=0.4$ for various frequencies d) comparison of $\epsilon''(T)$ measured at 10 kHz for $x=0.2, 0.3$ and $0.4$ . Vertical lines correspond to magnetic transition temperatures of $Mn^{3+}$ and $Gd^{3+}$ sublattice.	54
Figure.4.3	Variation of $\epsilon''$ with temperature at different frequencies. Curve fitting to estimate additional anomaly in $\epsilon''(T)$ of $Gd_{0.7}Y_{0.3}MnO_3$ carried out with Debye model.	56
Figure.4.4	Variation of relaxation time $\ln(\tau)$ vs. $(1/T)$ for a) $x=0.2$ , b) $x=0.3$ and c) $x=0.4$ fitted to a Debye model. Corresponding activation energies $E_a$ are indicated.	57
Figure.4.5	Figure showing the variation of $\epsilon''(\omega)$ at different temperature for $Gd_{0.8}Y_{0.2}MnO_3$ .	59
Figure.4.6	Figure showing the fitting $\epsilon''(\omega)$ with both conductive and Cole-Cole function for $x=0.2$ at 23K.	60
Figure.4.7	Arrhenius representation of relaxation time variation as a function of temperature for $Gd_{1-x}Y_xMnO_3$ for $x=0.2, 0.3$ and $0.4$ .	61
Figure.4.8	Variation of dielectric strength for $Gd_{1-x}Y_xMnO_3$ ( $x = 0.2, 0.3$ & $0.4$ ).	62

Figure.4.9	Low temperature XRD pattern at different temperature for $Gd_{0.7}Y_{0.3}MnO_3$ recorded at Indus-2. The Be peaks are star marked.	63
Figure.4.10	Lattice parameter variation of $GdMnO_3$ as a function of temperature.	64
Figure.4.11	Lattice parameter variation of $Gd_{0.8}Y_{0.2}MnO_3$ as a function of temperature.	65
Figure.4.12	Lattice parameter variations of $Gd_{0.7}Y_{0.3}MnO_3$ as a function of temperature.	66
Figure.4.13	Cp/T vs. T plot for $Gd_{1-x}Y_xMnO_3$ a) $x=0.2$ , b) $x=0.3$ and c) $x=0.4$ .	69
Figure.4.14	Figure showing the variation of $\Delta T_{ad}$ and $\Delta S$ for $Gd_{1-x}Y_xMnO_3$ (a, b) $x=0.2$ , (c, d) $x=0.3$ and (e, f) $x=0.4$ respectively.	71
Figure.5.1	Raman spectrum of $Gd_{1-x}Y_xMnO_3$ ( $x=0, 0.2, 0.3$ & $0.4$ ) at room temperature depicting various modes.	79
Figure.5.2	Raman mode shift with bond angle variation for $Gd_{1-x}Y_xMnO_3$ ( $x=0, 0.2, 0.3$ & $0.4$ ).	81
Figure.5.3	Raman spectrum of $Gd_{1-x}Y_xMnO_3$ for a) $x=0$ , b) $x=0.2$ , c) $x=0.3$ & select few temperature. The patterns have been shifted for clarity.	82
Figure.5.4	Variation of Raman modes with temperature for $A_g(4)$ , $A_g(1)$ , $B_{2g}(3)$ , and $B_{2g}(1)$ for all the composition. Red curve shows the fitting of anharmonic equation.	83
Figure.5.5	Total Raman shift of the individual modes for different composition.	84
Figure.5.6	Total Raman shift between anharmonic extrapolated curve and experimental curve at 10K.	86
Figure.5.7	Variation of FWHM and their fitting (red curve) for $Gd_{1-x}Y_xMnO_3$ ( $x=0, 0.3$ and $0.4$ ).	87
Figure.5.8	Partial and total density of states of (a) $GdMnO_3$ , (b) Gd, (c) Mn and (d) O contribution to $GdMnO_3$ DOS, (e) $YMnO_3$ , (f) Y, (g) Mn and (h) O contribution to $YMnO_3$ DOS.	90
Figure.5.9	partial density of states of (a) $Gd_{0.25}Y_{0.75}MnO_3$ , (b) O contribution to $Gd_{0.25}Y_{0.75}MnO_3$ DOS, (c) $Gd_{0.5}Y_{0.5}MnO_3$ contribution towards $Gd_{0.5}Y_{0.5}MnO_3$ .	91
Figure.5.10	Total DOS of (a) Gd in $GdMnO_3$ , $Gd_{0.25}Y_{0.75}MnO_3$ and $Gd_{0.5}Y_{0.5}MnO_3$ , (b) Mn in $GdMnO_3$ , $Gd_{0.25}Y_{0.75}MnO_3$ , $Gd_{0.5}Y_{0.5}MnO_3$ and $YMnO_3$ , (c) Y in $YMnO_3$ , $Gd_{0.25}Y_{0.75}MnO_3$ and $Gd_{0.5}Y_{0.5}MnO_3$ and (d) O in $GdMnO_3$ , $Gd_{0.25}Y_{0.75}MnO_3$ , $Gd_{0.5}Y_{0.5}MnO_3$ and $YMnO_3$ .	91
Figure.5.11	Electronic band structures of (a) $GdMnO_3$ , (b) $Gd_{0.25}Y_{0.75}MnO_3$ , (c) $Gd_{0.5}Y_{0.5}MnO_3$ and (d) $YMnO_3$ .	92
Figure.5.12	The phonon dispersion curves for $GdMnO_3$ and $YMnO_3$ along the high symmetry direction.	95
Figure.5.13	Phonon density of states for $Gd_{1-x}Y_xMnO_3$ ( $0 \leq x \leq 1$ ).	95
Figure.5.14	Individual atomic contribution to the density of states for $GdMnO_3$ as calculated from VASP.	96

List of Tables:

Table 2.1	Details of the STOE Diffractometer.	20
Table 2.2	Table showing the various beam parameters of BL-12 ADXRD beamline.	24
Table 2.3	Interatomic potentials used for GULP calculation	28
Table 3.1	Estimated lattice parameters, bond angles, fractional co-ordinates of the atoms for $Gd_{1-x}Y_xMnO_3$ ( $x= 0.2, 0.3$ & $0.4$ ) in orthorhombic symmetry belonging to <i>Pbnm</i> space group.	41
Table 5.1	Table showing the various Raman modes and their association with lattice distortions.	80
Table 5.2	Lattice Parameters, atomic positions and Mn-O characteristics as obtained from the relaxed ground state configurations obtained from DFT. The fundamental band gaps and the magnetic moments per formula unit and for the individual atoms are also given. The table also shows the values of the bulk modulus and the static and high frequency dielectric constants obtained for the various compounds from the GULP lattice calculations.	93

# CHAPTER 1

## INTRODUCTION

### 1.1. Introduction

Magnetic and electric ordering in their varied forms has been extensively investigated resulting in numerous applications. There has been a constant pursuit to synthesize materials exhibiting both these forms of ordering, so that, one can be controlled through the other. This would obviously give rise to wide ranging applications. Materials exhibiting either magnetically induced electric polarisation or electrically induced magnetization are called magneto-electric materials. Magneto-electric effect was theoretically proposed by Dzyaloshinskii in 1959 [1]. The search for such materials should logically begin with systems possessing both ferroelectric and magnetic properties. Such materials are called multiferroics. According to the original definition by Hans Schmid [2], multiferroic materials combine two or more of the primary forms of ferroic order, *i.e.* ferromagnetism, ferroelectricity, ferroelasticity and ferrotoroidicity. In practice, most of the recent research has focused on materials that combine some form of magnetic order with ferroelectricity. Hence, the term multiferroics in its current usage is synonymous to magnetic ferroelectrics and magneto-electric materials. The first material reported to exhibit magneto-electric effects was antiferromagnetic  $\text{Cr}_2\text{O}_3$  [3, 4], which shows both magnetic field induced polarisation and electric field induced magnetization. The linear cross-coupling between these fields is given by the second rank magneto-electric susceptibility tensor - denoted in general by  $\alpha$ . Brown *et al.* [5] proposed that the magneto-electric coefficient  $\alpha$  is restricted by the values of electric and magnetic susceptibility of the materials.

$$\alpha^2 < \chi_e \chi_m$$

Where  $\chi_e$  and  $\chi_m$  are the electric and magnetic susceptibility tensors. Hence, it is seen that a strong coupling is expected for ferromagnetic and ferroelectric materials in general. However, only a few compounds are seen to possess both types of ordering. The first ferromagnetic-ferroelectric material to be discovered was nickel iodine boracite,  $\text{Ni}_3\text{B}_7\text{O}_{13}\text{I}$  [6]. This was followed by synthesis of multiferroics by partially replacing  $d^0$ -B cations in ferroelectric Perovskite  $\text{ABO}_3$  oxides by paramagnetic ions. Theoretical studies have shown that the usual atomic-level mechanisms driving ferromagnetism and ferroelectricity are mutually exclusive, because they require completely empty and partially filled transition metal orbitals, respectively. This led researchers to look in new directions. As only a few materials were available which showed both types of ordering and as most of the materials studied have a very low value of  $\alpha$ , potential applications were extremely limited. This fact led to a decline of research in this area. The recent interest in the field of multiferroics was revived by Hill in a report [7] which addressed the issue as to why there was a paucity of multiferroic materials. Hill discussed the allowed structural, physical and electronic restrictions and suggested a class of materials that should be studied further. Amongst these, is a class of rare earths and their related manganites.  $\text{YMnO}_3$  and  $\text{BiMnO}_3$  were discussed as typical examples. Experimentally, the reporting of enhanced value of polarization in thin films of  $\text{BiFeO}_3$  by Wang *et al.* [8] and discovery of novel class of multiferroics like  $\text{TbMnO}_3$  [9] and  $\text{TbMn}_2\text{O}_5$  [10] rekindled research in multiferroics. It was also shown that in the latter class of materials, the direction of spontaneous polarization could be flipped by the application of a magnetic field. These three materials are being extensively investigated to test various theoretical aspects of multiferroics.

Multiferroic materials are generally classified into two groups: type I and type II [11]. In type-I multiferroics, the origins of ferroelectricity and magnetism are different and they largely

appear to be independent of one another. Generally, for this class of materials, the ferroelectric transition occurs at higher temperatures than the magnetic transition. Though these materials exhibit enhanced polarisation, the coupling is generally rather weak. BiFeO<sub>3</sub> is a classic example of type-I multiferroic materials for which both magnetic and ferroelectric transitions occur above the room temperature ( $T_{FE} \sim 1100\text{K}$  and  $T_N \sim 643\text{K}$ ) [12]. For the type-II multiferroics, the magnetic and ferroelectric transition temperatures are close by and occur at low temperatures, typically less than 50 K. More importantly, the magnetic transition of these compounds drives the ferroelectric ordering and the coupling between the ferroic orders is strong. Though the value of polarisation is lower compared to type-I, magnetic fields have a better control over the ferroic properties in type-II systems. In some systems, the spontaneous polarisation direction can be reversed by the application of a magnetic field. The archetypal example of type-II multiferroics are TbMnO<sub>3</sub> and TbMn<sub>2</sub>O<sub>5</sub>. In these materials, the onset of collinear to nonlinear magnetic ordering, incommensurate with the lattice period, leads to spontaneous polarization. For this reason, they are called improper ferroelectrics. Type-II class of multiferroics are of special interest as they are strongly correlated systems and ferroic orders can be better controlled. Further, different magnetic structures like spiral and collinear gives rise to spontaneous polarisation. The rare earth Perovskite manganites have rich magnetic and electric phases and are strongly correlated systems. As they are considered to be potential candidates for multiferroic research, much of research effort is devoted to them. TbMnO<sub>3</sub> one of the seminal materials exhibiting a strong coupling falls in this class of materials.

## 1.2. RMnO<sub>3</sub> Structural, Magnetic and Multiferroic Properties

Rare earth manganites RMnO<sub>3</sub> have been studied for a long time in relation to colossal magnetoresistance. The structural as well as magnetic properties of rare earth Perovskite manganites can be easily modified by varying the ionic radius of the R-Rare earth ion. For example, substitution of trivalent R with divalent cations like Ca and Sr result in magnetic phases like paramagnetic, ferromagnetic insulator and metals, canted antiferromagnetic insulator as well as structural transitions related to cubic, tetragonal, orthorhombic, rhombohedral and monoclinic symmetry [13, 14, 15, 16, 17, 18]. These investigations have greatly clarified the nature of changes that occur in the magnetic and the structural ground state of the RMnO<sub>3</sub> systems, especially LaMnO<sub>3</sub>. RMnO<sub>3</sub> with larger rare earth (R = La-Dy) ions have an orthorhombic structure. As the rare earth ionic radius decreases, the crystal structure changes from orthorhombic to hexagonal with R = Ho-Lu exhibiting hexagonal symmetry. As the rare earth ionic radius decreases, the tolerance factor of the ideal perovskite structure deviates from unity. This results in a mismatch of the A-O and B-O equilibrium bond lengths of an ideal cubic perovskite ABO<sub>3</sub> type structure and the tolerance factor  $t$  starts decreasing as:

$$t = \frac{(r_A + r_O)}{\sqrt{2}(r_B + r_O)}$$

The value of  $t$  at room-temperature and ambient-pressure is calculated from the sums of the empirical ionic radii given in tables, e.g., those of Shannon and Prewitt [19]. Reduction of  $t$  results in the B-O bonds being subject to a compression and the A-O bonds to tension. These internal stresses are relieved by a cooperative rotation of the BO<sub>6</sub> octahedra, leading to an orthorhombic GdFeO<sub>3</sub> type distortion. This changes the ideal Perovskite structure from cubic to

orthorhombic. This increased cooperative bending with decreasing rare earth ionic radii results in a reduction of the Mn-O-Mn bond angle. In RMnO<sub>3</sub> perovskite, the Mn<sup>3+</sup> ion sits in an octahedral site in high-spin configuration  $t_{2g}^3 e_g^1$  and a Jahn-Teller distortion of the octahedron lifts the two fold energy degeneracy of the  $e_g$  level. In Perovskite RMnO<sub>3</sub> systems, the cooperative Jahn-Teller distortion of the MnO<sub>6</sub> octahedra results in long range ordering of the occupied  $e_g$  orbitals [20, 21] within the (001) planes of an *O* orthorhombic structure. This alternating ordering of the orbital produces an *O'* orthorhombic structure with  $c/a < \sqrt{2}$  [22] with *Pbnm* symmetry. As the rare earth ionic radius is decreased further, the crystal structure changes from orthorhombic to hexagonal symmetry.

Concomitant with these phenomena, the magnetic structure of the RMnO<sub>3</sub> changes from A-type anti ferromagnetic for larger R [R = La-Gd] [14, 23] to E-type antiferromagnetic for smaller R [R = Ho-Lu] through an incommensurate long wavelength magnetic structure for intermediate R (R = Tb, Dy). The A-type antiferromagnetic [14] structure in larger rare earth ions is stabilized by the alternate orbital ordering of the  $e_g$  orbitals. In the case of RMnO<sub>3</sub>, the essential magnetic exchange path is between adjacent 3d orbitals of Mn<sup>3+</sup> mediated by the 2p-orbitals of O<sup>2-</sup>. Electron hopping results in a ferromagnetic interaction between the nearest neighbour (NN)  $e_g$  spins among the *ab* plane and antiferromagnetic interaction among the nearest neighbour  $t_{2g}$  spins. The magnitude of electron transfer among the  $e_g$  orbitals between the nearest neighbour (NN) Mn<sup>3+</sup> ions in the *ab* plane becomes larger than that in the *c* direction. Thus, the ferromagnetic interaction is stronger in the *ab* plane while it is weaker in the *c* direction where the anti ferromagnetic interaction is stronger [24]. The competition between this anisotropic ferromagnetic interaction and the isotropic antiferromagnetic interaction  $J_{AF}^{t_{2g}}$  stabilizes the A-type AFM. As the rare earth ionic radius decreases, it results in increased orthorhombic

distortion, which reduces the Mn-O-Mn bond angle. This results in variation of the ferromagnetic and anti ferromagnetic interaction which progressively reduces the Neel temperature of the  $\text{Mn}^{3+}$  sublattice. The decrease of Mn-O-Mn bond angle due to increased orthorhombic distortion increases the next nearest neighbour (NNN) antiferromagnetic interaction,  $J_2$  and decreases the in-plane NN ferromagnetic interaction-  $J_1$ . The competing interaction between these two results in the magnetic frustration of the  $\text{Mn}^{3+}$  ions, resulting in a long wavelength incommensurate phase [25]. This is shown pictorially in the Fig.1.1. Thus, it is evident that the rare earth ionic radius affects both the structure as well as the magnetic property of the  $\text{RMnO}_3$  system.

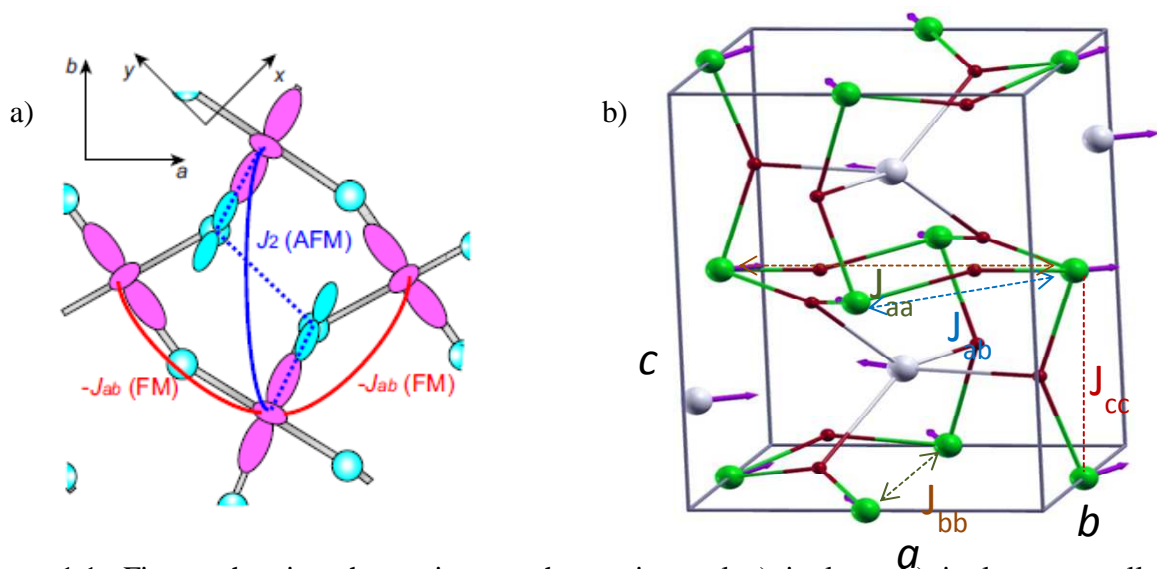


Figure.1.1: Figure showing the various exchange integral a) inplane, b) inplane as well as interplane for  $Pbnm$  structure  $J_{ab}$  is FM while  $J_{aa}$ ,  $J_{bb}$ , and  $J_{cc}$  are AFM

The experimentally obtained phase diagram of the  $\text{RMnO}_3$  systems, depicting the variation of Magnetic structure with Mn-O-Mn bond angle is shown in Fig.1.2 [25, 23]. The phase diagram shows that for intermediate  $R = \text{Gd-Ho}$ , with reduction in temperature the magnetic structure changes from paramagnetic to collinear incommensurate sinusoidal antiferromagnetic structure [26, 27, 28] of  $\text{Mn}^{3+}$ -sublattice with its magnetic moments alignment

pointing along the  $b$ -axis. The incommensurate modulation is characterized by a temperature dependent propagation wave vector  $k_{mag}^{Mn}(T)$ . The magnetic structure modulates the underlying lattice through a magneto-elastic coupling. This causes the modulation of propagation wave vector  $k_{lat}$  to be twice that of the magnetic modulation i.e.  $k_{lat}(T) = 2k_{mag}(T)$ .

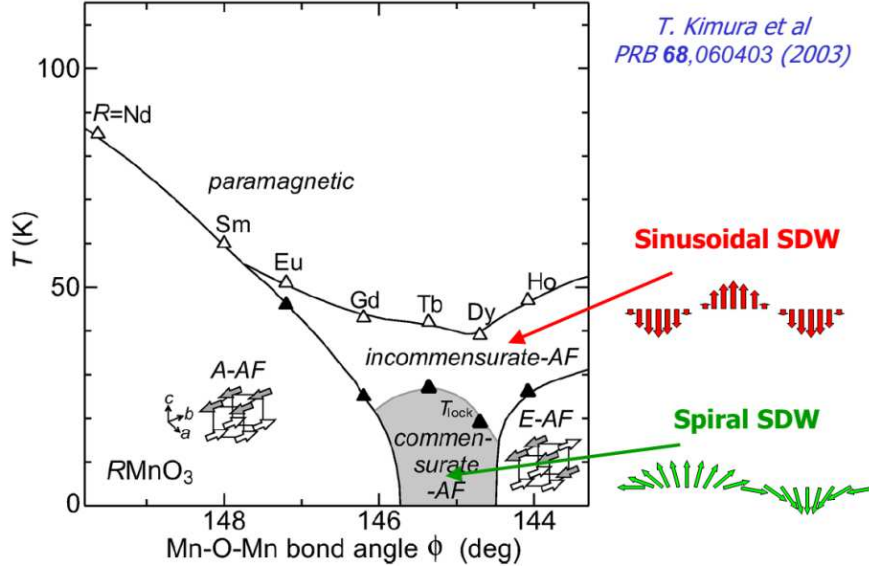


Figure.1.2: Phase diagram of  $\text{RMnO}_3$  as a function of Mn-O-Mn bond angle.

On further reduction of temperature,  $k_{mag}^{Mn}(T)$  starts to vary up to a temperature below which  $k_{mag}^{Mn}$  locks a constant value  $k_{lock}^{Mn}$ . At this temperature  $T_{lock}^{Mn}$ , the magnetic structure changes from collinear sinusoidal to a non-collinear (cycloidal) incommensurate structure (R= Tb and Dy) with the moment of the  $\text{Mn}^{3+}$  ion lying along the  $bc$ -plane. With the onset of the incommensurate cycloidal magnetic structure,  $\text{TbMnO}_3$  and  $\text{DyMnO}_3$  exhibit spontaneous polarization along the  $c$ -axis [29]. On the other hand, at  $T_{lock}^{Mn}$ , the  $k_{mag}^{Mn}$  of  $\text{GdMnO}_3$  drops from a finite value to zero ( $k_{lock} = 0$ ) to adopt an A-type (commensurate) antiferromagnetic structure. This process renders  $\text{GdMnO}_3$  paraelectric. Nonetheless, upon the application of a magnetic field as small as 1T along  $b$ -axis, polarization can be induced along the  $a$ -axis [30].The concomitant

emergence of polarization with cycloidal magnetic structure has been initially explained on the basis of a spin current model or inverse Dzyaloshinsky-Moriya (DM) effect proposed by Katsura-Nagaosa-Balatsky (KNB) [31]. This effect is purely an electronic process in which the spin-orbit interaction modifies the hybridization of electronic orbitals in such a way that a ferroelectric polarization of the charge density distribution emerges. It is important to note that this picture does not demand the displacement of ions from their centrosymmetric positions. The overlap of electronic wave functions of two adjacent atoms with canted spins can give rise to a local electric polarization given by

$$p_i = Ae_{i,i+1} \times (S_i \times S_{i+1})$$

Where  $e_{i,i+1}$  denotes the unit vector connecting two adjacent sites,  $S_i$  and  $S_{i+1}$  are the spins of the adjacent atoms and  $A$  is a constant determined by the spin-exchange and spin-orbit interactions. As the modulated magnetic structure forces the lattice to modulate [9, 29, 32, 33], an alternate theoretical model was proposed to explain the emergence of spontaneous polarization on the basis of magnetically induced displacement of relevant ions [34, 35]; the spiral spin order can induce uniform shifts of the oxygen ions through the spin-lattice coupling via the DM interactions, leading to the electric polarizations. Such a polarization is termed as an improper polarization. Theoretical studies have shown that the displacement of  $O^{2-}$  ions alone cannot account for the large polarization values observed in these materials and that the displacement of  $Mn^{3+}$  ions plays a more important role [36, 37]. These studies show that the lattice-mediated contributions to the ferroelectric polarization are dominant as compared to the purely electronic sources. Recent experimental evidence based on non-resonant magnetic x-ray scattering have shown that magnetically induced ionic displacements are responsible for substantial value of polarization in  $TbMnO_3$  [38, 39].

From the phase diagram shown in Fig.1.2, it is seen that for a narrow range of Mn-O-Mn bond angles, a cycloidal magnetic structure exists with an attendant spontaneous polarization. As the Mn-O-Mn bond angle of TbMnO<sub>3</sub>, DyMnO<sub>3</sub> falls in this window, they show a multiferroic property. Additionally, the phase diagrams hands out the scope for inducing a multiferroic property in other systems whose Mn-O-Mn angle falls outside this favourable range. In Perovskite compounds, the structure and hence the Mn-O-Mn can be modified in a straight forward fashion through an alteration of the average rare earth ionic radius.

### 1.2.1. TbMnO<sub>3</sub>

The multiferroic property of TbMnO<sub>3</sub> was reported by Kimura *et al.* in the seminal paper [9] and is one of the most extensively studied type-II multiferroic rare earth manganite. Magnetization and heat capacity data showed three distinct features at 41K, 27K and 7K. The transition at 41K is associated with the magnetic transition from paramagnetic to collinear sinusoidal antiferromagnetic of Mn<sup>3+</sup> sublattice [26, 27, 28, 40, 41]. The Mn<sup>3+</sup> spins are aligned along the *b*-axis with an incommensurate propagation wave vector  $k_{mag}^{Mn} = (0, 0.29, 1)$  in the *Pbnm* orthorhombic unit cell. With the decrease of temperature,  $k_{mag}^{Mn}$  decreases and gets locked in at  $k_{mag}^{Mn} = (0, 0.276, 1)$  below  $T_{lock}^{Mn}$  leading to magnetic transition, from sinusoidal to cycloidal [28] with the attendant emergence of spontaneous polarization along the *c*-axis. This is well captured in the variation of the imaginary part of the dielectric constant with temperature  $\epsilon''(T)$  [9]; while the dielectric constant along the *a*- and *c*-axis shows sharp anomalies, small and smooth variation is observed along the *b*-axis [29]. The transition at 7K is associated with the ordering of Tb<sup>3+</sup> magnetic moment in a canted antiferromagnetic structure with a propagation vector of  $k_{mag}^{Tb} = (0, 0.41, 1)$ . Corresponding to this temperature, a small anomaly is observed in

$\varepsilon''(T)$  along the  $a$ -axis as well. Application of magnetic field along the  $b$ -axis, results in reorientation of the ferroelectric order from  $c$ -axis to  $a$ -axis, known as electric polarization flop. Application of a magnetic field along the  $a$ -axis increases the strength of the anomaly at  $T_{lock}^{Mn}$ , with no shift in its position. Regardless of the direction of the applied magnetic field, no polarization develops along the  $b$ -axis. Application of magnetic field along  $c$ -axis dramatically varies the  $T_{lock}^{Mn}$  temperature [30] and suppresses the polarisation along the  $c$ -axis above 7T. The origin of polarization below  $T_{lock}^{Mn}$  has been attributed to the magnetoelastically induced ionic displacement [38, 39]. Holwker *et al.* have shown using non resonant magnetic x-ray scattering that ionic displacement make a substantial contribution to the observed value of polarization.

### 1.2.2. DyMnO<sub>3</sub>

The multiferroic property of DyMnO<sub>3</sub> was reported by Goto *et al.*, and its multiferroic properties are similar to that of TbMnO<sub>3</sub> [29]. DyMnO<sub>3</sub> shows an antiferromagnetic sinusoidal transition of the Mn<sup>3+</sup>- sublattice below 39K and the moments of Mn<sup>3+</sup> aligning along the  $b$ -axis with incommensurate propagation wave vector  $k_{mag}^{Mn} = (0, 0.72, 1)$ . As the temperature is decreased the  $k_{mag}^{Mn}$  increase and gets locked to  $(0, 0.77, 1)$  below the  $T_{lock}^{Mn} \sim 18$ K resulting in a cycloidal magnetic structure. Accordingly, spontaneous polarization along the  $c$ -axis is reported, which could be flipped to the  $a$ -axis by the application of a magnetic field. The Dy spins align commensurately  $k_{mag}^{Dy} = (0, 0.5, 1)$  below 6.5K in an antiferromagnetic structure. The magnitude of polarization in DyMnO<sub>3</sub> is larger than in TbMnO<sub>3</sub>. The temperature dependent dielectric constant shows a broad peak along the  $a$ -axis and a sharp peak along the  $c$ -axis at the  $T_{lock}^{Mn}$  temperature. The variation of the dielectric constant with the application of a magnetic field

along  $a$  and  $b$ -axis is similar to that of  $\text{TbMnO}_3$ . In contradiction to  $\text{TbMnO}_3$ , the polarization along  $c$ -axis is not suppressed by application of magnetic field along  $c$ -axis up to 9T.

### 1.2.3. $\text{Eu}_{1-x}\text{Y}_x\text{MnO}_3$

As discussed in the earlier section, the A-type AFM ground state of  $\text{RMnO}_3$  systems can be changed by tuning the average ionic radii of the R-site, such that the Mn-O-Mn bond angle falls in the window exhibiting a modulated magnetic and crystallographic structure. This would allow the realization of multiferroic properties in otherwise non-ferroelectric  $\text{RMnO}_3$  systems. An example of such a system is  $\text{EuMnO}_3$  [42, 43]. When partial substitution of Eu with Y was carried out to effect required structural and Mn-O-Mn modifications, the ground state of  $\text{Eu}_{1-x}\text{Y}_x\text{MnO}_3$  for  $x = 0.2-0.3$  changes from a canted A-type antiferromagnetic to presumably spiral /cycloidal structure in the  $ab$ -plane with the emergence of a spontaneous polarisation along the  $a$ -axis below 30K. For higher concentrations, the polarization direction changes from  $c$ -axis at higher temperatures to  $a$ -axis at lower temperatures. Change of the cycloidal from  $bc$ - to the  $ab$ -plane results in a reorientation of the polarization direction. The regime of  $c$ -axis polarization increases with increasing Y concentration. The reorientation of polarization or the flipping of the cycloidal magnetic structure of the  $\text{Mn}^{3+}$  ions can thus be achieved both by a thermal variation and by increasing orthorhombic distortion. The presence of magneto-elastic coupling has been established in this class of system by anomalies seen in temperature dependent lattice parameter variation across the magnetic transitions [44].

#### 1.2.4. $\text{Sm}_{1-x}\text{Y}_x\text{MnO}_3$

Multiferroic properties of yet another mixed crystal system  $\text{Sm}_{1-x}\text{Y}_x\text{MnO}_3$  was reported by O'Flynn [45]. They reported the presence of modulated magnetic transition for  $x = 0.4$  and  $0.5$  at  $T_{N2} \sim 23-25\text{K}$  apart from the paramagnetic to sinusoidal antiferromagnetic transition at  $T_{N1} \sim 41\text{K}$ . Associated with modulated magnetic transition is the emergence of spontaneous polarization along the  $c$ -axis. This is also inferred by the sharp peak like transition along the  $c$ -axis in the temperature dependent variation of the dielectric constant at  $T_{N2}$ . The behaviour of this transition with the applied magnetic field is similar to that of found in  $\text{TbMnO}_3$ .

### 1.3. Motivation for the present study

It is reasoned from experimental and theoretical studies that multiferroic properties can be induced in non-ferroelectric A-type antiferromagnetic  $\text{RMnO}_3$  systems by suitably modifying the average ionic radii of R. From the phase diagram Fig.1.2 it is seen that  $\text{GdMnO}_3$  exists close to the phase boundary between A-type antiferromagnetic and the modulated long wavelength structure. One would therefore expect the exchange interactions to subtly compete with each other. Thus,  $\text{GdMnO}_3$  is a good candidate for investigating the emergence of multiferroic properties.  $\text{GdMnO}_3$  has an A-type AFM ground state and is paraelectric in the entire temperature range. It exhibits a modulated magnetic structure in the form of sinusoidal AFM ordering of the  $\text{Mn}^{3+}$  sublattice below  $43\text{K}$  [30] with an incommensurate propagation wave vector  $k_{mag}^{Mn} = (0, 0.48, 1)$ . As the temperature is reduced the degree of incommensuration decreases and abruptly jumps from  $0.39$  to  $0$  at  $T_{\text{lock}} \sim 23\text{K}$ . With disappearance of the long wavelength modulated structure, the A-type AFM structure emerges [30, 46]. Thus, it can be inferred from this observation that it should be easy to modify the magnetic ground state of  $\text{GdMnO}_3$  by appropriately modifying the rare earth ionic radius. The  $\text{Gd}^{3+}$  sublattice enters into a

canted antiferromagnetic structure below 5.1K. The temperature dependent dielectric constant shows some interesting anomalies. As the temperature is decreased the dielectric constant along the  $a$ - and  $c$ -axis keep increasing with a sudden drop at  $T_{lock}^{Mn}$  to result in a step like behaviour rather than a peak. As the temperature is further reduced, additional anomaly corresponding to AFM ordering temperature ( $T_N^{Gd}$ ) of  $Gd^{3+}$  - sublattice is observed. In general, external magnetic field shifts these dielectric anomalies to higher temperature and suppresses the anomaly around  $T_N^{Gd}$  [30]. Goto *et al.*, studied the multiferroic properties of  $Tb_{1-x}Gd_xMnO_3$  for  $0 \leq x \leq 1$  [47]. For  $x < 0.6$ , the polarization along the  $c$ -axis with a sharp peak in the temperature dependent dielectric constant is reported. With increase in the concentration of Gd  $0.6 < x < 0.8$  the polarization changes direction from  $c$ -axis to  $a$ -axis indicated by a sharp peak in the  $\epsilon(T)$  along  $a$ -axis. In addition, a step like anomaly at lower temperature is also seen, indicating reentrant into a paraelectric phase. Investigators also report that the rare earth  $f$ -electron moments of Tb and Gd affect the multiferroic properties of the mixed-crystal system. Hence an investigation into the correspondence between multiferroic properties of the  $GdMnO_3$  system and a variation of the average Gd ionic radius involving non  $f$ -electron system would be interesting. In this regard we have chosen  $Gd_{1-x}Y_xMnO_3$  ( $x = 0.2, 0.3$  &  $0.4$ ) mixed crystal system to study the structural, dielectric and magnetic properties. Only one report exists on study of similar system by Ivanov *et al.* [48] which is limited to  $x = 0.2$  concentration. The system was shown to have a polarization and only dielectric properties were discussed.

The present thesis deals with the structural, dielectric and magnetic study of the  $Gd_{1-x}Y_xMnO_3$  ( $x=0.2, 0.3$  &  $0.4$ ) system. The presentation of the material is structured as follows: The procedure for the synthesis of the material, room temperature structural analysis as function of composition and magnetization studies are discussed in chapter 3. This is followed

by the low temperature dielectric study to find the ferroelectric ordering and low temperature lattice parameter study to elucidate magneto-elastic coupling in chapter 4. The chapter also discusses the magneto caloric effect in this system. Chapter 5 deals with low temperature Raman studies and computational studies to find the existence of different phonon modes and band structure calculations for different composition. The thesis ends with conclusions and future scope.

## References :

- [1]. I. E. Dzyaloshinskii, *Zh. Eksp. Teor.Fiz.*, **33**, 881 (1959) *Sov.Phys. JETP* **10**, 628 (1960).
- [2]. H. Schmid, *Ferroelectrics* **162**, 317 (1994).
- [3]. V. J. Folen, G. T. Rado, and E. W. Stalder, *Phys. Rev. Lett* **6**, 607 (1961).
- [4]. G. T. Rado. and V. J. Folen., *Phys. Rev. Lett* **7**, 310 (1961).
- [5]. W. F. Brown, R. M. Hornreich, and S. Shtrikman, *Phys. Rev.* **168**, 574 (1968).
- [6]. E. Ascher, H. Rieder, H. Schmid, H. Stössel, . *J. Appl. Phys.* **1966**, 37, 1404
- [7]. N. A. Hill, *J. Phys. Chem. B* **104**, 6694 (2000)
- [8]. J. Wang, J.B. Neaton, H. Zheng, V. Nagarajan, S. B. Ogale, B. Liu, D. Viehland, V. Vaithyanathan, D. G. Schlom, U. V. Waghmare, N. A. Spaldin, K. M. Rabe, M. Wuttig, and R. Ramesh, *Science* **299**, 1719 (2003).
- [9]. T. Kimura, T. Goto, H. Shintani, K. Ishizaka, T. Arima and Y. Tokura, *Nature* **426**, 55 (2003)
- [10]. N. Hur, S. Park, P. A. Sharma, J. S. Ahn, S. Guha, and S.-W. Cheong, *Nature* **429**, 392 (2004).
- [11]. D. Khomskii, *Physics* **2**, 20 (2009).
- [12]. J. Moreau, C. Michel, R. Gerson, and W. James, *Journal of Physics and Chemistry of Solids* **32**, 1315 (1971).
- [13]. H. Kawano, R. Kajimoto, M. Kubota, and Y. Yoshizawa, *Phys.Rev. B* **53**, R14 709 (1996).
- [14]. E. O. Wollan and W. C. Koehler, *Phys. Rev.* **100**, 545 (1955).
- [15]. H. Y. Hwang, S. W. Cheong, P. G. Radaelli, M. Marezio, and B. Batlogg, *Phys. Rev. Lett.* **75**, 914 (1995).

- [16]. R. Mahendrian, S. K. Tiwary, A. K. Raychaudhuri, T. V. Ramakrishnan, R. Mahesh, N. Rangavittal, and C. N. R. Rao, *Phys.Rev. B* **53**, 3348 (1996).
- [17]. R. M. Kusters, J. Singleton, D. A. Keen, R. McGreevy, and W. Hayes, *Physica B* **155** 362 (1989).
- [18]. G. H. Jonker and H. van Santen, *Physica* **16** , 337 (1950) ;G.H. Jonker, *ibid* . **22** , 707 (1956).
- [19]. R. D. Shannon and C. T. Prewitt, *Acta Crystallogr. B* **25**, 725 (1969); **26**, 1046 (1970).
- [20]. Y. Murakami J. P. Hill, D. Gibbs, M. Blume, I. Koyama, M. Tanaka, H. Kawata, T. Arima, Y. Tokura, K. Hirota, and Y. Endoh, *Phys. Rev. Lett.* **81**, 582 (1998).
- [21]. F. Moussa M. Hennion, J. Rodriguez-Carvajal, H. Moudden, L. Pinsard, and A. Revcolevschi, *Phys. Rev. B* **54**, 15 149 (1996).
- [22]. J. B. Goodenough, *Phys. Rev.* **100**, 564 (1955).
- [23]. J.-S. Zhou and J. B. Goodenough, *Phys. Rev. Lett.* **96**, 247202 (2006)
- [24]. S. Ishihara, J. Inoue, and S. Maekawa., *Phys. Rev. B* **55**, 8280 (1997).
- [25]. T. Kimura, S. Ishihara, H. Shintani, T. Arima, K. T. Takahashi, K. Ishizaka, and Y. Tokura, *Phys. Rev. B* **68**, 060403R (2003).
- [26]. S. Quezel, F. T. Cheou, J. Rossat-Mignod, G. Quezel, and E. Roudaut, *Physica B & C* **86-88**, 916 (1977).
- [27]. R. Kajimoto, H. Yoshizawa, H. Shintani, T. Kimura, and Y. Tokura, *Phys. Rev. B* **70**, 012401 (2004); **70**, 219904(E) (2004).
- [28]. M. Kenzelmann, A. B. Harris, S. Jonas, C. Broholm, J. Schefer, S. B. Kim, C. L. Zhang, S.-W. Cheong, O. P. Vajk, and J. W. Lynn, *Phys. Rev. Lett.* **95**, 087206 (2005).
- [29]. T. Goto, T. Kimura, G. Lawes, A. P. Ramirez, and Y. Tokura, *Phys. Rev. Lett.* **92**, 257201 (2004)
- [30]. T. Kimura, G. Lawes, T. Goto, Y. Tokura, and A. P. Ramirez, *Phys. Rev. B* **71**, 224425 (2005).

- [31]. H. Katsura, N. Nagaosa, and A. V. Balatsky, *Phys. Rev. Lett.* **95**, 057205 (2005).
- [32]. T. Arima, T. Goto, Y. Yamasaki, S. Miyasaka, K. Ishii, M. Tsubota, T. Inami, Y. Murakami, and Y. Tokura, *Phys. Rev. B* **72**, 100102R (2005).
- [33]. D. Higashiyama, S. Miyasaka, N. Kida, T. Arima, and Y. Tokura, *Phys. Rev. B* **70**, 174405 (2004).
- [34]. I. A. Sergienko and E. Dagotto, *Phys. Rev. B* **73**, 094434 (2006).
- [35]. A. B. Harris, *J. Appl. Phys.* **99**, 08E303 (2006).
- [36]. H. J. Xiang, S.-H. Wei, M.-H. Whangbo, and J. L. F. Da Silva, *Phys. Rev. Lett.* **101**, 037209 (2008).
- [37]. A. Malashevich and D. Vanderbilt, *Phys. Rev. Lett.* **101**, 037210 (2008).
- [38]. H. Walker, F. Fabrizi, L. Paolasini, F. de Bergevin, J. Herrero- Martin, A. T. Boothroyd, D. Prabhakaran, and D. McMorrow, *Science* **333**, 1273 (2011).
- [39]. H. C. Walker, F. Fabrizi, L. Paolasini, F. de Bergevin, D. Prabhakaran, A. T. Boothroyd, and D. F. McMorrow, *Phys. Rev. B* **88**, 214415 (2005).
- [40]. Y. Yamasaki, H. Sagayama, T. Goto, M. Matsuura, K. Hirota, T. Arima, and Y. Tokura, *Phys. Rev. Lett.* **98**, 147204 (2007); **100**, 219902(E) (2008).
- [41]. N. Aliouane, K. Schmalzl, D. Senff, A. Maljuk, K. Prokeš, M. Braden, and D. N. Argyriou, *Phys. Rev. Lett.* **102**, 207205 (2009).
- [42]. J. Hemberger, F. Schrettle, A. Pimenov, P. Lunkenheimer, V. Y. Ivanov, A. A. Mukhin, A. M. Balbashov, and A. Loidl, *Phys. Rev. B* **75**, 035118 (2007).
- [43]. Y. Yamasaki, S. Miyasaka, T. Goto, H. Sagayama, T. Arima, and Y. Tokura, *Phys. Rev. B* **76**, 184418 (2007).
- [44]. J. Agostinho Moreira, A. Almeida, W. S. Ferreira, J. P. Araújo, A. M. Pereira, M. R. Chaves, M. M. R. Costa, V. A. Khomchenko, J. Kreisel, D. Chernyshov, S. M. F. Vilela, and P. B. Tavares, *Phys. Rev. B* **82**, 094418 (2010).

- [45]. O’Fynn, C. V. Tomy, M. R. Lees, A. Daoud-Aladine, and G. Balakrishnan, *Phys. Rev. B* **83**, 174426 (2011).
- [46]. J. Hemberger, S. Lobina, H.-A. Krug von Nidda, N. Tristan, V. Y. Ivanov, A. A. Mukhin, A. M. Balbashov, and A. Loidl, *Phys. Rev. B* **70**, 024414 (2004).
- [47]. T. Goto, Y. Yamasaki, H. Watanabe, T. Kimura, and Y. Tokura, *Phys. Rev. B* **72**, 220403R (2005).
- [48]. V. Yu. Ivanov, A. A. Mukhin, V. D. Travkin, A. S. Prokhorov, Yu. F. Popov, A. M. Kadomtseva, G. P. Vorob’ev, K. I. Kamilov, and A. M. Balbashov, *phys. stat. sol. (b)* **243**, No. 1, 107–111 (2006)

## CHAPTER 2

### Experimental techniques data analysis and calculations

#### 2.1 Sample preparation

Bulk polycrystalline samples of  $Gd_{1-x}Y_xMnO_3$  ( $x = 0, 0.2, 0.3$  &  $0.4$ ) were prepared by conventional solid state reaction route.  $Gd_2O_3$ ,  $Y_2O_3$  and  $MnO_2$  (*Alfa Aesar*) with purity better than 99.995% were used as starting materials. Stoichiometric amounts of precursor  $Gd_2O_3$ ,  $Y_2O_3$  and  $MnO_2$  were weighed and thoroughly mixed using an agate mortar and pestle. High purity acetone was used as a wetting medium to assist the mixing process. Care was taken to remove the moisture in  $Gd_2O_3$  and  $Y_2O_3$  before weighing by preheating up to  $900\text{ }^\circ\text{C}$  for 8 hours. The well-mixed, dry powder samples were calcined at  $450^\circ\text{C}$ ,  $850^\circ\text{C}$  and  $1350^\circ\text{C}$  for 80 hours with intermittent grinding. The resultant powder was compacted into pellets of 10 mm diameter and sintered at  $1350^\circ\text{C}$ . Heating rate of  $120^\circ\text{C/hr}$  was used in all the heat treatments and after the dwell time, the samples were furnace cooled to room temperature. The stability of the furnace was better than  $\pm 5\text{ }^\circ\text{C}$  in the whole temperature range. All the synthesis work was carried out at ambient pressure and atmosphere.

#### 2.2. Room temperature powder X-ray diffraction (XRD)

Room temperature powder XRD patterns of the samples were collected using a fully computer controlled diffractometer (*STOE, Germany*) operated in the Bragg-Brentano para-focussing geometry. The diffractometer consists of a 4 kW X-ray generator (*Spellman DF-4*) with sealed-tube Cu-target, highly oriented (002) flat pyrolytic graphite secondary

monochromator with minimum mosaic spread and a detection unit consisting of a NaI(Tl) scintillation counter. A Si (911) single crystal wafer with a shallow cavity that yields a low background was used as the sample holder. Other details of the experimental set up are given in Table 2.1.

<b>Geometry</b>	Bragg-Brentano Para-focussing geometry, Vertical, R = 260 mm
<b>Target power setting</b>	30 kV × 40 mA (maximum: 50 kV × 80 mA)
<b>Radiation</b>	Cu K <sub>α</sub> (λ = 1.5418 Å)
<b>Soller slits</b>	Incident and reflected beam sides (1°)
<b>Slits</b>	Divergence slits (DS): 0.1-0.5 mm, variable motorized Receiving slits (RS) : 0.1-0.5 mm, variable motorized During a given XRD run, both DS and RS were kept fixed at 0.3 mm.
<b>Scan mode</b>	θ – 2θ
<b>Scan range</b>	2θ = 20 – 90°
<b>Step size</b>	0.05°
<b>Dwell time</b>	Varied to get a minimum count of ~ 6 × 10 <sup>3</sup> for the 100% peak
<b>2θ standard</b>	Silicon (NIST SRM 640b)
<b>2θ correction</b>	Linear interpolation of the nearest 2θ of the standard
<b>Intensity standard</b>	α-Al <sub>2</sub> O <sub>3</sub> (NIST SRM 674)

**Table 2.1:** Details of the STOE Diffractometer.

Approximately 20 mg of fine powder of the sample, slightly exceeding the volume of the cavity on the sample holder, was uniformly spread over the cavity. A microscope glass slide was used to very lightly compress the powder into the cavity. The excess sample material was removed by an inclined glass slide over the groove. The dwell time was chosen, in such a way that the Bragg intensity of the 100 % peak is more than 6×10<sup>3</sup> counts. It should be emphasized

here that the  $2\theta$  (zero) correction was performed using NIST SRM Si powder before recording each set of XRD patterns. Analysis of the powder pattern to extract the crystallographic information was carried out by Rietveld refinement [1] using General Structure Analysis System (GSAS) [2] software. A brief description of the above software packages and the methodology used in them is given at the end of this chapter.

### **2.3. Scanning electron microscopy and energy-dispersive X-ray analysis**

Scanning electron microscopy (SEM) (*Hitachi SU6600, Japan*) a Schottky Field Emission Analytical SEM coupled with an energy-dispersive X-ray spectrometer (*EDX*) was employed for the microstructural analysis and the elemental mapping of  $\text{Gd}_{1-x}\text{Y}_x\text{MnO}_3$  ( $x = 0, 0.2, 0.3$  &  $0.4$ ) compounds. The variable pressure mode allows for observation and analysis of non-conductive samples without the need for elaborate sample preparation. The SU6600 SEM system employs a tungsten filament serving as the electron source with an applied acceleration voltage in the range of 0.5 to 30 kV. It has a highly efficient Everhart-Thornly Secondary Electron Detector (SED) for high resolution imaging and a low impedance solid state Backscattered Electron Detector (BSED). Micro-Structural analysis was carried out using the secondary electron mode whereas the back-scattered electron mode was used for mapping the elemental distribution of the compound using a multi-channel analyzer.

The samples were mounted on a 5-axis, computer euentric, motor-drive stage using double sided adhesive carbon tape. The observation sites were chosen on the grain, across grain as well as near the grain boundaries. The reproducibility was checked by acquiring the data at different locations of at least two pellets of the same composition.

## 2.4. Magnetisation measurement

The dc magnetization measurements were carried out using a 12 Tesla commercial (Oxford Instruments) vibrating sample magnetometer (VSM) as a function of magnetic field and temperature. For zero-field-cooled magnetization ( $M_{ZFC}$ ) measurements, the sample was first cooled from room temperature down to 5K in zero field. After applying the magnetic field of 200 Oe at 5K, the magnetization was measured in the warming cycle with field on. Whereas, for field-cooled magnetization ( $M_{FC}$ ) measurements, the sample was cooled in the same field (measuring field in the ZFC case) down to 5K and  $M_{FC}$  was measured in the warming cycle under the same field.

## 2.5. Specific heat

The specific heat measurements were made using a 14T/2K physical property measurement system (PPMS) of Quantum design (QD), USA by thermal relaxation method [3]. The system is capable of measuring heat capacity both as function of temperature and applied magnetic field. Thermal-relaxation calorimetry provides a means of determining a sample's specific heat by measuring the thermal response of a sample/calorimeter assembly to a change in heating conditions. Sample typically weighting 20 mg is used for the measurement in the form of discs. The sample is placed on a  $\sim 3 \times 3$  mm<sup>2</sup> platform in the middle of a "puck". The platform is suspended by wires, which isolate the platform from thermal contact with the system, and are also used for platform heating and temperature measurement. The sample is attached to the platform using Apiezon N-grease. This puck is then placed inside a superconducting magnet which has a temperature range of 2-400 K, and is capable of applying magnetic fields up to  $\pm 14$ T. The heat capacity is then determined at a particular temperature by applying a small

increase in temperature (typically ~ 5% of the current temperature) and measuring how long the sample takes to return to the initial temperature. This is given by

$$T_p(t) = T_o + \Delta T \exp(-t/\tau)$$

Where  $T_p$  is the sample/platform temperature,  $T_o$  external /bath temperature ,  $\Delta T$  is increase in temperature and  $\tau$  is the relaxation time. By measuring the relaxation time the heat capacity can be determined by

$$\tau = (C_s + C_a)/K$$

Where  $C_s$  is the heat capacity of the sample  $C_a$  is the heat capacity of the addenda and  $K$  is the thermal conduction of the sample/platform with the bath. As both the sample platform and the Apiezon grease contribute to the relaxation time, it is necessary to initially take an addenda measurement, where the heat capacity of just the puck and the grease is measured over the temperature range required for the sample measurement. This is then subtracted from the subsequent measurement with the sample present.  $K$  is determined by measuring the temperature change  $\Delta T$  when power is applied. Heat capacity so measured is under the assumption that in small temperature change  $\Delta T$ , the heat capacity remains unchanged.

## 2.6. Dielectric spectroscopy

The dielectric properties were measured using an Alfa analyser (Novocontrol Systems, Germany) impedance analyser connected to a Helium cryostat sample insert on sample of 10mm dia and 2mm thickness. Silver paste was applied on both sides of the pellets for better electrical contacts. Experimentally, the dielectric constant of a material can be determined by measuring its capacitance, assuming its dimensions are well known. Both the real  $\epsilon'$  and imaginary  $\epsilon''$  part of dielectric permittivity was measured in the temperature interval of 5 to 70K in the frequency

range of  $10^0$  to  $10^6$  Hz. The temperature was varied using a helium bath cryostat with a dip stick arrangement for lowering the sample. The temperature stability was better than  $\pm 1$  K. Both  $\epsilon'$  and  $\epsilon''$  were plotted as a function of temperature at different frequencies and as function of frequency at different temperature for analysis.

## 2.7. Low temperature XRD

Low temperature x-ray diffraction measurements on powder samples of  $Gd_{1-x}Y_xMnO_3$  ( $x = 0, 0.2, 0.3$  &  $0.4$ ) in the temperature range of 70 to 10K were carried out using angle dispersive x-ray diffraction (ADXRD) beam line (BL-12) at INDUS-2 synchrotron source. Indus-2 is a 2.5 GeV, 100 mA second generation synchrotron facility. The ADXRD beamline is setup and installed on BL-12 bending magnet port of the Indus-2 synchrotron. The electron source size at

<b>Spectral range</b>	5-20keV
<b>Energy resolution</b>	1eV at 10keV [measured value $\sim 7000$ ( $\Delta E/E$ ) at Cu K-edge]
<b>Flux</b>	$10^{10}$ photons/sec at 10keV
<b>Beam size</b>	0.7mm (H) x 0.5mm (V)
<b>Angular resolution</b>	15 arc sec (single crystal in rocking curve open detector geometry)  0.03 degree ( $2\sigma$ in $2\theta$ ) for powder LaB <sub>6</sub> (NIST) on diffractometer  0.06 degree ( $2\sigma$ in $2\theta$ ) powder sample on Image Plate)

Table.2.2: Table showing the various beam parameters of BL-12 ADXRD beamline.

the port is approximately 0.5 mm (H) X 0.5 mm (V) and the beam acceptance of the beamline is 2 mrad(H) x 0.15 mrad(V). The optical elements consists of a platinum coated pre-mirror (M1) which is plane and bendable and is used for vertical focusing/collimation of the x-ray beam. This

is followed by a double crystal monochromator (DCM) with Si(111) which is used for monochromatization of photon beam. A second crystal of the DCM is also used for the sagittal focusing of the beam. For high energy resolution Si(311) crystal pair is used. The third optical element is a platinum coated bendable post mirror (M2) used for vertical focusing/collimation of the beam. The photon beam parameter of the beamline are given in Table.2.2

The diffraction patterns were recorded with a wavelength,  $\lambda = 1.0293 \text{ \AA}$  (12keV) in Debye-Scherrer geometry using an image plate area detector (MAR 345 DTB). The wave-length was accurately calibrated using diffraction pattern of LaB6 NIST standard. The area detector is a 345 mm diameter image plate capable of recording XRD pattern with a Q-range of up to  $10.88 \text{ \AA}^{-1}$  at 20keV with an angular resolution of 0.06 degree ( $2\sigma$  in  $2\theta$ ). The powder sample was sandwiched between Kapton sheets. For low temperature a liquid helium based flow type cryostat was used with Lakeshore 331 temperature controller. Temperature stability during each measurement was estimated to be  $\pm 2\text{K}$ . The sample chamber consists of evacuated double concentric Be dome for minimizing conduction and radiation loss. The sample sandwiched between kapton sheets is placed on a Be disc inside the sample chamber for thermalisation of temperature. As result of this setup Be diffraction peaks are also observed along with the sample peaks. Due to the difference in distance of the two concentric Be dome from the image plates, the Be peaks appear at different position at the image plate intermixed with sample peaks. This makes it difficult for removal of Be diffraction peaks for XRD analysis. Hence only the lattice parameter variation as a function of temperature was estimated and the atomic position variation could not be determined by Rietveld refinement.

## 2.8. Raman spectroscopy

Study of optical mode lattice vibration throw more light into the understanding of various physical properties an example of which is Jahn-Teller induced lattice distortion which changes the electron kinetic energy near magnetic transition in Perovskite manganites. The optical phonon were studied by recording the Raman spectrum on pelletised  $Gd_{1-x}Y_xMnO_3$  ( $x = 0, 0.2, 0.3$  &  $0.4$ ) sample using Renishaw (model: inVia Raman microscope) system using 514.5 nm excitation source with an optical eye piece of 20x magnification. The Raman spectra were measured in the temperature range of 300K to 4K in steps of 10K down till 50K and in steps of 3K till 4K using a Helium gas flow closed cycle refrigerator. The Raman spectra were recorded in  $200\text{ cm}^{-1}$  to  $800\text{ cm}^{-1}$  wave number range. The peaks were fitted with voigt function to find the peak position and FWHM for analysis.

## 2.9. Band structure calculations methodology

First principles DFT calculations of the electronic band structure were carried out using the non-scalar relativistic full potential linearized augmented plane wave (FP-LAPW) method for  $Gd_{1-x}Y_xMnO_3$  ( $x = 0, 0.25, 0.5$ , and  $1$ ) to study the structural and electronic properties with the Generalized Gradient Approximation (GGA) using the PBESol [4] for the exchange and correlation functional. The Kohn-Sham equations were solved with the full potential linearized augmented plane wave technique, as implemented in the WIEN2K package [5]. In the present self-consistent calculation, a muffin-tin model for the crystal potential was assumed. The electrons are divided into two groups: the core electrons whose charge densities are confined within the muffin-tin spheres and the valence electrons outside the spheres. In the two regions of the unit cell, different basis sets are used to expand the wave function, charge density and the

potential function. Inside the non-overlapping spheres of muffin-tin radius ( $R_{MT}$ ) around each atom, a linear combination of the product of the radial solutions of the Schrödinger equation and the spherical harmonics is used, while the plane wave basis set is used in the interstitial region. Non-overlapping sphere radius  $R_{MT}$  is chosen in such a way that there is no charge leakage from the core and total energy convergence is ensured. We used the Muffin-Tin radius ( $R_{MT}$ ) of 2.14 a.u. for Y, 2.24 a.u. for Gd, 1.85 a.u. for Mn and 1.59 a.u. for O atoms. The basis set and k-points were found to be fully converged with  $R_{MT} * K_{max} = 7.5$ ,  $G_{max} = 12$  and 300 k-points in the full Brillouin zone. Same numbers were used for all the calculations. Before calculating the material properties, the convergence tests with respect to the basis set size and the k-points used in the calculations were performed. Both the  $GdMnO_3$  and  $YMnO_3$  were specified in the  $Pnma$  (62) space group as the two end compounds. We have used the experimental lattice parameters for  $GdMnO_3$ ,  $Gd_{0.75}Y_{0.25}MnO_3$  and  $Gd_{0.5}Y_{0.5}MnO_3$  obtained from the x-ray diffraction experiments on the samples, while the parameters for  $YMnO_3$  were taken from literature [6] for our calculations. The atom positions were relaxed using the symmetry of the  $Pnma$  space group for the  $GdMnO_3$  and  $YMnO_3$  systems. For the intermediate systems,  $Gd_{0.75}Y_{0.25}MnO_3$  and  $Gd_{0.5}Y_{0.5}MnO_3$ , Gd atoms in the unit cell were replaced to obtain the required Gd:Y ratio, by first converting the system to  $P1$  space group with no symmetry other than translational symmetry, and then replacing one or two of the Gd atoms by Y. The program was then allowed to find out the symmetry of the resulting crystal structure. It reported  $Pm$  (no. 6), unique axis  $c$ , as the space group for  $x = 0.25$  and  $P2_1/m$  (no. 11), unique axis  $c$ , as the space group for  $x = 0.5$  compound. All the atom positions were then relaxed using the symmetry of the reported space groups. The final forces in between the atoms in these ionic relaxation steps were lower than 5 mRyd/a.u. The electronic self consistent cycles were stopped when the energy convergence was better than  $10^{-7}$

Ryd, charge separation smaller than  $10^{-7}$  a.u. and force convergence 1 mRyd/a.u. The systems under study consist of the  $5f$  (Gd) and  $4d$  (Y) and  $3d$  orbitals (Mn), we have used the Hubbard interaction with a U-J value of 8 eV, along with the spin-orbit coupling effects to model the correlations present in the systems. Spin-orbit interaction uses a second variational method with the scalar-relativistic orbitals as basis. The number of eigenvalues doubles since SO couples the spin-up and spin-down states, so they are no longer separable and become a single state. Hence, the up- and down-spin density of states have been calculated without accounting for the spin-orbit coupling, while the band structures have been calculated for both the cases.

The lattice dynamics has been performed for a series of compounds  $\text{Gd}_{1-x}\text{Y}_x\text{MnO}_3$  ( $x = 0, 0.1, 0.2, 0.25, 0.3, 0.4, 0.5$  and 1) using the GULP module available in the Materials Studio package. The charge state of the ions in these systems is  $\text{Gd}^{3+}$ ,  $\text{Y}^{3+}$ ,  $\text{Mn}^{3+}$  and  $\text{O}^{2-}$ . The interactions have been modeled using Buckingham type interatomic pair potentials along with the Coulomb interaction between the different ions [7]. The potential form is given by  $V_{ij}(r_{ij}) = \frac{q_i q_j}{r_{ij}} + A_{ij} e^{-r_{ij}/\rho_{ij}} - \frac{C_{ij}}{r_{ij}^6}$ . O ion interactions are split into a core with -2.869 charge and a shell with 0.869 charge. A spring with a specified spring constant is used to model the core-shell interactions. The details of the potentials used for the different species are given in the table 2.3. We obtain the vibrational frequencies and phonon density of states of all the compounds.

Atom Types		Potential	$A_{ij}$	$\rho_{ij}$	$C_{ij}$	Charge	Cutoffs	
$i$	$j$	Type	(eV)	(Å)	(eV-Å <sup>6</sup> )		min (Å)	max (Å)
Mn core	O shell	Buckingham	1257.9	0.3214	0	+3	0	10
Gd core	O shell	Buckingham	1336.8	0.3551	0	+3	0	10
Y core	O shell	Buckingham	1345.1	0.3491	0	+3	0	10
O shell	O shell	Buckingham	22764.0	0.1490	27.879	+0.869	0	12
O core	O shell	Spring (c-s)	74.92	0	0	-2.869	0	0.6

Table 2.3: Interatomic potentials used for GULP calculation

Group theoretical analysis was carried out using the online available tool for the structures [8].

## 2.10. Rietveld refinement by GSAS

Rietveld refinement is a nonlinear least-squares refinement method, in which the best fit is obtained for the entire observed powder diffraction pattern taken as a whole and the entire calculated pattern based on the simultaneously refined models for the crystal structure(s), diffraction optics effects, instrumental factors and other specimen characteristics. The least square structural refinement of  $\text{Gd}_{1-x}\text{Y}_x\text{MnO}_3$  was carried out using GSAS program [2] which employs Rietveld analysis [1]. A brief description of the choice of the important parameters and the strategy adopted for the refinement procedure are given in the following.

Starting values of the structural parameters for the refinement are taken from the standard neutron powder diffraction of  $\text{RMnO}_3$  system [9]. A statistical replacement of Gd by Y was carried out over the  $4a$  site. For all compounds, the site occupancy was constrained in a manner consistent with the nominal stoichiometry of the compound. The atomic co-ordinates and isotropic thermal parameters are constrained to be equal for the different atomic species having same point symmetry. The background is defined by a shifted Chebyshev polynomial with a leading constant term (function 1 in GSAS), which is a default background function in the program. The background intensity was estimated during the initial iterations with six terms refined simultaneously. The intensity ratio of  $K_{\alpha 1}$  to  $K_{\alpha 2}$  in the energy spectrum of X-rays from X-ray tube, was estimated to be 0.445, from the integrated intensity analysis of the standard sample (NIST Si 640b) and is kept fixed during the refinement process. In GSAS, pseudo-voigt

function is integrated using multi-term Simpson's rule. The mixing parameter ( $\eta$ ) is assumed to have the functional form given by P. Thomson *et. al* [10]. A detailed description of the peak-profile parameters and their interpretation are given by Larson and Von Dreele [2], the parameters refined in the present work are summarized here. While absorption correction is not needed in Bragg-Brentano type powder diffraction geometry with flat plate samples, the zero shift of the instrument is chosen as one of the parameters for the refinement. The  $2\theta$  shift,  $\Delta T$ , is corrected for the peak asymmetry  $A_S$  and the sample shift  $S_S$  form the transverse diffractometer axis as  $\Delta T' = \Delta T + (f_i A_S / \tan 2\theta) + S_S \cos f_i$  is the Simpson's rule co-efficient for asymmetry and  $i$  denotes the number of terms in the summation. The modified Thompson-Cox-Hastings pseudo-voigt function [11] (peak shape function No. 2 of GSAS) is employed for the profile analysis. This function provides a better fit to the asymmetric profiles and shows less correlation with the unit cell dimensions. The width of the peak varies with  $2\theta$  as  $\sigma^2 = U \tan^2 \theta + V \tan \theta + W + P/\cos^2 \theta$ , where U, V and W co-efficients are described by Cagliotti *et. al.* [12] and P is the Scherrer co-efficient for Gaussian broadening. The Lorentzian co-efficient,  $\gamma$ , varies as  $\gamma = (X/\cos \theta) + Y \tan \theta$ , where the first term represents the Lorentzian Scherrer broadening, and the second term describes the strain broadening. The peak profiles were truncated at 0.1 % of the peak height. During the refinement, it was found that the preferred orientation effects are practically absent. The function  $\sum w_i (Y_{io} - Y_{ic})^2$ , representing the weighted sum of the squared errors, is minimized by least square procedure, where  $Y_{io}$  and  $Y_{ic}$  are the observed and calculated intensity at each step  $i$  in the pattern. The weight  $w_i$  assigned to each step intensity is the reciprocal of the variance  $\sigma_i^2$  at the  $i^{\text{th}}$  step and was evaluated by  $w_i = 1/\sigma_i^2 \approx N/ Y_{io}$  where N is the number of observations contributing to the average step intensity. The following goodness of fit R factors were evaluated.

$$R_p = \sigma |Y_{io} - Y_{ic}| / \sum Y_{io} \quad 2.1$$

$$R_{wp} = [\sum w_i (Y_{io} - Y_{ic})^2 / \sum w_i Y_{io}^2]^{1/2} \quad 2.2$$

$$S = \sum w_i (Y_{io} - Y_{ic})^2 / (N - P) \quad 2.3$$

where N and P are the number of observations and the adjustable parameters respectively. The least square refinement is continued until the sum of squared errors, i. e, parameter shifts/estimated standard deviation, is less than 1 %.

During refinement, the parameter turn-on procedure suggested by Young was largely adopted to select the parameters to refine. The optimization procedure was carried out in the sequence of the background function with six parameters, the histogram scale,  $2\theta$  shift then the lattice parameter by turning one parameter on at a time. Then the profile co-efficients were refined. In the initial cycles, only the parameters corresponding to a single atom were refined one by one. When the system was near convergence, all atom parameters were refined simultaneously to minimize the correlation between parameters of different atoms. As the present system under study belongs to *Pbnm* symmetry, fractional atom co-ordinates of general positions were only refined. This was followed by the refinement of the background parameters alone with higher order terms. After that, the site occupancy of different atomic species was refined one by one, with the constraint that the total concentration of Gd and Y in the sample at any time to be one (i.e.  $(1-x) + x = 1$ ). This followed simultaneous refinement of the unit cell parameters and site occupancies. The progress of the refinement process was reviewed by the calculated, observed and the difference intensity plots of the different stages of the refinement steps using the online plot facility of GSAS. Gross errors in scale factors, in the background level or shape or in lattice parameters, various kinds of profile misfits, including inadequate calculated

tail length, uncorrected asymmetry and profile broadening could be recognized at once in such plots but not so easily in the numerical output.

## References:

- [1]. Robert Alan Young, *The Rietveld method*, Oxford University Press (2002).
- [2]. A.C. Larson and R.B. Von Dreele, "General Structure Analysis System (GSAS)", *Los Alamos National Laboratory Report LAUR* **86**, 748 (1994).
- [3]. R. Bachmann, F. J. DiSalvo Jr., T. H. Geballe, R. L. Greene, R. E. Howard, C. N. King, H. C. Kirsch, K. N. Lee, R. E. Schwall, H.-U. Thomas and R. B. Zubeck, *Rev. Sci. Instrum.* **43**, 205 (1972).
- [4]. J. P. Perdew and Y. Wang, *Phys. Rev. B* **45**, 13244 (1992); J. P. Perdew, J. A. Chevary, S. H. Vosko, K. A. Jackson, M. R. Pederson, D. J. Singh, C. Fiolhais, *Phys. Rev. B* **46**, 6671 (1992); M. Itoh, H. Tanaka, Y. Watanabe, M. Udagawa and I. Sumita, *Phys. Rev. B* **47**, 2216 (1993), J.P. Perdew, A. Ruzsinszky, G.I. Csonka, O.A. Vydrov, G.E. Scuseria, L.A. Constantin, X. Zhou, and K. Burke, *Phys. Rev. Lett.* **100**, 136406 (2008).
- [5]. P. Blaha, K. Schwarz, G. K. H. Madsen, D. Kvasnicka and J. Luitz., *WIEN2K, An Augmented Plane Wave, Local Orbitals Program for Calculating Crystal Properties*, Karlheinz Schwarz, Technical Universität, Wien, Austria 2001 ISBN 3-9501031-1-2.
- [6]. M. N. Rao, N. Kaur, S. L. Chaplot, N. K. Gaur and R. K. Singh, *J. Phys.: Condens. Matter*, **21**, 355402 (2009).
- [7]. G.V. Lewis and C.R.A. Catlow, *J. Phys. C: Solid State Phys.*, **18**, 1149-1161 (1985).
- [8]. E. Kroumova, M.I. Aroyo, J.M. Perez-Mato, A. Kirov, C. Capillas, S. Ivantchev & H. Wondratschek, *Bilbao crystallographic server, useful database and tools for phase transition studies*, *Phase Transitions*, **76**, 155-170 (2003). <http://www.cryst.ehu.es/rep/sam.html>].
- [9]. J. A. Alonso, M. J. Martí'nez-Lope, M. T. Casais and M. T. Ferná'ndez-Dí'az, *Inorg. Chem.*, **39**, 917-923 (2000).
- [10]. P. Thompson, D. E. Cox & J. B. Hastings, *J. Appl. Cryst* **20**, 79-83 (1987).

[11]. C. J. Howard, *J. Appl. Cryst* **15**, 615 (1982).

[12]. G. Cagliotti, A. Pauletti and *F. P. Ricci*, *Nucl. Instrum. Methods* **3**, 223 (1958).

## Chapter 3

### Structural magnetization and specific heat studies on $\text{Gd}_{1-x}\text{Y}_x\text{MnO}_3$

#### 3.1. Introduction

The multiferroic properties as has been already described are closely related to the structural variations and distortions in  $\text{RMnO}_3$  system. The work of Kimura *et.al.* [1] had clearly brought out a correlation between average bond angle  $\langle\text{Mn-O-Mn}\rangle$ , ionic radius and magnetic ground state of the  $\text{RMnO}_3$  perovskites. It is proposed from earlier studies [2-4] that the onset of ferroelectric behaviour depends strongly on the magnetic ground state. The magnetic frustration brought in by the competing magnetic interaction as a direct result of the structural distortions and the R-Mn interaction results in the modulated magnetic structure of the  $\text{Mn}^{3+}$  sublattice in the  $\text{RMnO}_3$  perovskites. This results in the cycloidal magnetic ground state of the  $\text{Mn}^{3+}$  sublattice as seen in  $\text{TbMnO}_3$  and  $\text{DyMnO}_3$  [4]. The increase in magnetic frustration is a direct result of decrease of the Mn-O-Mn bond angle with decreasing rare earth ionic radius. The orthorhombic larger ionic radius rare earth have a A-type antiferromagnetic structure and this changes to long wavelength antiferromagnetic order with cycloidal magnetic ground state with decreasing Mn-O-Mn bond angle. The emergence of multiferroic property as a function of varying Mn-O-Mn bond angle in non-multiferroic, A-type antiferromagnetic ground state  $\text{RMnO}_3$  perovskite has been carried out by several groups. Substitution of Y at the Eu site in  $\text{EuMnO}_3$  and at Sm site in  $\text{SmMnO}_3$  has been reported. In both the cases substitution of Y decreases the average Mn-O-Mn bond angle and this parameter is attributed to the emergence of the multiferroic properties [1].  $\text{GdMnO}_3$  which is located in the vicinity of the phase boundary of A-type antiferromagnetic and long wavelength antiferromagnetic phase is an ideal system for

this kind of structural studies. Thus studying the structural variation on Y substituted  $\text{GdMnO}_3$  is an interesting problem to attempt. With this in mind, we have synthesized such specimens.

This chapter discusses the sample synthesis and investigations on the variation of lattice parameter and bond angles as a function of increasing Y concentration in  $\text{Gd}_{1-x}\text{Y}_x\text{MnO}_3$  ( $x=0.2, 0.3$  &  $0.4$ ). The variation in magnetization behaviour due to substitution is also studied, with a view of inducing cycloidal antiferromagnetic transition in the  $\text{Mn}^{3+}$  sublattice. This has been seen in  $\text{TbMnO}_3$  and known to arise due to the variation of the Mn-O-Mn bond angle. We carry out specific heat studies to identify the magnetic transition present in the system.

### **3.2. Sample synthesis**

Polycrystalline samples of  $\text{Gd}_{1-x}\text{Y}_x\text{MnO}_3$  ( $x=0, 0.2, 0.3$  &  $0.4$ ) were synthesized by solid state reaction route using  $\text{Gd}_2\text{O}_3$ ,  $\text{Y}_2\text{O}_3$  and  $\text{MnO}_2$  (Aldrich make, 99.95% pure). The precursor oxides were calcined at  $900^\circ\text{C}$  for 12 hr to remove adsorbed moisture. Homogeneously mixed precursors in stoichiometric ratio were heated in the temperature range from  $450^\circ\text{C}$  to  $1350^\circ\text{C}$  for a total duration of 72 hours with a few intermittent grinding. Powders were compacted into pellets of ( $\sim 10\text{mm}$  diameter and  $\sim 3\text{mm}$  thick) under a force of  $40\text{kN}$  and sintered at  $1350^\circ\text{C}$  for 12 hrs. During all the heat treatment steps, platinum foil was used to reduce the contamination. The SEM micrographs of the samples are shown in Fig. 3.1 All the samples exhibit large grains with well defined facets. The stoichiometry of the samples as estimated from EDX studies closely matches with the nominal composition.

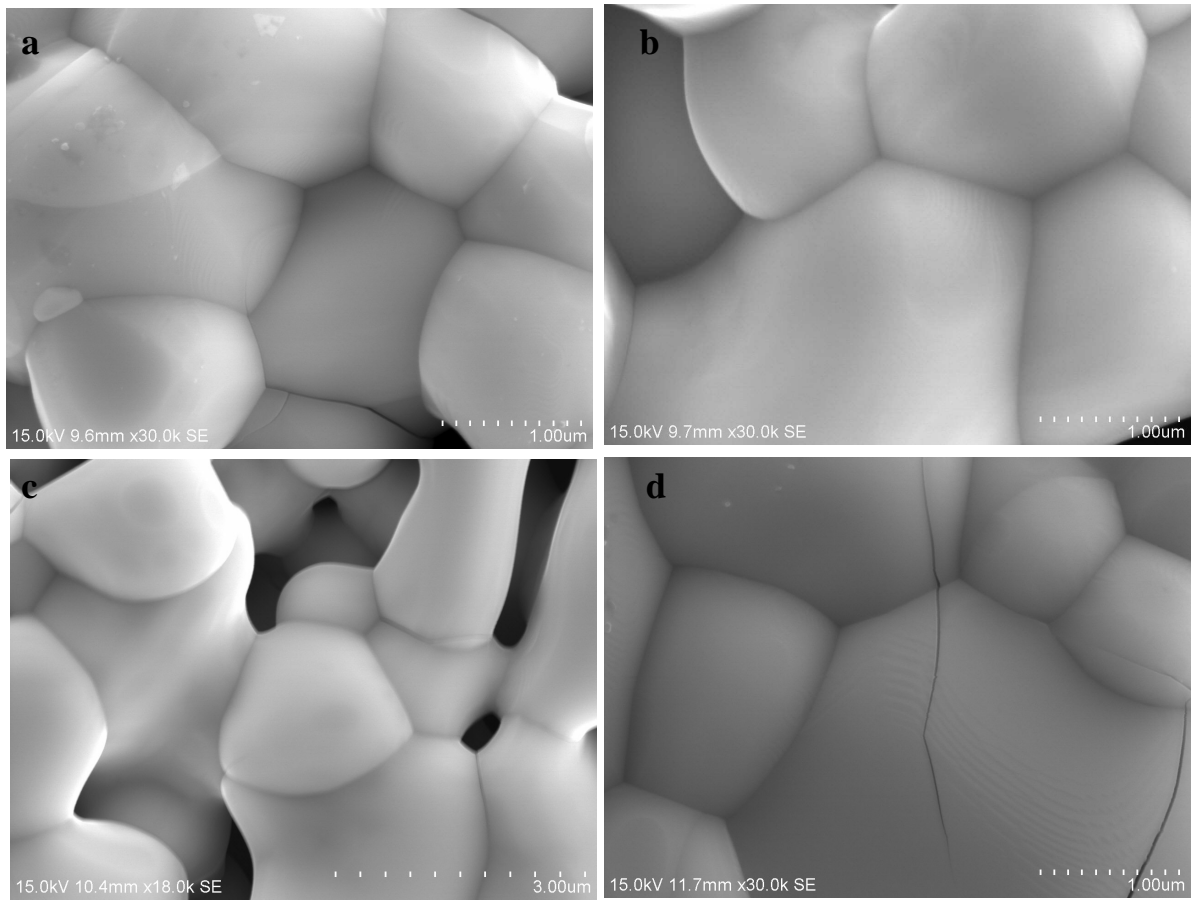


Figure.3.1: SEM micrographs of  $Gd_{1-x}Y_xMnO_3$  for a)  $x=0$ , b)  $x=0.2$ , c)  $x=0.3$  and d)  $x=0.4$ .

### 3.3. X-ray diffraction and structural studies

The room temperature XRD patterns of  $Gd_{1-x}Y_xMnO_3$  ( $x= 0.2, 0.3$  and  $0.4$ ) are shown in Fig.3.2. No impurity could be detected from the diffraction studies. The XRD pattern of  $GdMnO_3$  matches with reported diffraction pattern [5] and JCPDS (250337). The XRD pattern of  $x = 0$  composition is discussed in the next chapter with respect to low temperature XRD. Upon  $Y^{3+}$  substitution, the peak shift to higher angle indicating decrease of lattice parameters. The preliminary structural analysis was undertaken using Treor programme [6]. All the peaks could

be indexed to orthorhombic symmetry. The lattice parameter  $a$ ,  $b$ ,  $c$  and the unit cell volume obtained from this analysis were used as inputs for the Rietveld refinement analysis [7].

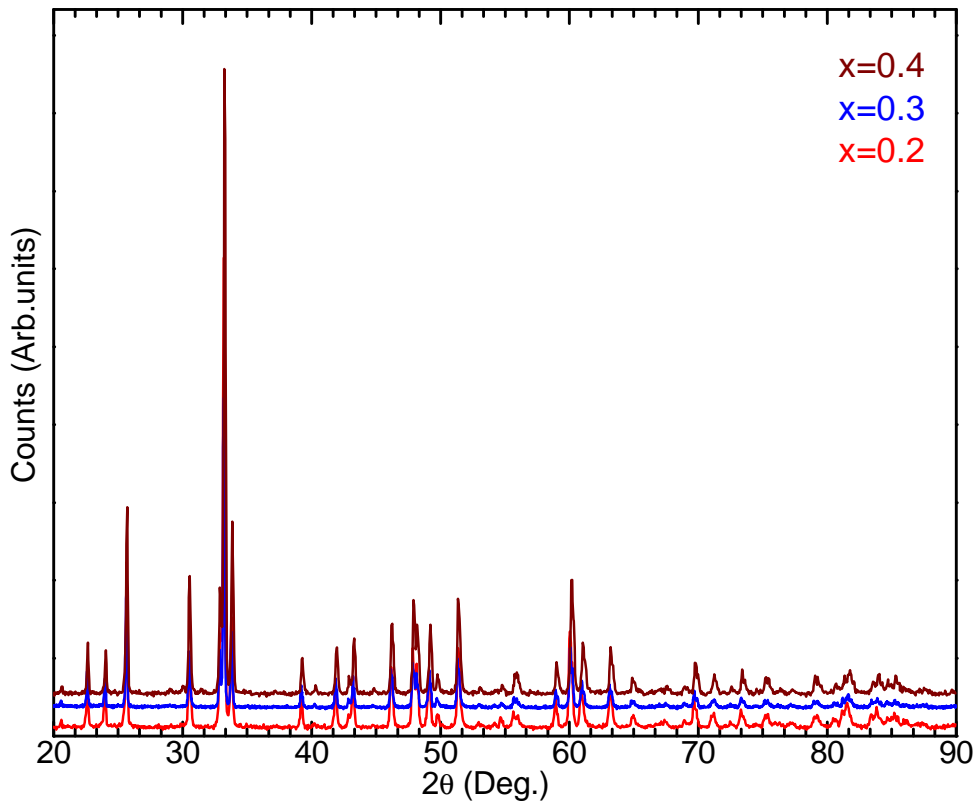


Figure.3.2: Room temperature XRD patterns of  $Gd_{1-x}Y_xMnO_3$  ( $x=0.2$ ,  $0.3$  and  $0.4$ ). The diffraction patterns are vertically shifted for clarity.

As a representative, measured X-ray diffraction pattern ( $\times$ ) along with calculated ( $—$ ) pattern, Bragg reflections ( $|$ ) and the difference ( $—$ ) patterns for  $Gd_{0.7}Y_{0.3}MnO_3$  is shown in Fig.3.3. Variations of lattice parameters with  $x$  are shown in Fig.3.4. While the lattice parameters  $a$  and  $c$  decreases almost linearly, non-linear decrease in the lattice parameter  $b$  is observed. Similar variation in  $b$ -axis was reported for such ortho-manganites [8]. However, the

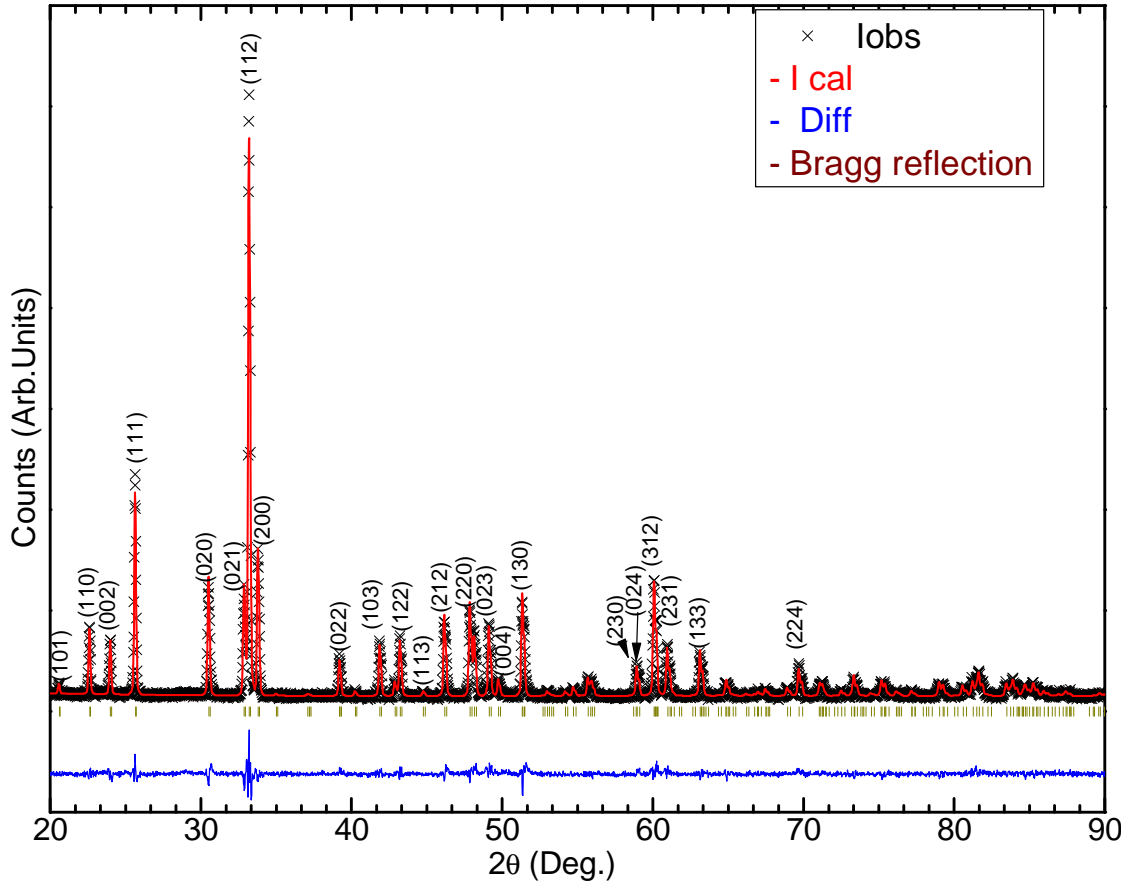


Figure.3.3: Measured X-ray diffraction pattern of  $\text{Gd}_{0.7}\text{Y}_{0.3}\text{MnO}_3$  along with fitted pattern; (x) - measured pattern, (—) - Calculated pattern; (—) – difference pattern and (|) – position of Bragg reflection.

relation,  $c/\sqrt{2} < a < b$  corresponding to O' distortion of the ortho-perovskite is obeyed for all  $x$ . A moderate increase in the orthorhombic distortion  $2(b - a)/(a + b)$  from 0.096 ( $\text{GdMnO}_3$ ) to 0.1 ( $\text{Gd}_{0.6}\text{Y}_{0.4}\text{MnO}_3$ ) is observed. Decrease of lattice parameter and unit cell volume with Yttrium substitution is due to the smaller ionic radius of  $\text{Y}^{3+}$  ion (1.075 Å) compared to that of  $\text{Gd}^{3+}$  ions (1.107 Å) [9]. Smaller ionic radius of  $\text{Y}^{3+}$  results in rotation or/and tilting of the octahedron leading to reduction in  $Mn-O-Mn$  bond angle and  $Mn-O$  bond lengths,  $d_{Mn-O}$ .  $Mn-O$

Bond lengths and *Mn-O-Mn* bond angles along with other crystallographic parameters of  $Gd_{1-x}Y_xMnO_3$  are presented in Table 3.1. It is seen that octahedron tilt angle defined by

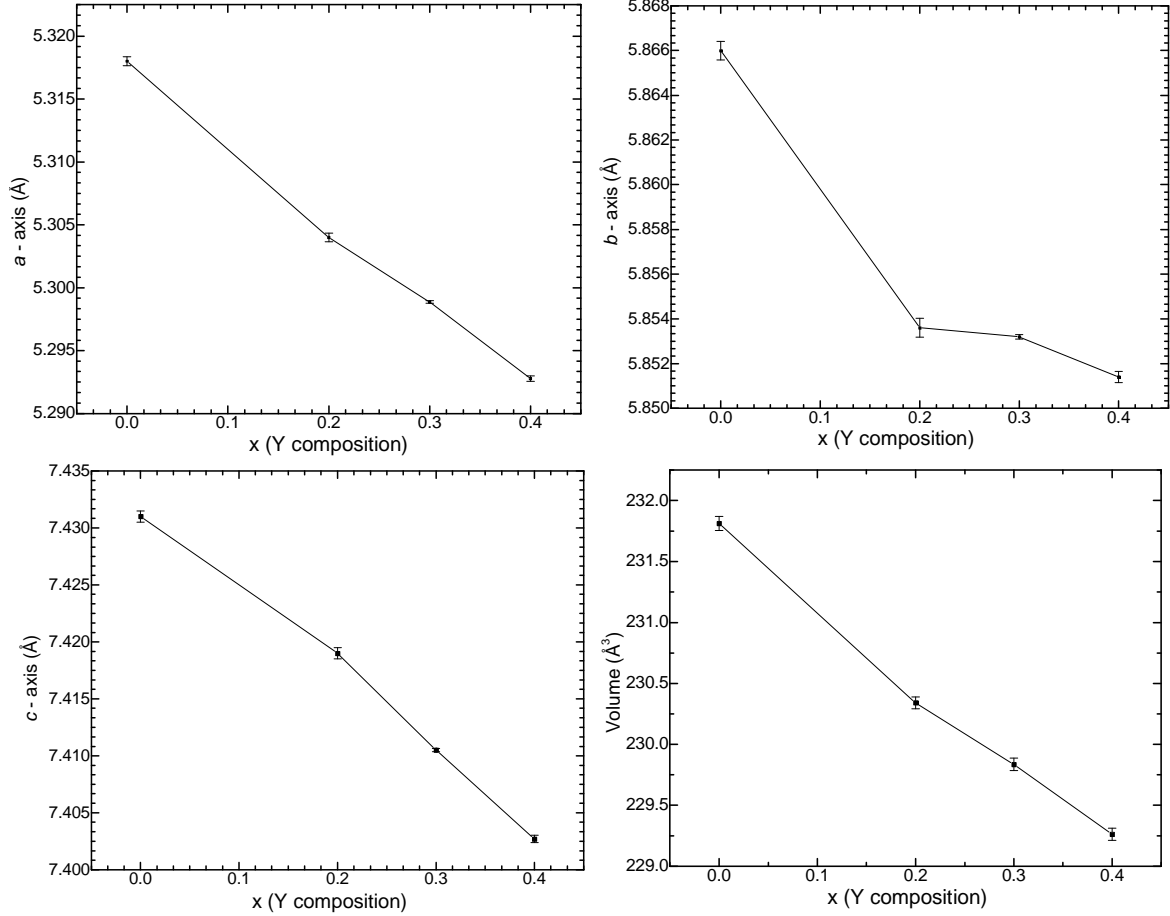


Figure.3.4: Variation in the lattice parameters  $a$ ,  $b$ ,  $c$  and unit cell volume with Y concentration ( $x$ ). Lines are drawn as a guide to the eye

$\theta = (180 - (Mn - O1 - Mn))/2$  increases by about 0.51% upon 40 at.% substitution of  $Y^{3+}$ . On the other hand, for the same substitution average *Mn-O2-Mn* bond angle undergoes larger reduction of 1.67% in the *ab*-plane. Importantly, the estimated average bond angles closely match with that  $TbMnO_3$  and falls within range of bond angle values for observing spontaneous ferroelectric polarization [1]. Thus, the present systems are expected to exhibit modulation in

magnetic structure. This in the presence of magneto-elastic coupling could lead to an improper ferroelectric transition, quite similar to that of  $\text{TbMnO}_3$ . This argument finds support in the recent work on  $\text{Sm}_{1-x}\text{Y}_x\text{MnO}_3$  system [10].

	$\text{Gd}_{0.8}\text{Y}_{0.2}\text{MnO}_3$	$\text{Gd}_{0.7}\text{Y}_{0.3}\text{MnO}_3$	$\text{Gd}_{0.6}\text{Y}_{0.4}\text{MnO}_3$
$a$ (Å)	5.3048(3)	5.2988(1)	5.2927(2)
$b$ (Å)	5.8536 (4)	5.8532(1)	5.8511(3)
$c$ (Å)	7.4190 (4)	7.4105(1)	7.4027(3)
Mn-O1-Mn (Deg.)	145.918 (3)	145.537 (1)	145.166 (2)
$\langle\text{Mn-O2-Mn}\rangle$ (Deg.)	145.433 (1)	144.299 (1)	143.042 (1)
$\langle\text{Mn-O-Mn}\rangle$ (Deg.)	145.594 (2)	144.711 (1)	143.75 (2)
Gd/Y 4c ( $x, y, 1/4$ )			
$x$	0.9849	0.9836	0.9829
$y$	0.0816	0.0815	0.0812
Mn 4b ( $1/2, 0, 0$ )			
O1 4c ( $x, y, 1/4$ )			
$x$	0.1020	0.1022	0.1024
$y$	0.4702	0.4672	0.4644
O2 8d ( $x, y, z$ )			
$x$	0.7049	0.7030	0.6995
$y$	0.326	0.3270	0.3282
$z$	0.0515	0.05424	0.0563
$R_w$	0.1589	0.0855	0.131
$\chi^2$	7.751	1.686	6.565

Table 3.1: Estimated lattice parameters, bond angles, fractional co-ordinates of the atoms for  $\text{Gd}_{1-x}\text{Y}_x\text{MnO}_3$  ( $x = 0.2, 0.3$  &  $0.4$ ) in orthorhombic symmetry belonging to  $Pbnm$  space group.

### 3.4. Thermomagnetisation and M-H studies

The magnetic properties of  $\text{Gd}_{1-x}\text{Y}_x\text{MnO}_3$  ( $x = 0.2, 0.3$  &  $0.4$ ) have been investigated by measuring the thermomagnetization and the magnetization at fixed temperatures. The thermomagnetization studies with an applied field of 200 Oe were carried out both in zero field cooled (ZFC) and field cooled (FC) mode over the temperature range 300 to 5 K. Negligible difference between the ZFC and FC curves is observed for all the compositions. The

thermomagnetization curve of all the samples shows a monotonous increase in magnetisation with decrease in temperature, devoid of specific features of magnetic transitions. However, earlier magnetization studies on *single crystals* of R-site substituted  $\text{RMnO}_3$  systems indicate diminutive yet clear signature of magnetic transitions of  $\text{Mn}^{3+}$  sublattice. Coupled with inherent

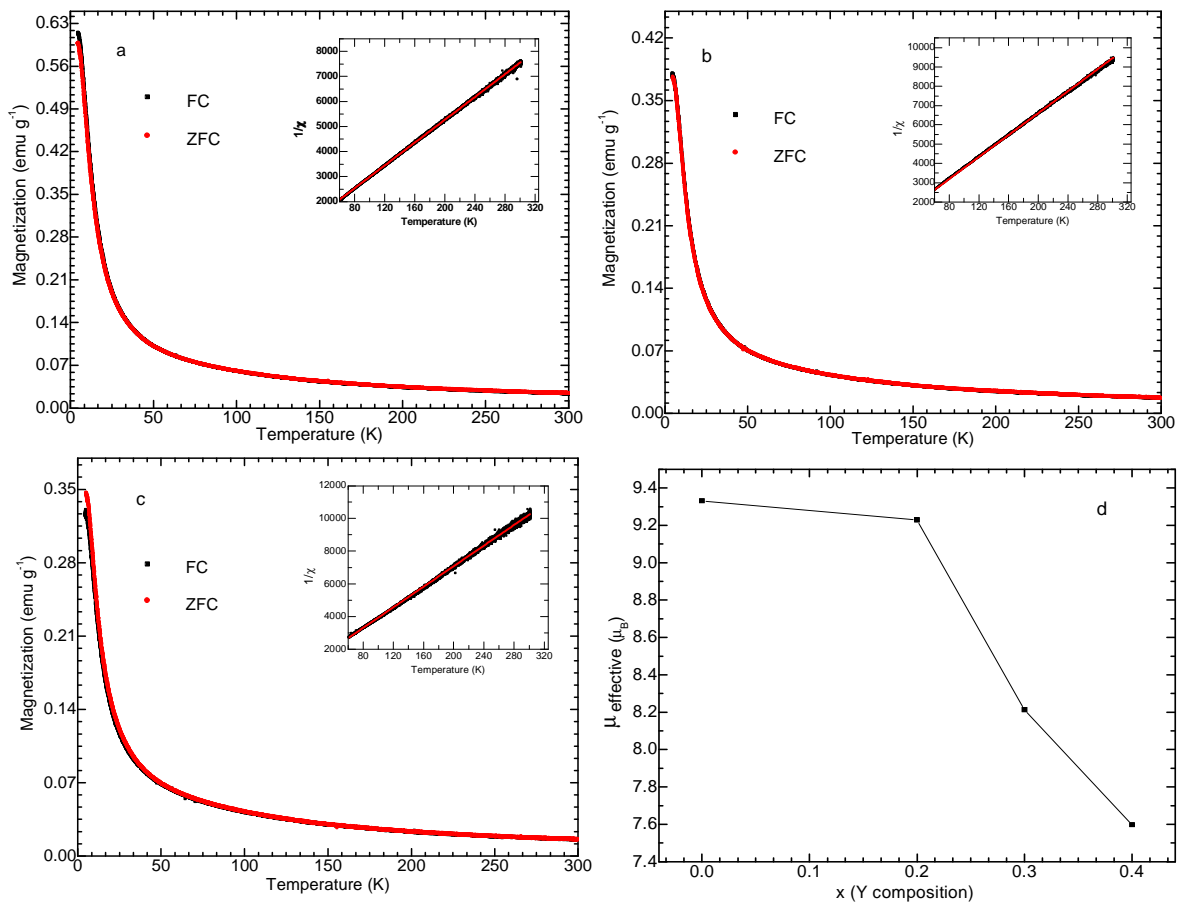


Figure.3.5: Figure showing the FC and ZFC curves and inset showing the fitting of  $1/\chi$  vs T with Curie-Weiss law for a)  $x=0.2$ , b)  $x=0.3$ , c)  $x=0.4$  and d) effective magnetic moment for all composition.

large anisotropy, these features might have been obliterated in the case of *polycrystalline* samples. Additionally, substantial paramagnetic contribution of  $\text{Gd}^{3+}$ -sublattice to the

magnetization at these temperatures could have compounded the problem as has been reported for other RMnO<sub>3</sub> systems [10].

As such, expected magnetic transitions of Mn<sup>3+</sup>-sublattice could not be ascertained from thermomagnetization studies. The inverse susceptibility (insets) vs. temperature plots exhibit linearity down to ~ 55 K and takes a negative deviation below this temperature. The linear portion of the inverse susceptibility curve ( $T > 75$  K) was fitted with Curie-Weiss equation to estimate the Curie-Weiss constant and Weiss temperature ( $\theta$ ).  $\theta$  almost linearly decreases from -32 K for  $x=0.2$  to -22 K for  $x=0.4$ . This is in agreement with a reduction in the value of  $\langle Mn-O-Mn \rangle$  with Y substitution, which decreases next nearest neighbour antiferromagnetic interaction strength in relation to the nearest neighbour ferromagnetic interaction strength between Mn<sup>3+</sup> spins in the *ab*-plane. The effective magnetic moments  $\mu_{\text{eff}}$  was calculated from the Curie-Weiss constant and its variation as a function of  $x$  is plotted Fig. 3.5.

The M-H curves have been measured at 20, 10 and 5K in an applied magnetic field range of -10 to 10T and are shown in Fig.3.6. For all the composition, M-H curves exhibits a knee without saturation. For a given system, magnetization at a given magnetic field increases with lowering temperature, in accordance with thermomagnetization studies. Also, magnetization (Fig. 3.6d) measured at 5 K decreases with  $x$ , in accordance with magnetic dilution effect. At 5K the increase is more drastic and this could be due to the Gd<sup>3+</sup> ordering. Also the magnetization increases rapidly beyond 1.5T at 5K, a partial knee like variation of the M-H curve is seen. This could be attributed to the magnetic transition of the Gd<sup>3+</sup> sublattice from canted anti-ferromagnetic to ferromagnetic in an applied magnetic field above 1.5T. This has been reported for other RMnO<sub>3</sub> system and is more pronounced in case of single crystals [11]. The

magnetization value for 5K is seen to decrease with increasing Y, due to dilution of  $Gd^{3+}$ . Magnetization curves of single crystals of  $RMnO_3$  recorded below the magnetic transition temperature of R-sublattice exhibit a sharp increase in magnetization above a critical field [12]. This is attributed to a field-induced first-order metamagnetic transition from AFM to FM state. Such a feature is not observed in the present study owing to polycrystalline nature of the sample.

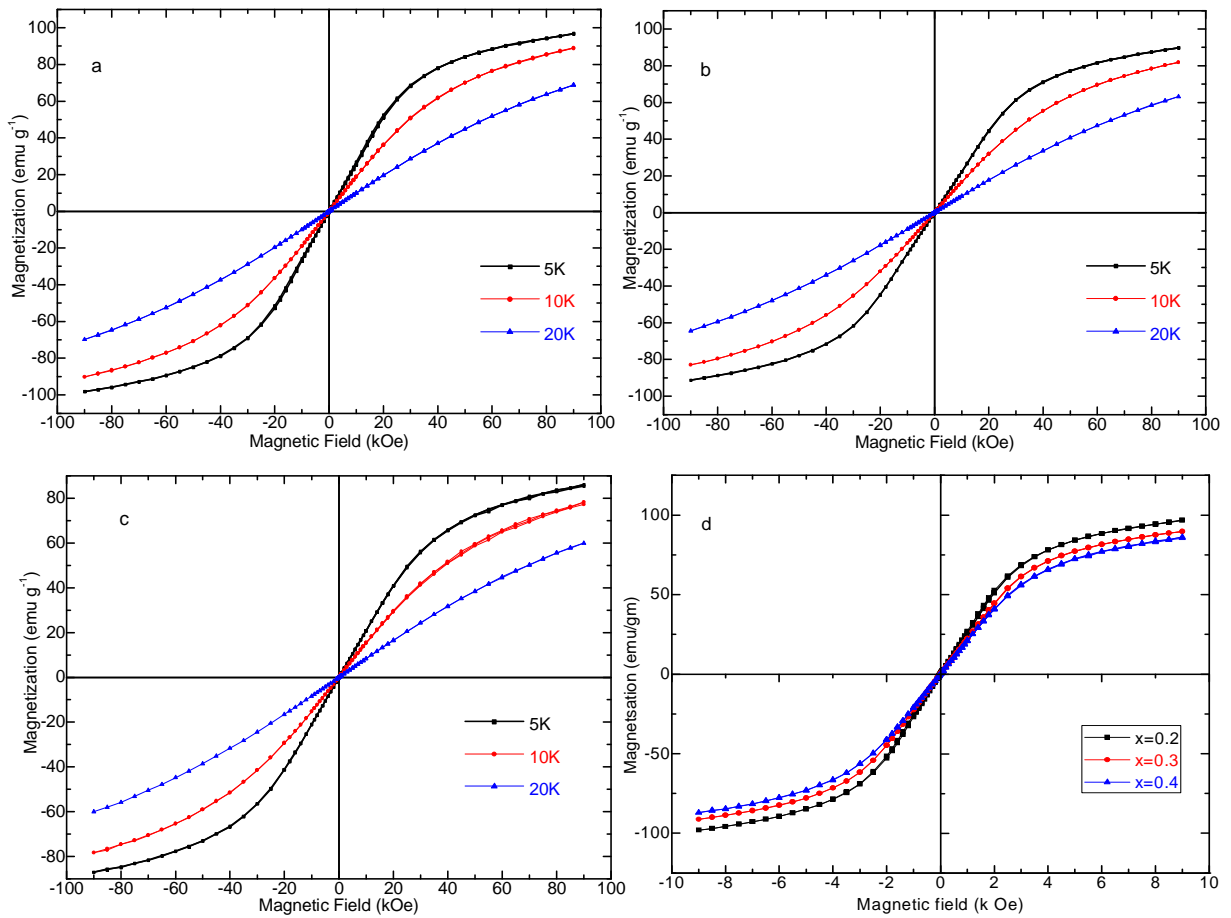


Figure.3.6: M-H curves at 20, 10 and 5K for a)  $x=0.2$ , b)  $x=0.3$ , c)  $x=0.4$  and d) M-H curves for all composition at 5K

### 3.5. Specific heat studies

With a view to find out the magnetic transition of the  $\text{Mn}^{3+}$  and  $\text{Gd}^{3+}$  sublattices, specific heat measurements were under taken both in presence and in absence of magnetic field. Specific heat measurements were carried out on powdered samples of  $\text{Gd}_{1-x}\text{Y}_x\text{MnO}_3$  ( $x = 0.2, 0.3$  &  $0.4$ ) using a physical property measurement system (Quantum Design, USA). The measurements were done in an applied field of 0, 0.5, 5 and 10T in the temperature range of 60 to 4K.  $C_p/T$  vs. T curves for all the systems are plotted in Fig. 3.7. All the compositions show a lambda like anomaly about 41K corresponding to a paramagnetic to sinusoidal antiferromagnetic transition of the  $\text{Mn}^{3+}$  sublattice (MT1) and is reported for the parent compound  $\text{GdMnO}_3$  about 43K [4]. This anomaly down shifts approximately by 2K as  $x$  is increased to 0.4.

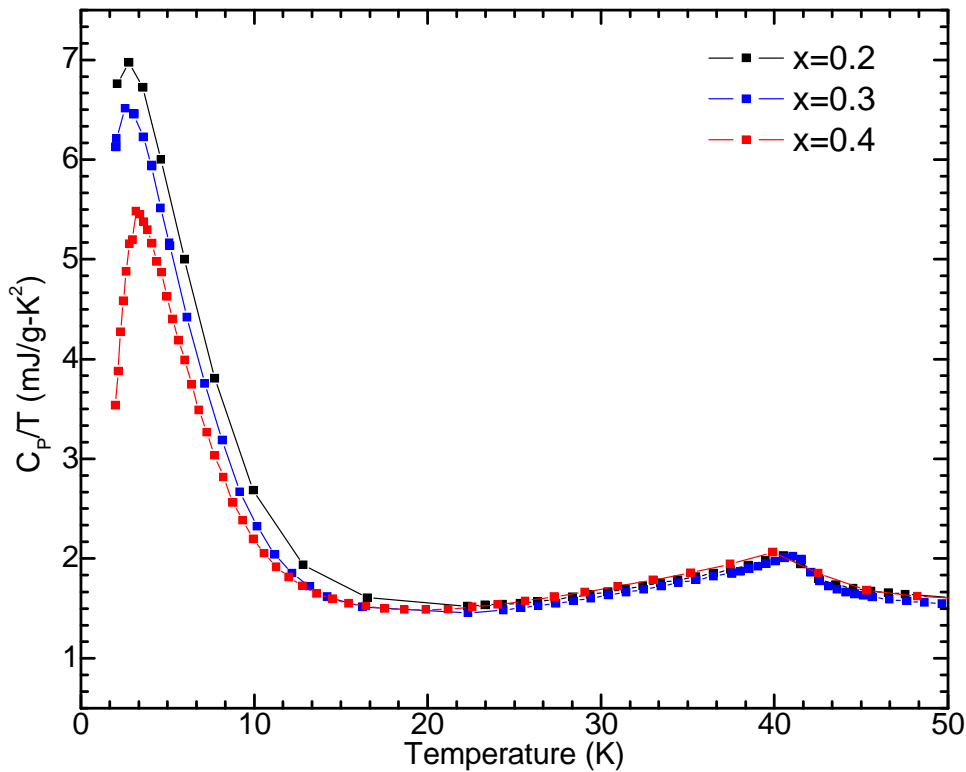


Figure.3.7:  $C_p/T$  vs T plot for  $\text{Gd}_{1-x}\text{Y}_x\text{MnO}_3$   $x = 0.2, 0.3$  &  $0.4$

This should be contrasted against observed lowering of  $\theta$  about 10 K for the same change in  $x$ . This indicates that the frustration defined by  $\theta/T_N$  increases with  $Y^{3+}$  substitution. Apart from this, much stronger anomaly is observed about 5K. This is attributed to the paramagnetic to canted antiferromagnetic transition of the  $Gd^{3+}$  sublattice and is not affected by Y substitution. Other than this signature corresponding to magnetic transitions could be observed except for  $x=0.3$ , due significant contribution from the  $Gd^{3+}$ -sublattice. The feeble anomaly is observed around 18K for  $x = 0.3$  composition which increases in magnitude with applied magnetic field as shown in Fig. 3.8. It is proposed that this could be ascribed to the sinusoidal to cycloidal anti-ferromagnetic transition of the  $Mn^{3+}$  sublattice as seen in  $TbMnO_3$  [2].

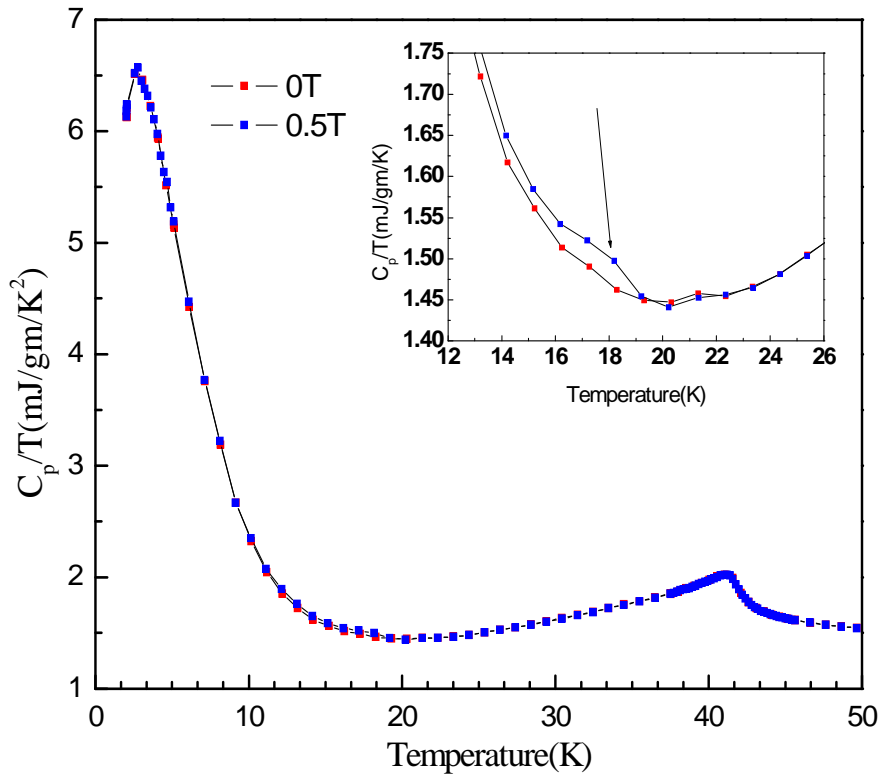


Figure.3.8:  $C_p/T$  vs.  $T$  plot for  $Gd_{0.7}Y_{0.3}MnO_3$  with the inset showing a feeble anomaly at 18K attributed to sinusoidal to cycloidal antiferromagnetic transition of  $Mn^{3+}$  sublattice.

### 3.6. Conclusions

Polycrystalline samples of  $\text{Gd}_{1-x}\text{Y}_x\text{MnO}_3$  ( $x = 0.2, 0.3$  &  $0.4$ ) were synthesized in single phase. All the peaks in the XRD patterns could be indexed to the orthorhombic symmetry belonging to  $Pbnm$  space group. The lattice parameter is found to decrease with increasing Yttrium concentration. The bond angle is found to decrease with Y and fall in a window of favorable values [1] for emergence of multiferroic property.

The thermomagnetisation curves of all the samples were observed to monotonically increase with decrease of temperature and are devoid of any features. The inverse susceptibility plot of  $1/\chi$  vs.  $T$  decreases linearly down till 55K and deviates from linearity below it. The Curie constant, Weiss temperature and effective magnetic moment was estimated by fitting the linear portion of the inverse susceptibility curve above 75K. The effective magnetic moment and the Weiss temperature decrease with Y concentration due to dilution of  $\text{Gd}^{3+}$  ions with non-magnetic  $\text{Y}^{3+}$  ions.

The specific heat measurements show strong anomalies about 41 and 5K corresponding to a paramagnetic sinusoidal antiferromagnetic transition of the  $\text{Mn}^{3+}$  sublattice (MT1) and to a paramagnetic to canted antiferromagnetic transition (MT3) of the  $\text{Gd}^{3+}$  sublattice respectively. While MT1 marginally decreases by 2K, no change was observed for MT3. Additional feeble anomaly was observed near 18 K for the  $x = 0.3$ . The magnitude of this anomaly was seen to increase with magnetic field. Based on estimated  $\langle\text{Mn-O-Mn}\rangle$  bond angle and earlier works, this anomaly is associated with the sinusoidal to cycloidal AFM transition of the  $\text{Mn}^{3+}$  sublattice. The specific heat measurement also shows features of magnetic transitions like that found in  $\text{TbMnO}_3$ , though they could not be clearly observed due to higher magnetic moment of the  $\text{Gd}^{3+}$

ion. Further studies like dielectric spectroscopy and low temperature XRD may give better understanding and are discussed in the next chapter.

## References:

- [1]. T. Kimura, S. Ishihara, H. Shintani, T. Arima, K. T. Takahashi, K. Ishizaka, and Y. Tokura, *Phys. Rev. B* **68**, 060403R (2003).
- [2]. Kimura, T., Goto, T., Shintani, H., Ishizaka, K., Arima, T., and Tokura, Y. *Nature* **426**, 55 (2003)
- [3]. Hur, N., Park, S., Sharma, P. A., Ahn, J. S., Guha, S., and Cheong, S.-W. *Nature* **429**, 392 (2004).
- [4]. T. Kimura, G. Lawes, T. Goto, Y. Tokura and A. P. Ramirez, *Phys. Rev. B* **71**, 224425 (2005).
- [5]. G. Q. Zhang, S. J. Luo, S. Dong, Y. J. Gao, K. F. Wang and J.-M. Liu, *J. Appl. Phys.* **109**, 07D901 (2011).
- [6]. Werner P.E., Erikson L. and Westdahl M.C., *J. Appl. Cryst.* **18** 367(1985).
- [7]. Robert Alan Young, *The Rietveld method*, Oxford University Press (2002).
- [8]. J. A. Alonso, M. J. Martínez-Lope, M. T. Casais, and M. T. Fernández-Díaz, *Inorg. Chem.* **39** 917 (2000).
- [9]. R. D. Shannon and C. T. Prewitt, *Acta Crystallogr. B* **25**, 725 (1969); **26**, 1046 (1970).
- [10]. D. O'Flynn, C. V. Tomy, M. R. Lees, A. Daoud-Aladine, and G. Balakrishnan, *Phys. Rev. B* **83**, 174426 (2011).
- [11]. Jin-Ling Jin, Xiang-Qun Zhang, Guo-Ke Li, Zhao-Hua Cheng, Lin Zheng and Yi Lu, *Phys. Rev. B* **83**, 184431 (2011).
- [12]. A. Midya, S. N. Das, P. Mandal, S. Pandya and V. Ganesan, *Phys. Rev. B* **84**, 235127 (2011).

## CHAPTER 4

### Dielectric and powder XRD studies at low temperature

#### 4.1. Introduction

The discovery of multiferroic property in  $\text{TbMnO}_3$  by Kimura et.al [1] and in  $\text{DyMnO}_3$  [2] has shown that the onset of incommensurate modulated magnetic structure (spiral/cycloidal) gives rise to spontaneous polarization. The presence of a sharp peak in the temperature dependent dielectric constant  $\epsilon(T)$  curve is shown as a clear evidence of ferroelectric transition. Goto *et.al.* have clearly indicated that the a sharp peak exist in the temperature dependent dielectric constant along the  $a$ -axis as well as along the  $c$ -axis both in  $\text{TbMnO}_3$  and  $\text{DyMnO}_3$  at temperature where spontaneous polarization emerges. Not much of variation is observed in dielectric constant along the  $b$ -axis. On the other hand, a step-like feature is seen along the  $a$ -axis and  $c$ -axis for paraelectric  $\text{GdMnO}_3$  and  $\text{EuMnO}_3$  at sinusoidal to A-type anti ferromagnetic transition temperature. More over in the study of solid solution of  $\text{Tb}_{1-x}\text{Gd}_x\text{MnO}_3$  [3] it is clearly shown that the a sharp peak exist along the  $c$ -axis in  $\epsilon(T)$  for concentration upto  $x \leq 0.6$  with polarization along  $c$ -axis. As the concentration of Gd is increased from 0.6 to 0.8 a sharp peak in temperature dependent dielectric constant emerges along the  $a$ -axis with polarization flipping along the  $a$ -axis. This is associated to the flipping of the spiral magnetic moments of the  $\text{Mn}^{3+}$  ions from  $bc$ -plane to  $ab$ -plane. Along with this a step like feature is also observed for this concentration along the  $a$ -axis in  $\epsilon(T)$  which becomes dominant beyond  $x > 0.8$ . This is associated to a reentrant paraelectric phase and the system becomes completely paraelectric beyond  $x > 0.8$ . Thus, it is evident that a sharp peak rather than a step in  $\epsilon(T)$  at the metamagnetic transition specifies a ferroelectric transition. Such features has been reported for

$\text{Gd}_{1-x}\text{Y}_x\text{MnO}_3$  [4] for  $x=0.1$  and  $0.2$ .  $\text{GdMnO}_3$  also has interesting features associated with structural distortions and dielectric effect [5] More over several relaxation process present in the system can also be studied by analysing the real and imaginary part of  $\epsilon(T)$  which may provide insight about the understanding of magnetic and ferroelectric transition. It has been reported that dielectric relaxation changes across magnetic transition [2, 6, 7] evidenced by change in activation energy. Thus in view of this it will be interesting to study such behaviours and relaxation process in the present system  $\text{Gd}_{1-x}\text{Y}_x\text{MnO}_3$  ( $x = 0.2, 0.3$  &  $0.4$ ). It has been reported that temperature dependent lattice parameter show anomalous variation near the magnetic transition, evidencing magneto-elastic coupling [8]. Hence low temperature XRD studies would throw more light on the presence of magneto-elastic coupling in the present system. In general it is observed that multiferroic materials exhibit large magneto-caloric effect (MCE) at low temperature and exhibit both normal and inverse MCE [9, 10]. Historically Gd [11] based materials have higher magneto-caloric effect, hence in light of all these  $\text{Gd}_{1-x}\text{Y}_x\text{MnO}_3$  ( $x= 0.2, 0.3$  &  $0.4$ ) forms an excellent system to study all the above phenomena.

## 4.2. Dielectric spectroscopic studies

Dielectric properties of  $\text{Gd}_{1-x}\text{Y}_x\text{MnO}_3$  ( $x = 0.2, 0.3$  &  $0.4$ ) were studied by impedance spectroscopy. Dielectric measurements were carried out in a temperature interval of 5 to 60 K over a frequency range  $10^1$  to  $10^6$  Hz. This temperature range covers the magnetic transition temperatures of  $\text{Gd}^{3+}$  and  $\text{Mn}^{3+}$ -sublattices. The temperature dependant real part of the dielectric constant  $\epsilon'(T)$  for all the compositions measured at different frequencies are shown in Fig. 4.1. For the sake of comparison,  $\epsilon'(T)$  measured at 10 kHz for  $x = 0.2, 0.3$  and  $0.4$  are shown in Fig.4.1(d). These matches with that of the  $\epsilon(T)$  dielectric curve along  $a$ -axis for  $\text{RMnO}_3$  [2]. For

all compositions and frequencies, an anomaly in the form of a peak around  $\sim 18\text{K}$  and a weak shoulder at  $\sim 7\text{K}$  are observed. The peak at  $18\text{K}$  down shifts marginally by  $2\text{K}$  as  $x$  is increased from  $0.2$  to  $0.4$ . However, there is no detectable change in the position of the shoulder with  $x$ . The width of the peak substantially increases with substitution that the shoulder ( $\sim 7\text{K}$ ) which is relatively well resolved for  $x = 0.2$ , is barely seen for  $x = 0.4$ . This may be ascribed to site disorder due to Y-substitution.

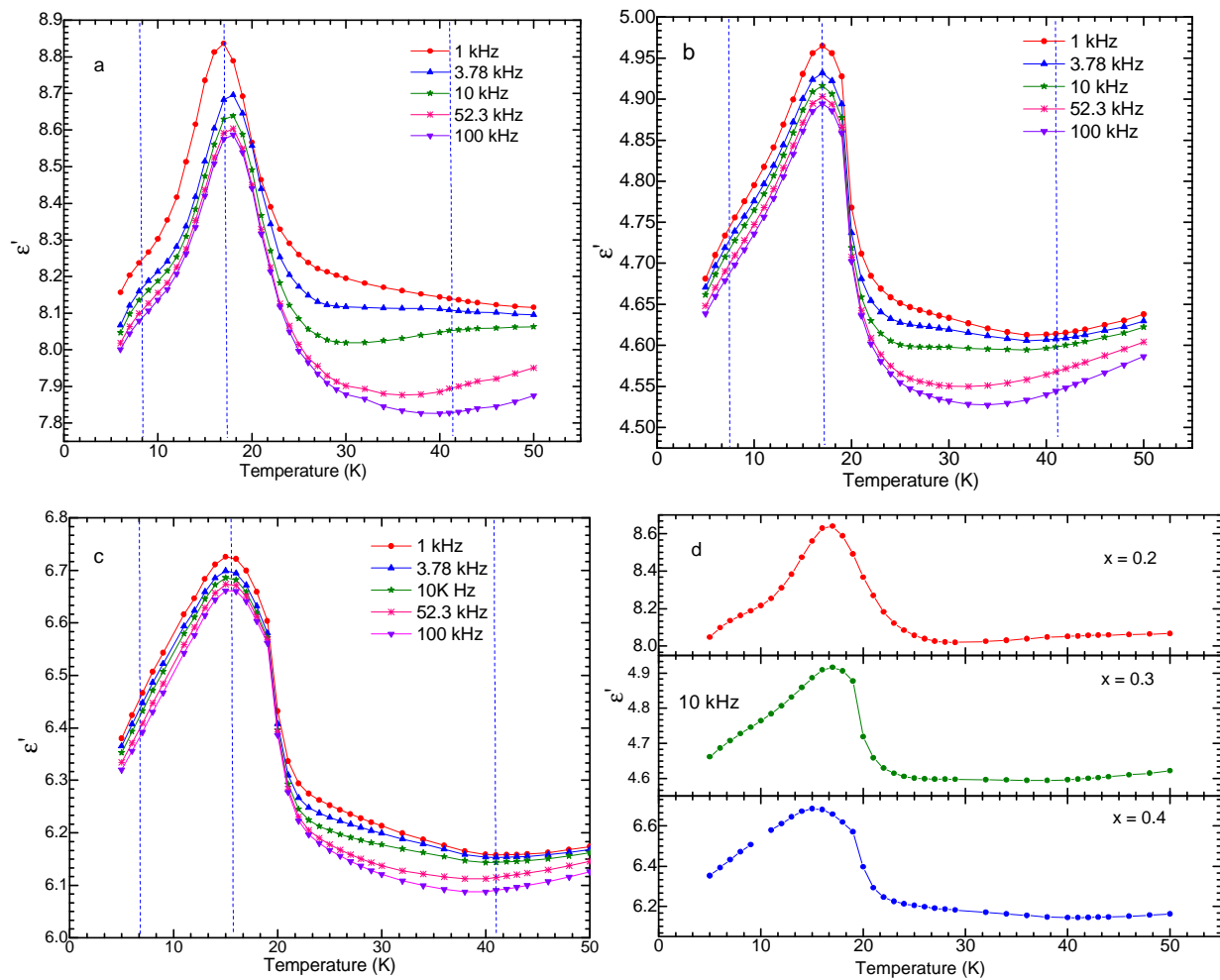


Figure.4.1: Variation of real part of dielectric permittivity with temperature  $\epsilon'(T)$  for  $\text{Gd}_{1-x}\text{Y}_x\text{MnO}_3$ : a)  $x=0.2$ , b)  $x=0.3$  c)  $x=0.4$  for various frequencies, d) comparison of  $\epsilon'(T)$  measured at  $10\text{ kHz}$  for  $x=0.2$ ,  $0.3$  and  $0.4$ . Vertical line corresponds to magnetic transition temperatures of  $\text{Mn}^{3+}$  and  $\text{Gd}^{3+}$  sublattice.

In the parent compound  $\text{GdMnO}_3$ , a step like anomaly at  $\sim 23\text{K}$  has been reported, associated to an incommensurate sinusoidal to an A-type antiferromagnetic transition [2] which retains the system in paraelectric phase. Corresponding to this temperature, the temperature dependant modulation wave vector abruptly drops from finite value ( $K_l^{Mn} \sim 0.39$ ) to zero, rendering the ground state to be paraelectric [12]. Under the influence of magnetic field the ground state changes to ferroelectric and the step like feature in  $\epsilon'(T)$  modifies to a peak. In general, a peak in  $\epsilon'(T)$  is seen in multiferroic  $\text{RMnO}_3$  like  $\text{TbMnO}_3$  and  $\text{DyMnO}_3$  and in  $(\text{RR}')\text{MnO}_3$  like  $\text{Eu}_{1-x}\text{Y}_x\text{MnO}_3$  and  $\text{Sm}_{1-x}\text{Y}_x\text{MnO}_3$  and  $\text{Tb}_{1-x}\text{Gd}_x\text{MnO}_3$  [1-3]. Additionally from the structural studies presented in the previous chapter, it is seen that the average  $\langle \text{Mn-O-Mn} \rangle$  bond angles of  $\text{Gd}_{1-x}\text{Y}_x\text{MnO}_3$  system fall in a window range that is favourable for observing multiferroic properties in the present system. Thus it is seen that Y substitution in  $\text{GdMnO}_3$  induces ferroelectric transition in  $\text{Gd}_{1-x}\text{Y}_x\text{MnO}_3$  system about 17 K. Accordingly, the peak is ascribed to metamagnetic transition of  $\text{Mn}^{3+}$ -sublattice, MT2. The site disorder due to Y-substitution, deduced from the broadened ferroelectric transition, is not strong enough to alter the nature of the transition to relaxor type. This is clearly evidenced from the fact that the position of the peak in  $\epsilon'(T)$  is unaltered with frequency. Moderate decrease in the strength of the anomaly with frequency is noticed. This is in accordance with the reported reduction in the strength of dielectric constant measured along  $c$ -axis with frequency for other  $\text{RMnO}_3$  compounds [2].

The shoulder observed in the real part of the dielectric constant is due to the magnetic ordering of the  $\text{Gd}^{3+}$  sublattice (MT3) from paramagnetic to canted antiferromagnetic [13,14]. This is a clear indication that the rare earth magnetic ordering also affects the dielectric permittivity and has been reported for the parent compound  $\text{GdMnO}_3$  [2]. The position of the peak is not affected by both frequency and Y-substitution. However, no feature associated with

the paramagnetic to sinusoidal anti ferromagnetic transition (MT1) of the  $Mn^{3+}$  sublattice could be observed. This is in agreement with earlier work on  $RMnO_3$  systems [2].

Temperature dependant imaginary part of the dielectric constant  $\epsilon''(T)$  measured under different frequencies for all the compositions are shown in Fig. 4.2. For ease of comparison,  $\epsilon''(T)$  measured at 10 kHz for  $x=0.2, 0.3$  and  $0.4$  are also presented. Striking effects of frequency on  $\epsilon''(T)$  is more apparent than in the case of  $\epsilon'(T)$ .

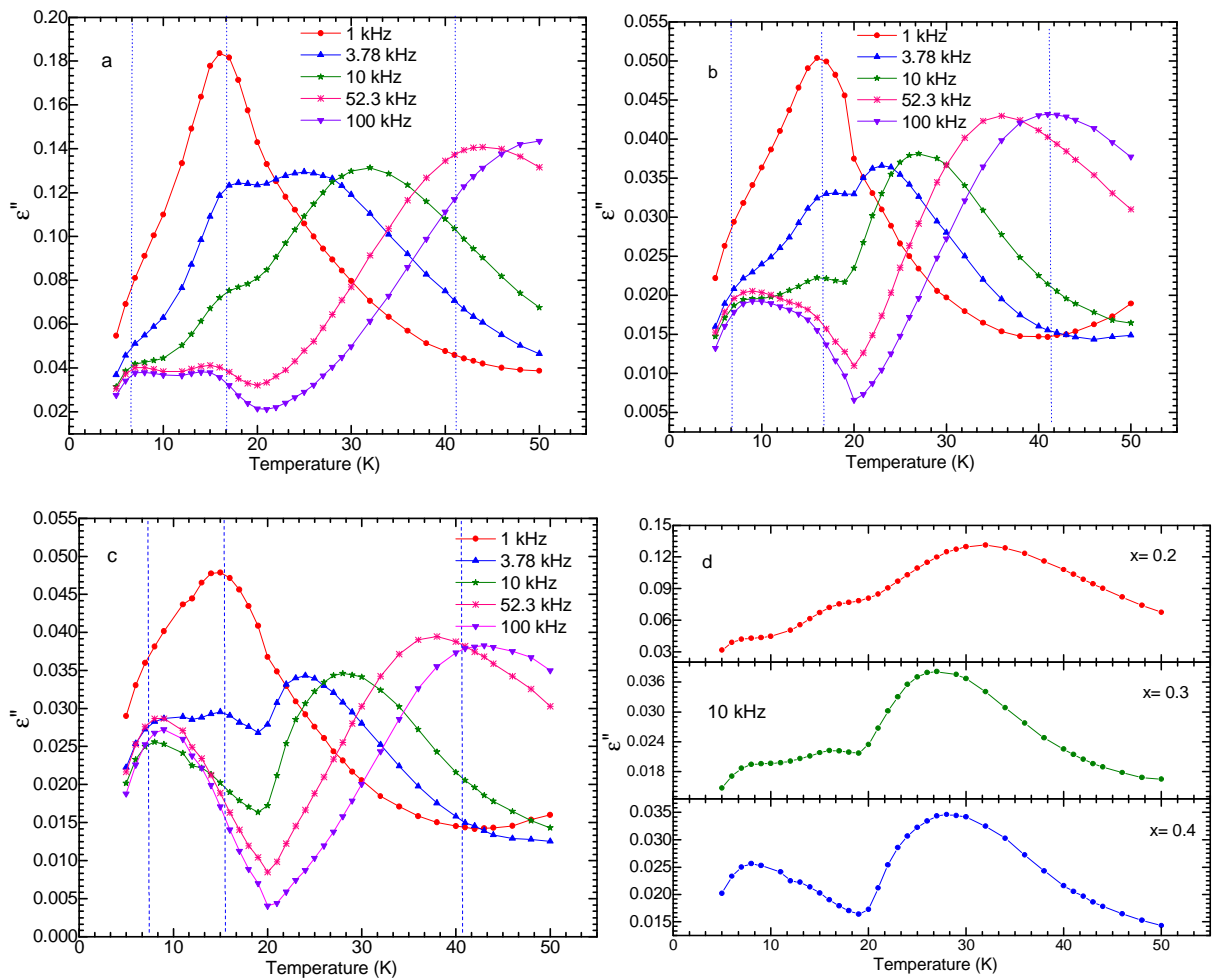


Figure.4.2: Variation of imaginary part of dielectric permittivity with temperature  $\epsilon''(T)$  for  $Gd_{1-x}Y_xMnO_3$ : a)  $x=0.2$ , b)  $x=0.3$  c)  $x=0.4$  for various frequencies d) comparison of  $\epsilon''(T)$  measured at 10 kHz for  $x=0.2, 0.3$  and  $0.4$ . Vertical lines correspond to magnetic transition temperatures of  $Mn^{3+}$  and  $Gd^{3+}$  sublattice.

As in the case of  $\epsilon'(T)$ , two anomalies are observed about 7 and 18 K. As had been inferred above, these anomalies are associated to relaxation processes related to MT3 and MT2 of  $Gd^{3+}$ - and  $Mn^{3+}$ -sublattices respectively. While the peak associated with MT2 a down shift to  $\sim 2K$  with composition, no detectable change is observed in the position of the anomaly related to MT3. Additionally, considerable suppression in the strength of the anomaly associated with MT2 is seen. This reduction renders the contribution of  $Gd^{3+}$  sublattice to be distinct.

For  $f \geq 3.78$  kHz, additional anomaly could be clearly seen. This peak evolves stronger and shifts to higher temperature with frequency. The peaks in imaginary part of the dielectric constant shifting with frequency indicate relaxation process [15] and are also reported in the single crystal studies of  $RMnO_3$  [2]. The temperature dependence of relaxation process associated with the additional peak was studied by fitting the  $\epsilon''(T)$  curve to the Debye model [16] given by

$$\epsilon''(\omega, T) = \frac{\frac{1}{2}\Delta\epsilon}{\cosh\left[\frac{U}{k_B}\left(\frac{1}{T_M} - \frac{1}{T}\right)\right]} \quad 4.1$$

Where  $\Delta\epsilon$  is the dielectric strength,  $U$  is the activation energy associated with dielectric relaxation process,  $k_B$  is the Boltzmann constant and  $T_M$  is the temperature corresponding to a maximum value of  $\epsilon''(T)$ . The fitting of the curves are shown in Fig.4.3. It is observed that the fitting is better for high frequency than at lower frequency due to strong overlap of the anomalies. The data shown in Fig.4.3 were fitted to Eq 4.1 and  $T_M$  at different frequency was

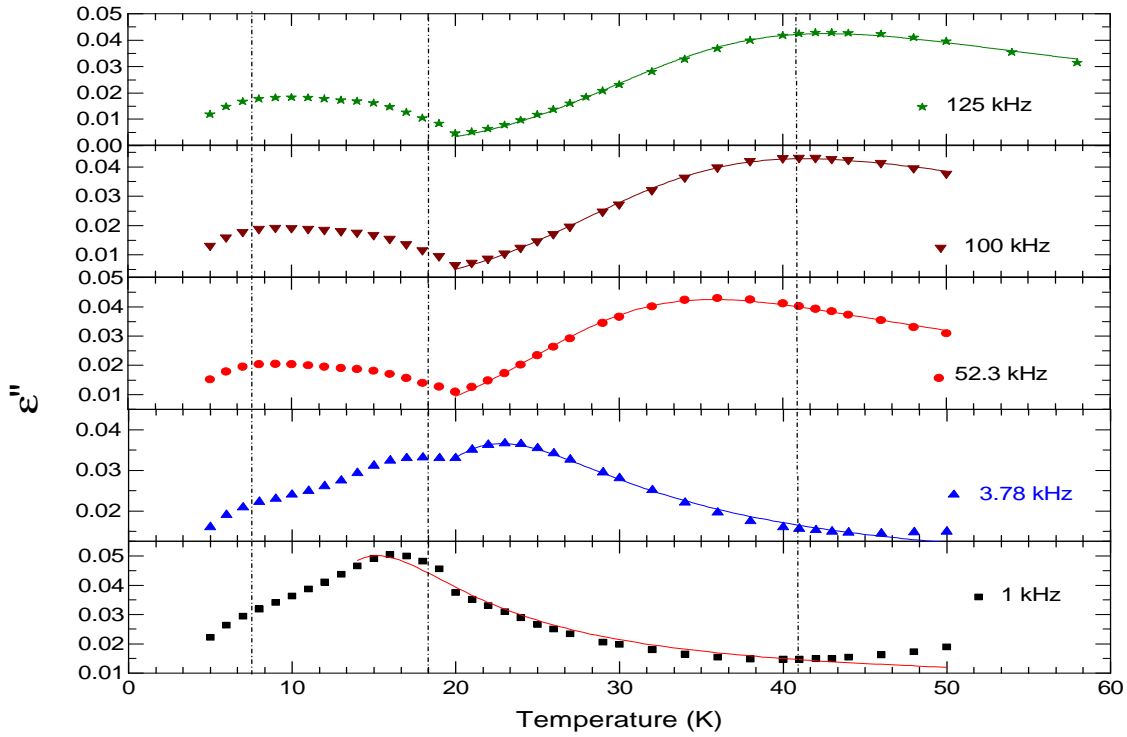


Figure.4.3: Variation of  $\epsilon''$  with temperature at different frequencies. Curve fitting to estimate additional anomaly in  $\epsilon''(T)$  of  $\text{Gd}_{0.7}\text{Y}_{0.3}\text{MnO}_3$  carried out with Debye model.

estimated. Relaxation time was taken as the inverse of corresponding frequency. Variation of relaxation time as function of temperature was estimated by plotting the  $\ln(\tau)$  vs.  $1/T$  to see how it is related to the Arrhenius regime. The plot along with the corresponding fits for all the compositions is shown in Fig.4.4. It is seen that the linearity i.e. Arrhenius law is obeyed in certain temperature regions only. The figures show varying activation energies in different temperature regions depicted by three different slopes. The fitted lines have been extended in Fig 4.4 (b) for clear visibility of three different slopes. The first slope change occurs near the MT1 temperature, i.e. paramagnetic to sinusoidal antiferromagnetic transition of the  $\text{Mn}^{3+}$  sublattice

near about  $\sim 41$  K for all the composition, where a  $\lambda$  like transition was observed in heat capacity measurement discussed in previous chapter.

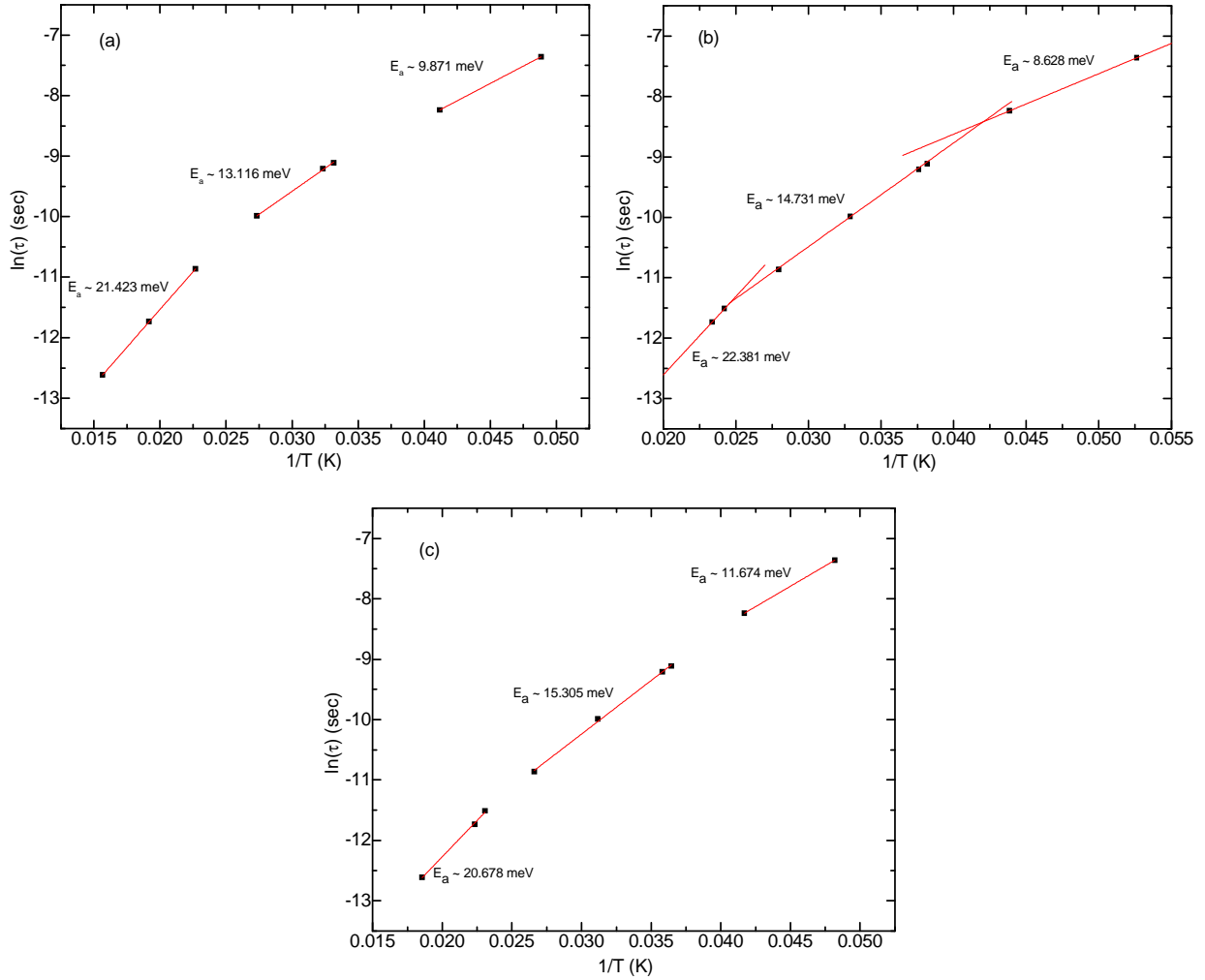


Figure .4.4: Variation of relaxation time  $\ln(\tau)$  vs.  $(1/T)$  for a)  $x=0.2$ , b)  $x=0.3$  and c)  $x=0.4$  fitted to a Debye model. Corresponding activation energies  $E_a$  are indicated.

This indicates that the magnetic ordering changes the dielectric relaxation activation energy. The other change of activation energy is observed in the temperature region of 27 K to 24 K, which may be associated with some transition not detected in specific heat as well as dielectric measurement. The minimum temperature estimated from the fitting of imaginary part of

dielectric permittivity using eq 4.1 was 19K. Hence the second transition that is MT2 could not be traced by linear fitting of the Arrhenius equation. It is clear from the figure that the Arrhenius law is not obeyed in the entire temperature region. More over magnetic transition alter the activation energy of dielectric relaxation mechanism. The activation energies estimated fall in the region of 22 meV to 8 meV for all the composition which are very well associated to dielectric relaxation process. Similar trends and values for activation energy have been quoted for GdMnO<sub>3</sub> [6]. This process described by Debye model follows the Arrhenius law in certain temperature regions and does not describe much about the ferroelectric transition indicated by the strong peak in  $\epsilon'(T)$ , which is an indication of evolution of modulated magnetic structure.

The relaxation process related to ferroelectric phenomena can be best studied by analysing the frequency ( $\omega/2\pi$ ) dependence of dielectric permittivity at different temperatures. The relaxation time can be best determined from the imaginary part of the dielectric permittivity as function of frequency  $\epsilon''(\omega)$  at different temperatures. The loss peaks  $\epsilon''(\omega)$  over five decades of frequency for different temperatures across the ferroelectric transition are plotted in Fig. 4.5. The conductivity contribution is seen as a increase in the value of  $\epsilon''(\omega)$  at lower frequency. The dependence of  $\epsilon''$  on conductivity is given by [15]

$$\epsilon'' = \sigma_0/\epsilon_0\omega \quad (4.2)$$

where  $\sigma_0$  is the dc-conductivity of the sample and  $\epsilon_0$  is the dielectric permittivity of vacuum. With the decrease of temperature, the loss peaks shifts towards lower frequencies with an increase in the strength. The loss peaks are much broader and indicate a distribution of relaxation times. Hence the peaks are best fitted using empirical Cole-Cole function which takes this into

account [15]. The  $\varepsilon''(\omega)$  was fitted to the imaginary part of the Cole-Cole function for estimation of relaxation time.

$$\varepsilon''(\omega) = \frac{\Delta\varepsilon * (\omega\tau_{cc})^\beta * \sin(\beta\pi/2)}{[1 + 2(\omega\tau_{cc})^\beta * \cos(\frac{\beta\pi}{2}) + (\omega\tau_{cc})^{2\beta}]} \quad 4.3$$

where  $\Delta\varepsilon$  is the dielectric strength,  $\tau_{cc}$  is the Cole-Cole relaxation time and  $\beta$  is a width parameter, with  $\beta = 1$  implying the Debye case. Values of  $\beta < 1$  lead to broadening of the loss peaks.

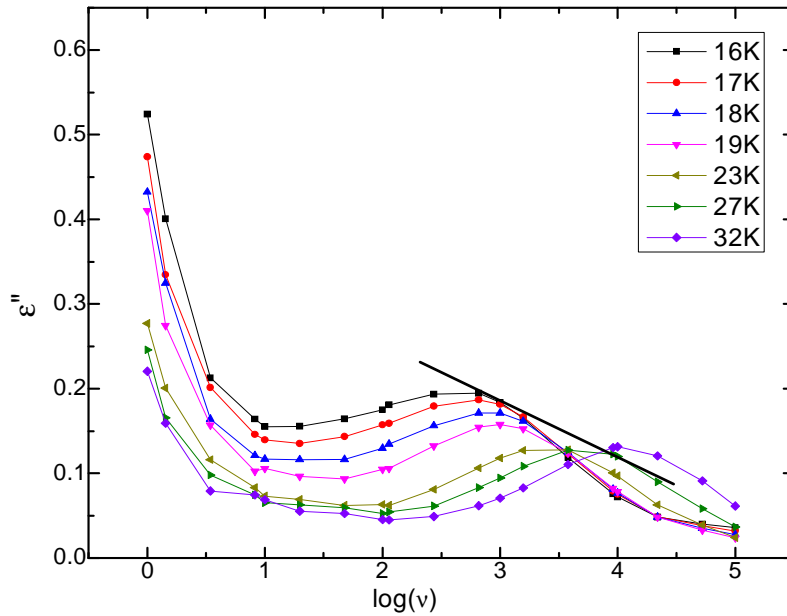


Figure 4.5: Figure showing the variation of  $\varepsilon''(\omega)$  at different temperature for  $Gd_{0.8}Y_{0.2}MnO_3$ .

As the  $\varepsilon''(\omega)$  consists of conductive and relaxation contributions, the curves were fitted with both the conductivity part given by Eq 4.2 and relaxation part given by a Cole-Cole function give by Eq 4.3. The fitting for  $Gd_{0.8}Y_{0.2}MnO_3$  at 23K is shown Fig.4.6.

Variation of the relaxation times as a function of temperature is plotted in an Arrhenius representation and is shown in Fig.4.7 for all the compositions. The curves exhibit non-linear

dependence. This essentially indicates that the process is not a simple thermally activated behaviour, in other words are non-Arrhenius. The positive curvature in the  $\tau$  vs.  $\log(\nu)$  plots imply that the non-Arrhenius could be a tunneling processes at low temperatures [7]. The curves merge at the high temperature region indicating that the relaxation process has same origin in all the compositions.

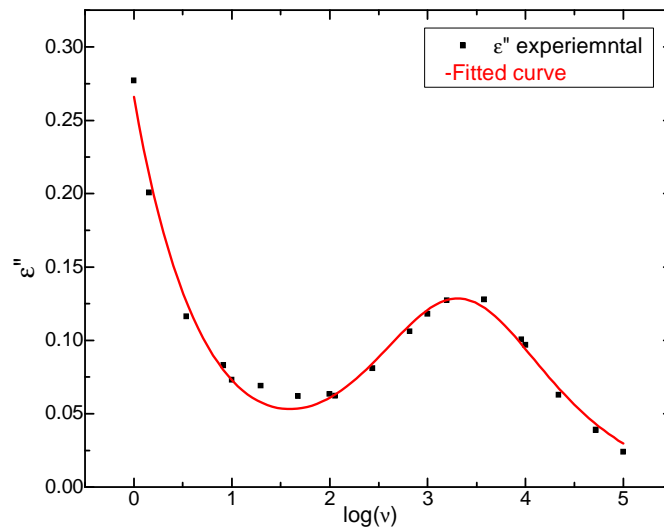


Fig.4.6: Figure showing the fitting  $\epsilon''(\omega)$  with both conductive and Cole-Cole function for  $x=0.2$  at 23K.

The plots show a peak like structure emerging for  $x=0.3$  and  $0.4$  visible by slight change in slope in the temperature region of 19 to 15K. This indicates that the relaxation process slows down near the ferroelectric transition and then again assumes its usual earlier behaviour. This also matches with the  $\text{Eu}_{0.8}\text{Y}_{0.2}\text{MnO}_3$  curve reported in [7], but they are not as clearly visible as reported by F. Schrettle *et.al.*, where the measurements were done on  $c$ -axis oriented single crystal, while the samples studied here are polycrystalline in nature.

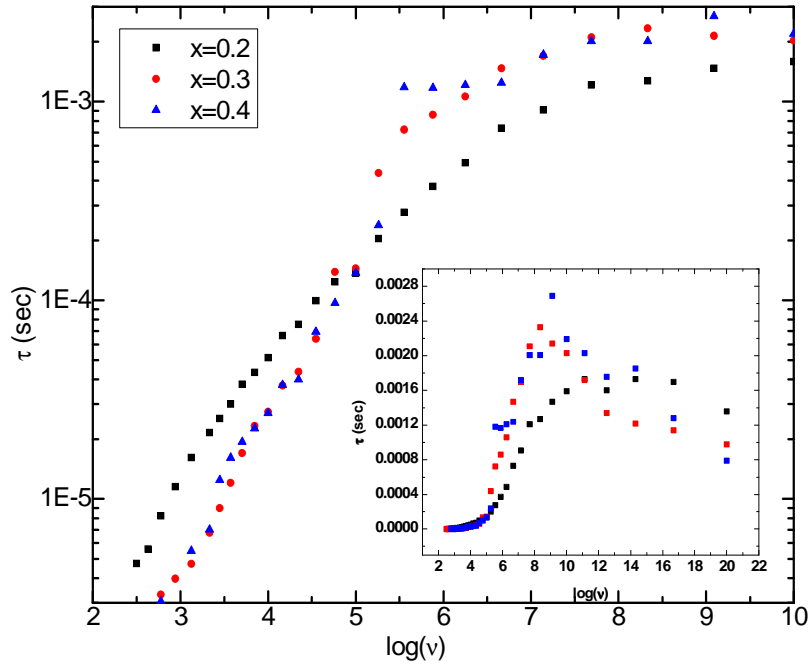


Figure.4.7: Arrhenius representation of relaxation time variation as a function of temperature for  $Gd_{1-x}Y_xMnO_3$  for  $x=0.2, 0.3$  and  $0.4$ .

The dielectric measurements were done at a temperature interval of 1K as a result the peaks observed were not as well defined as seen in [7] and could not be observed for the  $x=0.2$  composition. The variations of the dielectric strength  $\Delta\epsilon$ , with temperature are plotted in Fig. 4.8. The dielectric strength is seen to increase near the ferroelectric transition temperature and it shows a peak well above the transition temperature in all the compositions.

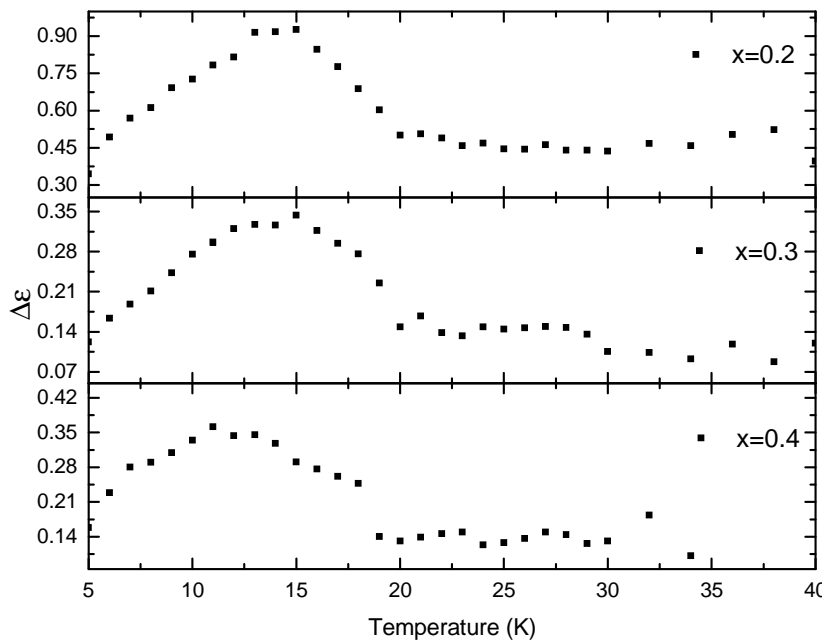


Figure.4.8: Variation of dielectric strength for  $Gd_{1-x}Y_xMnO_3$  ( $x = 0.2, 0.3$  &  $0.4$ ).

### 4.3. Low Temperature XRD Studies

Low temperature XRD studies were undertaken on  $Gd_{1-x}Y_xMnO_3$  ( $x=0, 0.2$  &  $0.3$ ) system to study the variation of lattice parameters with temperature and to elucidate the existence of magnetoelastic coupling in the system. Powder X-ray diffraction (XRD) studies were carried out at Indus II synchrotron beam line in the temperature interval of 10 to 110 K. In  $TbMnO_3$ , the ferroelectricity appears to originate from a long-period incommensurate AFM spiral or ellipsoidal structure that cause the underlying lattice to modulate with a period twice that of magnetic through magnetoelastic coupling. As few studies are devoted to low temperature structural studies of  $GdMnO_3$ , parent compound is also included in the present study. As a representative, low temperature XRD patterns for  $x=0.3$  compound at select temperatures are shown in Fig.4.9.

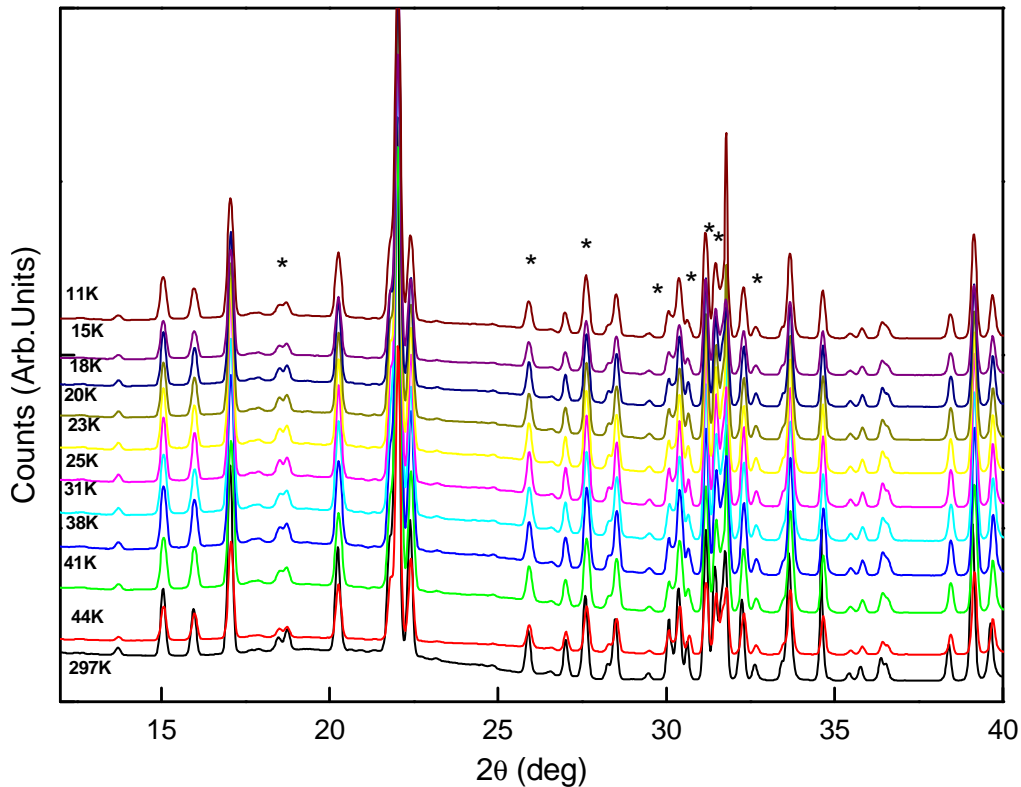


Figure.4.9: Low temperature XRD pattern at different temperature for  $Gd_{0.7}Y_{0.3}MnO_3$  recorded at Indus-2. The Be peaks are star marked

The peaks marked with ‘\*’ are the Bragg reflections from the beryllium foils/discs located at the sample holder and at vacuum shields of the cryostat. Due to the difficulties, as elaborated in Chapter 2, in taking into account of Be peaks during the Rietveld refinement analysis, lattice parameters were alone estimated from the powder XRD patterns. Due to the lower signal to noise ratio and background the XRD pattern of the  $x=0.4$  sample were not analysed.

The temperature dependence of the lattice parameters of the parent compound  $GdMnO_3$  is shown in Fig.4.10. In the temperature interval of 60 to 110 K, a positive thermal coefficient for all the lattice parameters is clearly seen. Anomalous changes in the lattice parameters are

observed at about 44 K, corresponding to para to incommensurate sinusoidal AFM magnetic transition of  $\text{Mn}^{3+}$  sublattice of  $\text{GdMnO}_3$ .

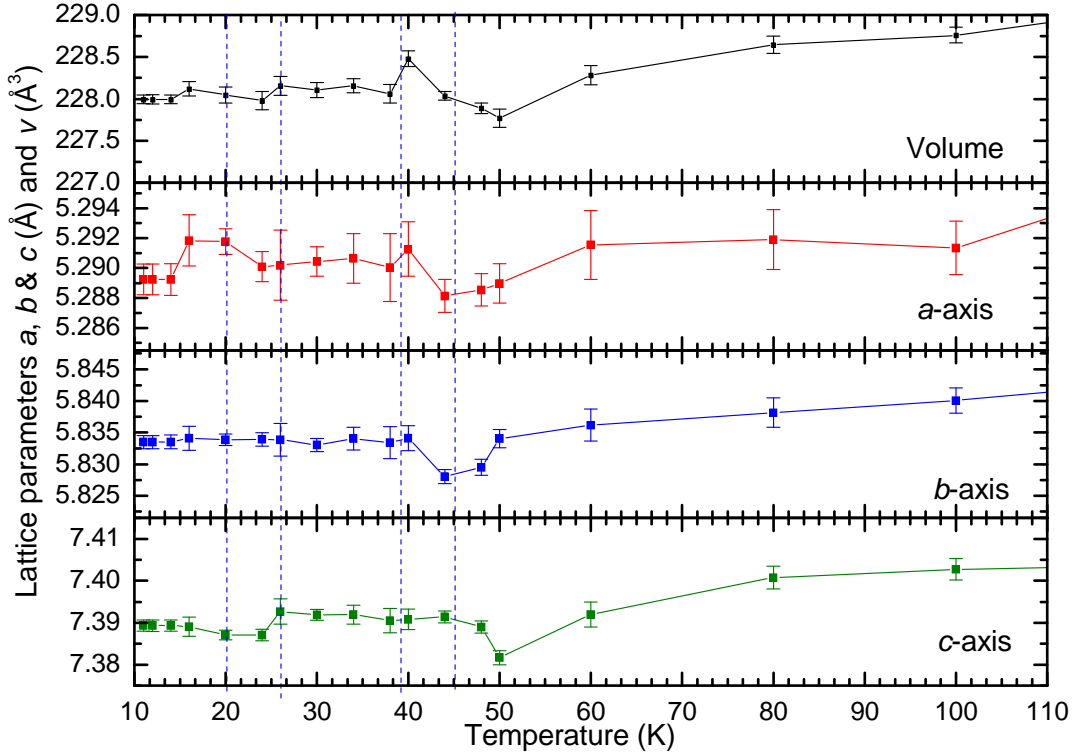


Figure.4.10: Lattice parameter variation of  $\text{GdMnO}_3$  as a function of temperature.

This results in unambiguous increase in the volume of the unit cell across this temperature. At about 23 K  $a$ - and  $c$ - axis alone exhibit measurable changes; while  $a$ -axis increases,  $c$ -axis is seen to decrease by similar magnitude leading to marginal decrease in the unit cell volume. This temperature region is associated to a sinusoidal antiferromagnetic to A-type antiferromagnetic transition of the Mn sublattice [12]. These changes across the magnetic transitions clearly demonstrate presence of magnetoelastic coupling in  $\text{GdMnO}_3$ . Observed changes in the lattice parameters across the MT2 transition are in general agreement with a report on thermal expansion studies on crystals of  $\text{GdMnO}_3$ .

Temperature dependence of lattice parameters of  $\text{Gd}_{0.8}\text{Y}_{0.2}\text{MnO}_3$  in the temperature interval of 10 to 110 K are shown in Fig. 4.11.

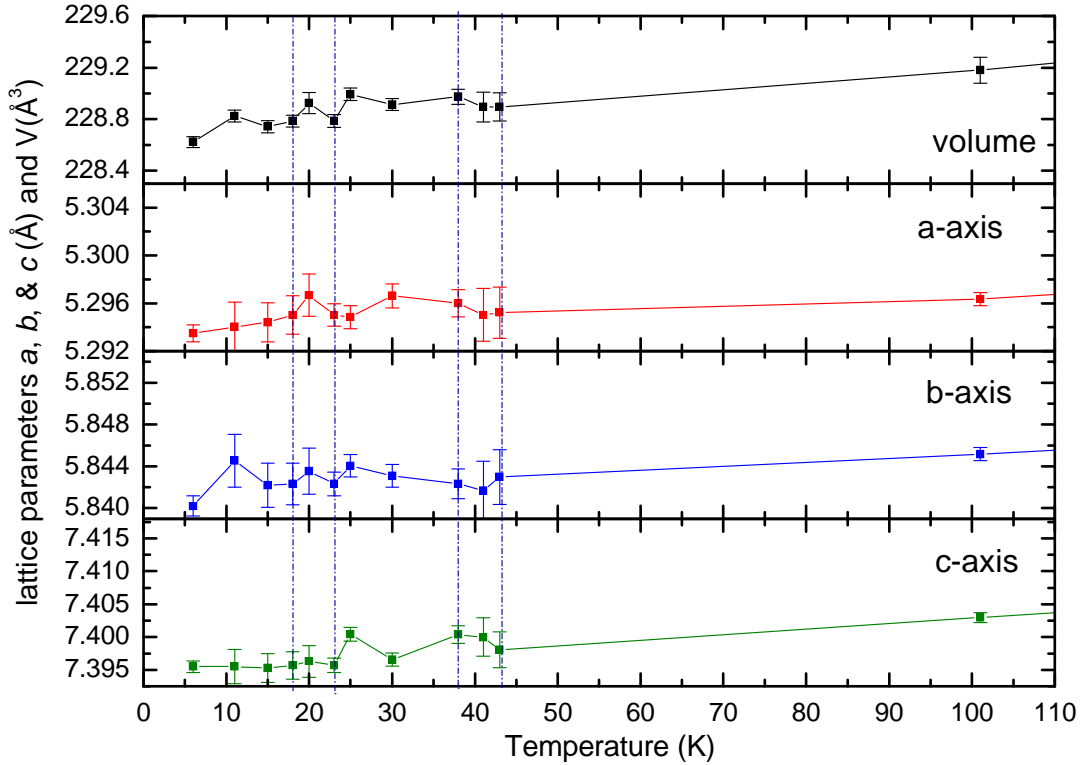


Figure.4.11: Lattice parameter variation of  $\text{Gd}_{0.8}\text{Y}_{0.2}\text{MnO}_3$  as a function of temperature.

An overall positive coefficient for thermal expansion of the lattice parameters are observed down to 50 K. Minute anomalies in the temperature variation of lattice parameters  $a$  and  $c$  are observed about 41 K; whilst lattice parameters  $a$  and  $c$  increase, a dip is observed for the lattice parameter  $b$ . This temperature coincides with that of  $\lambda$ -anomaly seen in specific heat studies (Fig.4.13) and is associated with the paramagnetic to sinusoidal AFM transition of  $\text{Mn}^{3+}$ -sublattice. These variations are small compared to corresponding anomalies observed in  $\text{GdMnO}_3$ . Other than this, no perceptible anomalies in any of the lattice parameter is observed, specifically about a temperature ( $\sim 18\text{K}$ ) wherein peak in  $\epsilon'(T)$  and  $\epsilon''(T)$  is observed.

Variations of the lattice parameters  $a$ ,  $b$ ,  $c$ , and unit cell volume  $v$  in the temperature interval 0 to 110 K for  $\text{Gd}_{0.7}\text{Y}_{0.3}\text{MnO}_3$  is shown Fig.4.12.

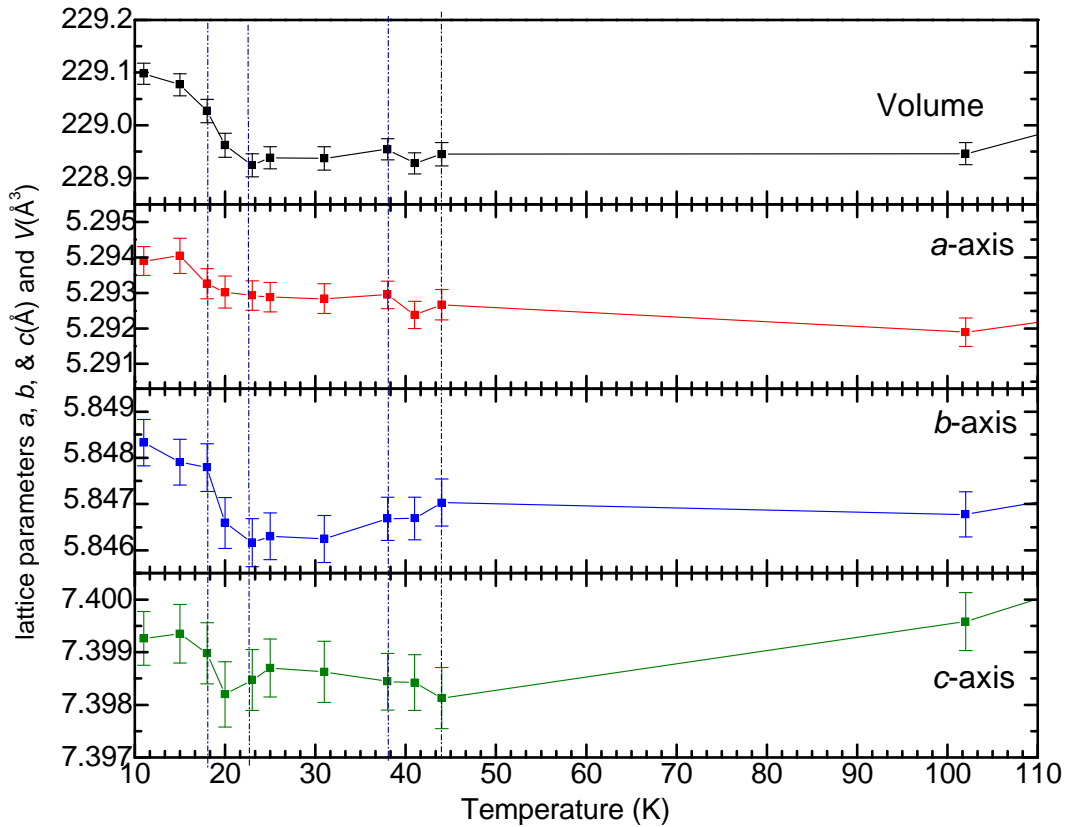


Figure.4.12: Lattice parameter variations of  $\text{Gd}_{0.7}\text{Y}_{0.3}\text{MnO}_3$  as a function of temperature

The lattice parameters exhibit anomalous variations in their temperature dependence about the magnetic transitions MT1 and MT2. It is seen that the  $a$ -axis exhibits negative thermal expansion with a dip about 41 K and a step increase about 20 K. Though  $b$ -axis also registers a step increase about 20 K, exhibits positive thermal expansion between the magnetic transition MT1 and MT2 temperature. On the other hand, the  $c$ -axis in the temperature range of MT1 and MT2 is almost temperature independent. In the temperature range of 23K to 18K the  $c$ -axis first decreases followed by a step increase below 20K undergoing an expansion all the way to low temperature. All the lattice parameters in general increase below 20K. In general, the anomaly

exhibited by the lattice parameter  $a$  is smaller compared to those by  $b$  and  $c$ . A steep increase in the lattice parameters  $a$ ,  $b$ , and  $c$  at about 17 K are estimated to be  $1.03 \times 10^{-3}$ ,  $1.32 \times 10^{-3}$ , and  $1.15 \times 10^{-3}$  Å respectively.

Notwithstanding the thermal expansion and the anomalies, the relation,  $c/\sqrt{2} < a < b$  corresponding to O' distortion of  $Gd_{1-x}Y_xMnO_3$  ( $x=0, 0.2$  and  $0.3$ ) is obeyed throughout the temperature range of measurement. Corresponding to para to sinusoidal AFM transition of  $Mn^{3+}$ -sublattice, changes in the lattice parameters are observed for all the value of  $x$ . Mixed variation, increase and decrease along different axes are observed. Associated to the ferroelectric transition (MT2), no anomaly is detected in the lattice parameter variation with temperature for  $x = 0.2$ . However, increase in all the lattice parameters is observed for  $x = 0.3$  about MT2 resulting in substantial increase in the volume. This is to be compared against mixed variations reported for lattice parameters of  $Eu_{1-x}Y_xMnO_3$  [8] and  $Lu_{1-x}Y_xMnO_3$  [17]. In general, low temperature structural studies imply existence of magnetoelastic coupling for the compounds under investigation.

#### 4.4. Normal and Inverse Magneto Caloric Effect

The results on the specific heat measurements on  $Gd_{1-x}Y_xMnO_3$  ( $x=0.2, 0.3$  and  $0.4$ ) were discussed in Chapter 3, limiting to identification of the magnetic transitions in the system. The paramagnetic to antiferromagnetic transition of  $Mn^{3+}$ - ( $\sim 41$  K) and  $Gd^{3+}$ - ( $\sim 7$  K) sublattice could be clearly identified but the metamagnetic transition of the  $Mn^{3+}$  sublattice ( $\sim 18$  K) could not be seen clearly. Magneto-thermal phenomena, vis-à-vis magnetocaloric effect (MCE) have a strong influence on physical properties like entropy, heat capacity and thermal conductivity, and reflects transformations taking place in spin structure of a magnetic material. Thus studying MCE in

multiferroic materials is of great interest as these consists of several magnetic and meta magnetic transition related to spin reorientation. MCE a ubiquitous phenomenon exhibited by all materials in general and is further enhanced in 3d-4f systems. Thus  $\text{RMnO}_3$  system offers great opportunity for such studies. The interest in investigation of MCE on the one hand is due to the possibility of obtaining information about the magnetic state and magnetic phase transformations in magnetic materials that is hard to obtain by other methods and, on the other hand, because of the prospects of the creation of magnetic cooling machines using magnetic materials as working bodies. In the presence of coupling between the ferroic degrees of freedom, the magnetocaloric effect in multiferroic is expected to be enhanced compared to the rest. The MCE can be quantified by either intensive parameter like adiabatic temperature change  $\Delta T_{\text{ada}}$  or extensive thermodynamic parameter like isothermal entropy change  $\Delta S$ . In most of the report in literature,  $\Delta S$  alone is shown, for the sake of comparison both these parameters  $\Delta S$  and  $\Delta T_{\text{ada}}$  have been estimated for the present system. These parameters were obtained from the specific heat studies both in presence and absence of external magnetic field. The details of their estimation will subsequently be presented.

The reduction in  $C_p/T$  at the Gd transition temperature with reducing Gd concentration was discussed in detail in section 3.4. The higher value of specific heat at  $\text{Gd}^{3+}$  transition is owing to its higher magnetic moment compared to that of Mn [18]. The  $C_p/T$  vs. T plot for all x at different magnetic fields is shown in Fig.4.13. From the figure it is seen that the  $C_p/T$  vs. T plot essentially is unaltered for  $H = 0.5$  T. For higher fields, significant changes are observed in  $C_p/T$  value about  $\text{Gd}^{3+}$ -sublattice ordering temperature (MT3) while diminutive changes are observed corresponding to that of  $\text{Mn}^{3+}$ -sublattice (MT1). In accordance with the antiferromagnetic transition nature, no detectable change is observed about MT1. On the other

hand the peak corresponding MT3 shifts to higher temperatures. Further, this peak broadens and asymmetrically stretches to higher temperature in the presence of field. This stretching results in a nominal increase in the value of  $C_p$  at about MT1. For certain  $\text{RMnO}_3$  systems, rare-earth sublattice is reported to undergo below their antiferromagnetic transition, a magnetic field induced AFM to FM transition above certain critical field [19]. In view of this report and based on the observed shift the anomaly associated with  $\text{Gd}^{3+}$ -sublattice to higher temperatures on application of magnetic field, a magnetic field induced AFM to FM of the  $\text{Gd}^{3+}$ -sublattice above  $H > 0.5$  T is inferred in  $\text{Gd}_{1-x}\text{Y}_x\text{MnO}_3$  system. Thus this could possibly be the first report of field induced AFM-FM transition of  $\text{Gd}^{3+}$  in orthorhombic  $\text{RMnO}_3$  systems.

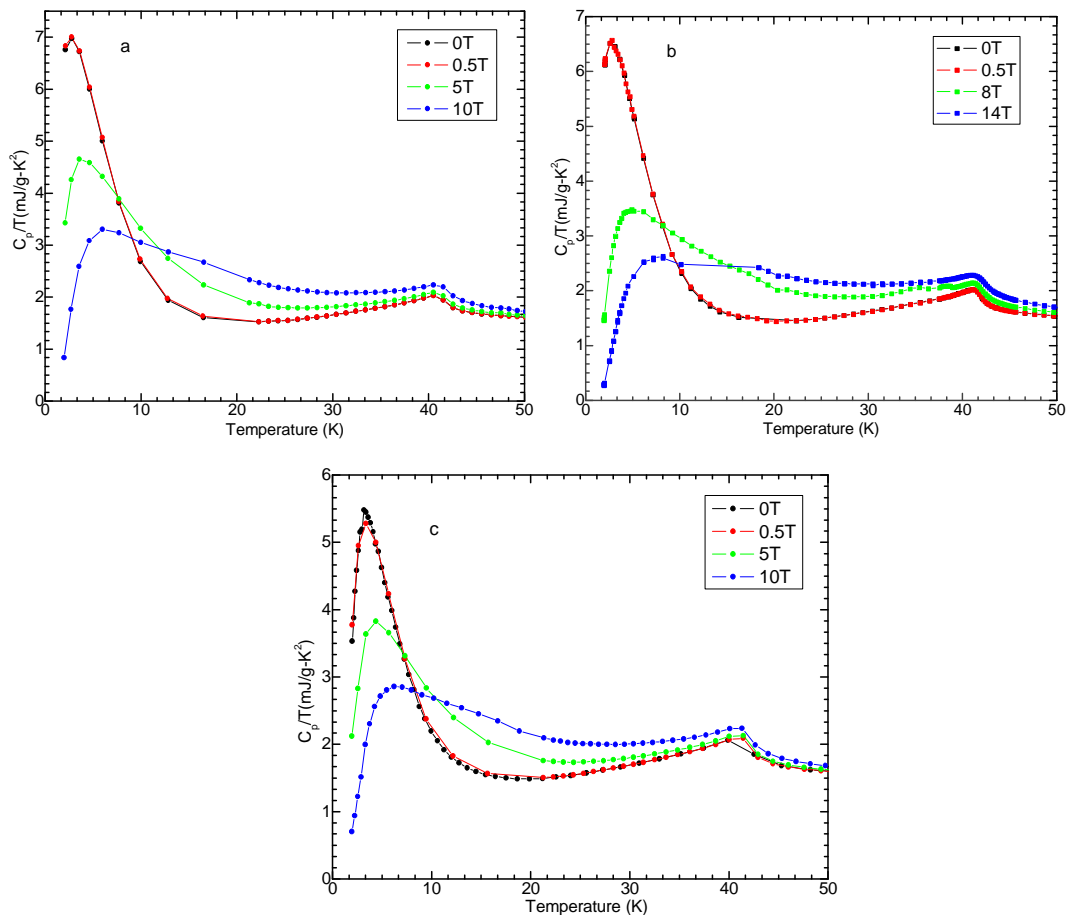


Figure.4.13:  $C_p/T$  vs.  $T$  plot for  $\text{Gd}_{1-x}\text{Y}_x\text{MnO}_3$  a)  $x=0.2$ , b)  $x=0.3$  and c)  $x=0.4$ .

Hence, for  $H=0.5T$ , the AFM ground state of  $Gd^{3+}$ -sublattice is preserved and no change in the specific heat about  $MT_3$  is observed. Broadening and stretching is direct consequence of smearing of the Brillouin function under the influence of external magnetic field and is a generic of the ferromagnetic state.

The isothermal entropy change can be found indirectly either from isothermal magnetisation curve or from heat capacity curves obtained at different magnetic field. The change in entropy is found from the heat capacity curves using the formula

$$\Delta S(H, T) = \int_0^T \frac{C_P(H) - C_P(0)}{T} dT$$

It is to be pointed out that, the specific heat were measured at 0, 0.5, 5 and 10T for  $x=0.2$  and 0.4, while for  $x=0.3$  system they were measured at 0, 0.5, 8 and 14T. The variation of adiabatic temperature change  $\Delta T_{ada}$  and isothermal entropy change  $\Delta S$  at different applied magnetic field as a function of temperature for all the composition is shown in Fig.4.14. For all the compositions and for  $H=0.5 T$ , the value of  $\Delta T_{ada}$  ( $\Delta S$ ) is negative (positive). The reasons for observation of inverse MCE is that under a field of 0.5 T, ground state of both the sublattice are still antiferromagnetic. In contrast to ferromagnets which cool upon demagnetization, antiferromagnets cools upon adiabatic magnetization *i.e.*, positive  $\Delta S$  or inverse MCE (IMCE). Thus for a ferromagnetic transition associated  $\Delta S$  is  $-ve$  and  $\Delta T$  is  $+ve$  while for an anti ferromagnetic transition signs are reversed, *i.e.*  $\Delta S$  is  $+ve$  and  $\Delta T$  is  $-ve$  [18]. At higher fields, both  $\Delta T_{ada}$  and  $\Delta S$  reverse their signs and assumes much higher value from that for  $H=0.5 T$  for  $T < MT_1$ . Reversals of signs imply the ground state of  $Gd^{3+}$ -sublattice is changed to ferromagnetic. Such a reversal of isothermal entropy change is also reported for  $TbMnO_3$  crystal

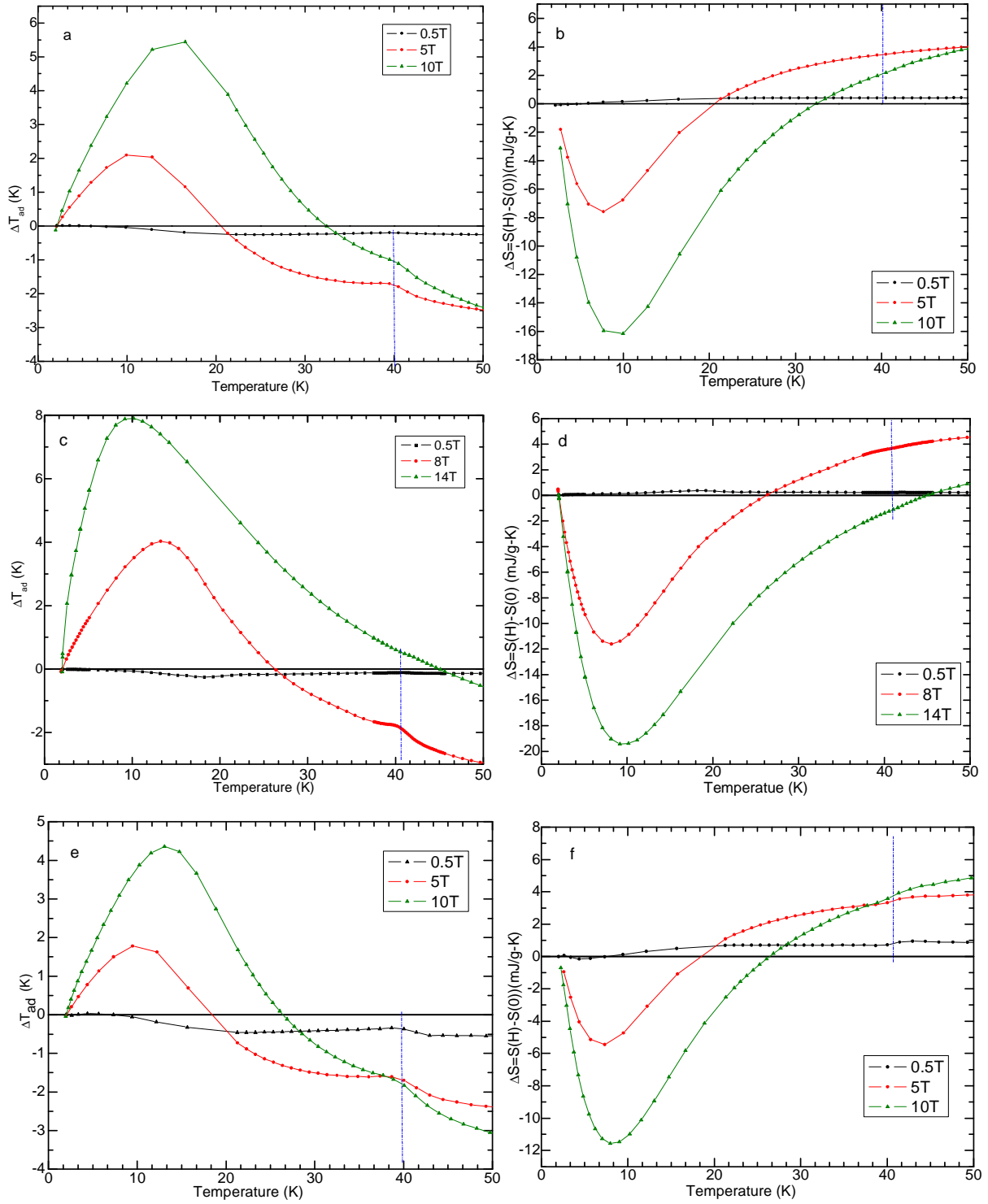


Figure.4.14: Figure showing the variation of  $\Delta T_{ad}$  and  $\Delta S$  for  $Gd_{1-x}Y_xMnO_3$  (a, b)  $x=0.2$ , (c, d)  $x=0.3$  and (e, f)  $x=0.4$  respectively.

[20] along the  $a$  and  $b$ -axis. In addition to this, a weak and distinctive anomaly about MT1 ( $\sim 41$  K) rides over major peak in  $\Delta T_{\text{ada}}$  whose sign is not reversed with field. Unlike that of  $\text{Gd}^{3+}$ -sublattice, the magnetic state associated with MT1 is unaffected by field. These observations are in line with the similar inferences drawn from the  $C_p/T$  studies in the presence of magnetic field [19]. It is seen that the temperature corresponding to maximum in  $\Delta T_{\text{ada}}$  doesn't coincide with that corresponding to minimum in  $\Delta S$ . This is in accordance with the report of Pecharsky *et. al.* [21] who have showed that in general the maximum (or minimum)  $\Delta T_{\text{ada}}$  (T) should not coincide with the temperature of the corresponding minimum (or maximum) in  $\Delta S(T)$ . This apart, for higher field both  $\Delta T_{\text{ada}}$  and  $\Delta S$  change their sign beyond a particular field. The cause for such a change has to be probed and understood.

The maximum value of  $\Delta T_{\text{ada}}$  is found to be  $\sim 5.4$  K and 4.3 K for  $x = 0.2$  and 0.4 respectively for  $H = 10\text{T}$  and  $\sim 4$  K for  $x = 0.3$  at 8T. It is observed that the value of  $\Delta T$  decreases with decreasing Gd concentration. Though the value of  $\Delta T_{\text{ada}}$  is considerably large they are less compared to archetypical Gd based MCE materials like  $\text{Gd}_5\text{Se}_2\text{Ge}_2$  [22]. The maximum value for  $\Delta S$  is found to be -16.102 mJ/gm-K and -11.562mJ/gm-K for  $x=0.2$  and 0.4 at 10T and -11.634mJ/gm-K for  $x=0.3$  at 8T. In general, the value of  $\Delta S$  decreases with decrease of Gd concentration. The  $\Delta S$  changes sign and become positive above 20K for all the composition. The sign reversal temperature increases with increasing magnetic field. Apart from the magnitude of  $\Delta T_{\text{ada}}$  and  $\Delta S$  the width of the peak is also important for refrigerant capacity (RC). In comparison to  $\text{TbMnO}_3$  the FWHM of  $\Delta S$  for  $\text{Gd}_{1-x}\text{Y}_x\text{MnO}_3$  system is smaller. This indicates that the RC of current system is smaller in comparison to  $\text{TbMnO}_3$  [10].

## 4.5. Conclusions

The dielectric studies clearly show a peak like feature both in the real and imaginary part of temperature dependent dielectric permittivity around  $\sim 18\text{K}$  for all the composition. As the system studied is polycrystalline, the peak is slightly broad which could be the combined effect of peaks observed along a-axis and c-axis [2]. Thus it is a clear evidence of ferroelectric transition present in the system. This peak slightly shifts with variation of composition. Apart from this another anomaly is observed near about  $7\text{-}8\text{K}$  which is associated with the magnetic ordering of the  $\text{Gd}^{3+}$  sublattice and this has been reported in literature [2]. No evidence whatsoever of the magnetic transition at MT1 of  $\text{Mn}^{3+}$  sublattice from paramagnetic to sinusoidal anti ferromagnetic could be found in the dielectric curves. The study of relaxation process by analyzing the imaginary part of the dielectric permittivity  $\epsilon''(\text{T})$  as a function of temperature at different frequencies shows that the Arrhenius law is obeyed only in certain temperature regions thus indicating that in the entire temperature region the dielectric mechanism may not be a simple thermally activated process. The first change in activation energy is observed near MT1 around  $\sim 41\text{K}$  for all the composition. Another change in activation energy is observed near  $27\text{K-}24\text{K}$  whose process is not understood at present and further investigations is required. As the variation of activation energy across MT2 could not be studied by this, the variation of  $\epsilon''$  was analysed as a function of frequency at different temperature by fitting it with Cole-Cole function and also taking into account the conductivity part at lower frequency over five decades of frequency range. It is clear from this study that system does not follow the Arrhenius law and variation of the relaxation time shows a bending which shows a tunneling process [7]. More over for  $x = 0.3$  and  $0.4$  change in relaxation time (slowdown) around MT2 is observed which is

associated to ferroelectric transition and is similar in nature though not as evident as seen for  $\text{Eu}_{0.8}\text{Y}_{0.2}\text{MnO}_3$  *c*-axis oriented single crystal curve in the work of F. Schrettle *et.al* [6]. The variation of lattice parameter around MT1 and MT2 shows the magneto-elastic behaviour about the magnetic transition. The lattice parameters show anomalous changes and it is observed for  $\text{Gd}_{1-x}\text{Y}_x\text{MnO}_3$  for  $x = 0, 0.2$  and  $0.3$ . Similar variation has been reported for  $\text{Eu}_{1-x}\text{Y}_x\text{MnO}_3$  [8] and  $\text{Lu}_{1-x}\text{Y}_x\text{MnO}_3$  [17].

The system shows enhanced MCE as is expected for multiferroic materials. Both  $\Delta S$  and  $\Delta T_{\text{ada}}$  show interesting features with temperature and magnetic field. The system shows reversal of sign of both  $\Delta S$  and  $\Delta T_{\text{ada}}$  with applied magnetic field. As the magnetic field is increased beyond 0.5T the signs change this is associated with antiferromagnetic to ferromagnetic transition of  $\text{Gd}^{3+}$  sublattice. This has been reported for other  $\text{RMnO}_3$  systems like  $\text{TbMnO}_3$  [10,19]. This is a first report of magnetic field induced transition in  $\text{GdMnO}_3$  series. As the magnetic moment of Gd is higher than Mn most of the features of MCE is dominated by Gd. With magnetic field there is also a slight shift and broadening of the peaks near Gd transition temperature. As the temperature is further raised  $\Delta S$  again changes sign from negative to positive. The reason for this is not understood but it could be due to destruction of ferromagnetic ordering of  $\text{Gd}^{3+}$  sublattice with temperature while the  $\text{Mn}^{3+}$  still remains antiferromagnetic. This is just a supposition while the real reason needs to be further investigated. The value of both  $\Delta S$  and  $\Delta T$  decrease with decreasing Gd concentration. Thus  $\text{Gd}_{1-x}\text{Y}_x\text{MnO}_3$  shows both normal and Inverse MCE with magnetic field and temperature. Such materials have immense use for various applications such as in hydrogen liquefaction and space applications.

## References:

- [1]. T. Kimura, T. Goto, H. Shintani, K. Ishizaka, T. Arima, and Y. Tokura, *Nature* **426**, 55 (2003).
- [2]. T. Goto, T. Kimura, G. Lawes, A. P. Ramirez, and Y. Tokura, *Phys. Rev. Lett.* **92**, 257201 (2004).
- [3]. T. Goto, Y. Yamasaki, H. Watanabe, T. Kimura, and Y. Tokura, *Phys. Rev. B* **72**, 220403(R) (2005).
- [4]. V. Yu. Ivanov, A. A. Mukhin, V. D. Travkin, A. S. Prokhorov, Yu. F. Popov, A. M. Kadomtseva, G. P. Vorob'ev, K. I. Kamilov, and A. M. Balbashov, *phys. stat. sol. (b)* **243**, No. 1, 107–111 (2006).
- [5]. Mathias Doerr, Michael Luewenhaupt, Aditya A. Wagh, P. S. Anilkumar, Suja Eilzabeth, Sahana Roessler, Martin Rotter, Steffen Wirth, *J. Korean. Phys. Society* **62** 10 (2013)
- [6]. W. S. Ferreira, J. Agostinho Moreira, A. Almeida, M. R. Chaves, J. P. Araújo, J. B. Oliveira, J. M. Machado Da Silva, M. A. Sá, T. M. Mendonça, and P. Simeão Carvalho, *Phys. Rev. B* **79**, 054303 (2009).
- [7]. F. Schrettle, P. Lunkenheimer, J. Hemberger, V. Yu. Ivanov, A. A. Mukhin, A. M. Balbashov, and A. Loidl, *Phys. Rev. Lett.* **102**, 207208 (2009).
- [8]. J. Agostinho Moreira, A. Almeida, W. S. Ferreira, J. P. Araújo, A. M. Pereira, M. R. Chaves, M. M. R. Costa V. A. Khomchenko, J. Kreisel, D. Chernyshov, S. M. F. Vilela and P. B. Tavares, *Strong magnetoelastic coupling in orthorhombic  $\text{Eu}_{1-x}\text{Y}_x\text{MnO}_3$  manganite*, *Phys. Rev. B* **82**, 094418 (2010).
- [9]. Melvin M Vopson, *J. Phys. D: Appl. Phys.* **46** (2013) 345304
- [10]. Jin-Ling Jin, Xiang-Qun Zhang, Guo-Ke Li, and Zhao-Hua Cheng, *Phys. Rev. B* **83**, 184431 (2009).
- [11]. X. Moya, S. Kar-Narayan and N. D. Mathur, *Nmat* **13**, 439 (2014).
- [12]. T. Kimura, G. Lawes, T. Goto, Y. Tokura and A. P. Ramirez, *Phys. Rev. B* **71**, 224425 (2005).
- [13]. I.A. Troyanchuk, N.V. Kaspar, H. Szymczak, and A. Nabialek, *Low Temp. Phys.* **23**, 300 (1997).
- [14]. J. Hemberger, S. Lobina, H.-A. Krug von Nidda, N. Tristan, V. Yu. Ivanov, A. A. Mukhin, A. M. Balbashov, and A. Loidl, *Phys. Rev. B* **70**, 024414 (2004).

- [15]. F.Kremer and A. Schonhals, *Broadband dielectric spectroscopy*, Springer-Verlag Berlin Heidelberg GmbH (2003).
- [16]. C J F Bottcher and P Bordewijk , *Theory of electric polarization, Vol II*, Elsevier Scientific Publishing Company 1977.
- [17]. Seongsu Lee, A. Pirogov, Misun Kang, Kwang-Hyun Jang, M. Yonemura, T. Kamiyama, S.-W. Cheong, F. Gozzo, Namsoo Shin, H. Kimura, Y. Noda & J.-G. Park, *Nature* **451**, 805 (2008).
- [18]. A M Tishin and Y I Spichkin, *The magnetocaloric effect and its applications*, Institute of Physics Publishing Bristol and Philadelphia (2003)
- [19]. A. Midya, S. N. Das, P. Mandal, S. Pandya and V. Ganesan, *Phys. Rev. B* **84**, 235127 (2011).
- [20]. Jin-Ling Jin, Xiang-Qun Zhang, Guo-Ke Li, Zhao-Hua Cheng, Lin Zheng and Yi Lu, , *Phys. Rev. B* **83**, 184431 (2011).
- [21]. V. K. Pecharsky, K. A. Gschneidner, Jr. A. O. Pecharsky and A. M. Tishin, *Phys. Rev. B* **64**, 14006 (2001).
- [22]. V. K. Pecharsky, K. A. Gschneidner, Jr , *Phys. Rev. Lett.* **78**, 4494 (1997).

## CHAPTER 5

### Raman studies and band structure calculation on $\text{Gd}_{1-x}\text{Y}_x\text{MnO}_3$

#### 5.1. Introduction

The average ionic radius of rare earth of  $\text{RMnO}_3$  subtly modifies the ground state of magnetic structure. With favourable structural parameters, especially the Mn-O-Mn bond angle a few of  $\text{RMnO}_3$  compounds ( $\text{R}=\text{Tb}, \text{Dy}$ ) are multiferroic. Decreasing ionic radius increases the orthorhombic distortion, which in turn varies the relative strength of competing ferro ( $J<0$ ) and antiferromagnetic ( $J>0$ ) superexchange interaction among the  $\text{Mn}^{3+}$  ions. Resultant magnetic frustration leads to varieties ground state for the magnetic structures, a few of which give rise to spontaneous polarization as well. It is probable that these lattice, magnetic modulation and distortions have some effect on the phonon parameters near the magnetic transitions. Strong coupling between phonons and electrons has been shown to play important role in colossal magnetoresistance in  $\text{La}_{1-x}\text{M}_x\text{MnO}_3$  ( $\text{M}=\text{Sr}, \text{Ca}$ ) system [1,2]. Among these, phonon modes associated with the Jahn-Teller (JT) distortion in particular is known to affect both the magnetic and transport properties and has been studied using optical phonons [1,3]. As the JT distortion is coupled to the magnetic structure, it is expected to affect those corresponding phonon modes are modified across the magnetic transition. This coupling between spin and phonon, known as dynamic spin-phonon coupling is quite ubiquitous in ortho-manganites and specifically in multiferroic materials [4]. This results in renormalization of phonon frequencies with the onset of long range magnetic ordering. Such spin-phonon coupling effects have been studied in  $\text{RMnO}_3$  [5] system and mixed crystal systems like  $\text{Eu}_{1-x}\text{R}_x\text{MnO}_3$  ( $\text{R}=\text{Y}, \text{Lu}$ ) [6]. These studies indicate anomalous softening that of certain Raman active modes especially the stretching modes

associated with dynamic Jahn-Teller distortions across the magnetic ordering. The anomalous softening of these modes is reasoned to arise from phonon modulation of the superexchange integral,  $J$  [7].

As had been stated in the Chapter 1, due to its proximity to the border between A-type and modulated AFM structure, the balance between competing superexchange interactions in  $\text{GdMnO}_3$  is expected to more subtle. Hence, it will be of interest to elucidate spin-phonon coupling effects in  $\text{Gd}_{1-x}\text{Y}_x\text{MnO}_3$  system. Additionally, the improper ferroelectric transition in this system is inferred from the dielectric studies (Chapter 4). Raman scattering studies, traditionally used to probe the conventional ferroelectric transition is employed to study the optical properties of  $\text{Gd}_{1-x}\text{Y}_x\text{MnO}_3$  both as a function of  $x$  and temperature covering relevant magnetic transition temperatures.

## 5.2. Room temperature Raman studies

The Raman spectra of  $\text{Gd}_{1-x}\text{Y}_x\text{MnO}_3$  ( $x=0, 0.2, 0.3, 0.4$ ) samples measured at room temperature are show in Fig. 5.1. For the sake of comparison, spectra were normalized with respect to the intensity of a Raman mode at  $480 \text{ cm}^{-1}$ . Raman modes arise due to structural distortion of the present orthomanganite system against the ideal cubic Perovskite. Among allowed 60 normal modes at the  $\Gamma$  point of Brillouin, only 24 modes are Raman active. These modes can be decomposed into irreducible representation of  $mmm$  point group as

$$\Gamma = 7A_g + 5B_{1g} + 7B_{2g} + 5B_{3g}$$

Mode assignments of the Raman peaks were carried out following the works of Ilive et. al. [8] and are enumerated in Table 5.1.

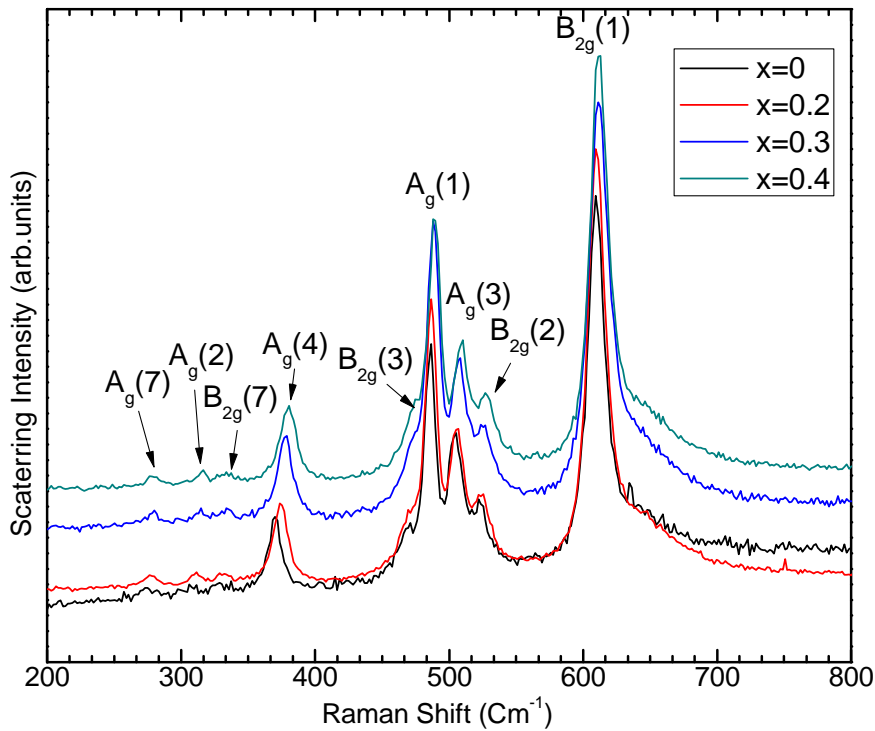


Figure.5.1: Raman spectrum of  $Gd_{1-x}Y_xMnO_3$  ( $x=0, 0.2, 0.3$  &  $0.4$ ) at room temperature depicting various modes.

Fivefold degenerate  $A_g$  modes and four fold degenerate  $B_{2g}$  modes are clearly seen. Their association with the specific kind of lattice distortion is shown in table 5.1. Among these,  $A_g$  and  $B_{2g}$  are the most intense modes and are the ones which are reported in various studies. The three Raman modes  $A_g(7)$ ,  $A_g(2)$  and  $B_{2g}(7)$  associated with the vibration of R-O ions have lower intensities as compared to the rest of the Raman modes. The other six relatively intense peaks are associated with  $MnO_6$  octahedra. From the symmetry consideration it is seen that, vibrational motion of  $O^{2-}$ -ions and not that of  $Mn^{3+}$ -ions contribute to Raman spectrum. This results in rotation, tilt, symmetric and anti-symmetric oxygen stretch or J-T tilt, or in phase stretching of the octahedron. Due to shorter bond length of Mn-O compared to that of R-O, Raman modes associated with octahedra are more intense compared to those associated with R-O.

Mode	Atomic motion	distortion
Ag(1)	O2 anti stretching	JT
Ag(2)	In-phase MnO6 y rotaion	[010]
Ag(3)	MnO6 bending	[101]
Ag(4)	Out of phase MnO6 x rotation	[101]
Ag(7)	O1(x)	R shift
B2g(1)	In-plane O2 stetching	JT
B2g(2)	In-phase O2 scissorlike	[010]
B2g(3)	Out of phase MnO6 bending	[101]
B2g(7)	O1(z)	R shift

Table.5.1: Table showing the various Raman modes and their assoiciation with lattice distortions.

The Raman spectrum of  $\text{GdMnO}_3$  matches with those reported in the literature [5]. It is seen that with  $\text{Y}^{3+}$  substitution, no disorder induced additional peaks in the Raman spectrum could be observed. The Raman modes however shift systematically to higher wave numbers with  $x$ . This clearly indicates that  $\text{Gd}_{1-x}\text{Y}_x\text{MnO}_3$  belong to a class of mixed crystals exhibiting amalgamation type or single mode optical properties. The relative intensity of the Raman modes, specifically those of  $A_g(1)$  and  $A_g(3)$  remains unaltered with  $\text{Y}^{3+}$  substitution. However, flipping in the intensity of these two modes have been reported for  $\text{Eu}_{1-x}\text{Y}_x\text{MnO}_3$  system [9].

This is reasoned to arise due to mixing of  $A_g(1)$  and  $A_g(3)$  modes. Such a mode mixing is well documented for  $\text{RMnO}_3$  system with the rare earth ionic radius in the range 1.09–1.14 Å [10].

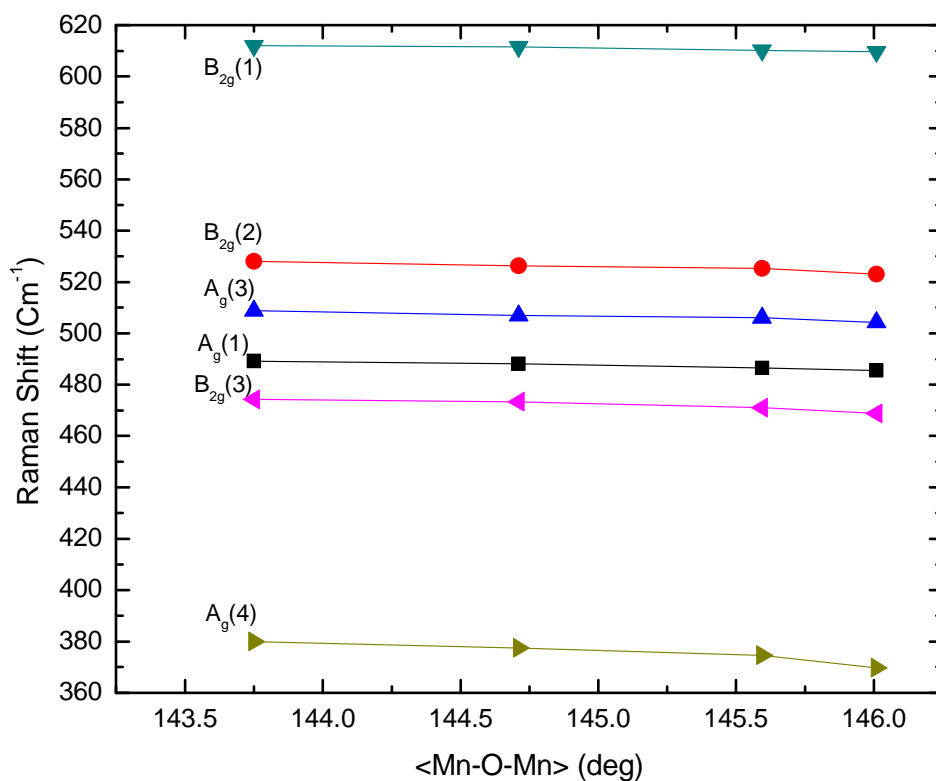


Figure.5.2: Raman mode shift with bond angle variation for  $Gd_{1-x}Y_xMnO_3$  ( $x=0, 0.2, 0.3$  &  $0.4$ ).

While the average rare earth ionic radius of the  $Eu_{1-x}Y_xMnO_3$  system falls in the range for strong mode mixing, Y substitution moves  $GdMnO_3$  away from it. In Fig. 5.2. the peak position of the Raman modes is plotted as function of  $\langle Mn-O-Mn \rangle$  bond angle which varies with Y concentration. Though, the shift in the peak position of the modes is almost linear with increasing concentration, the rate of shifts are different;  $A_g(4)$  mode exhibits the maximum shift of  $\sim 4 \text{ cm}^{-1}/\text{deg}$ ,  $B_{2g}(1)$  mode undergoes a shift of  $0.95 \text{ cm}^{-1}/\text{deg}$  and other modes shift with a slope in range of  $1.5$  to  $2.2 \text{ cm}^{-1}/\text{deg}$ . These shift especially of  $A_g(1)$  mode is far less compared to reported shifts for  $RMnO_3$  system [10] but compares well with those reported for  $Eu_{1-x}Y_xMnO_3$  system [9]. Larger shift of  $A_g(4)$  mode, associated with the octahedral rotation compared to that of tilt mode implies larger change in Mn-O-Mn bond angle in  $ab$ -plane compared to changes in

Mn-O-Mn along the  $c$ -axis. This is in complete agreement with the results of X-ray diffraction studies. The  $B_{2g}(1)$  is known to be insensitive to changes in the R-ionic radius of  $RMnO_3$  system [10]. Accordingly, the  $B_{2g}(1)$ , among others exhibits lesser shift with Y substitution.

### 5.2.1. Low temperature Raman studies

Raman spectra for  $x=0, 0.2, 0.3$  and  $0.4$  at select temperatures are shown in Fig. 5.3.

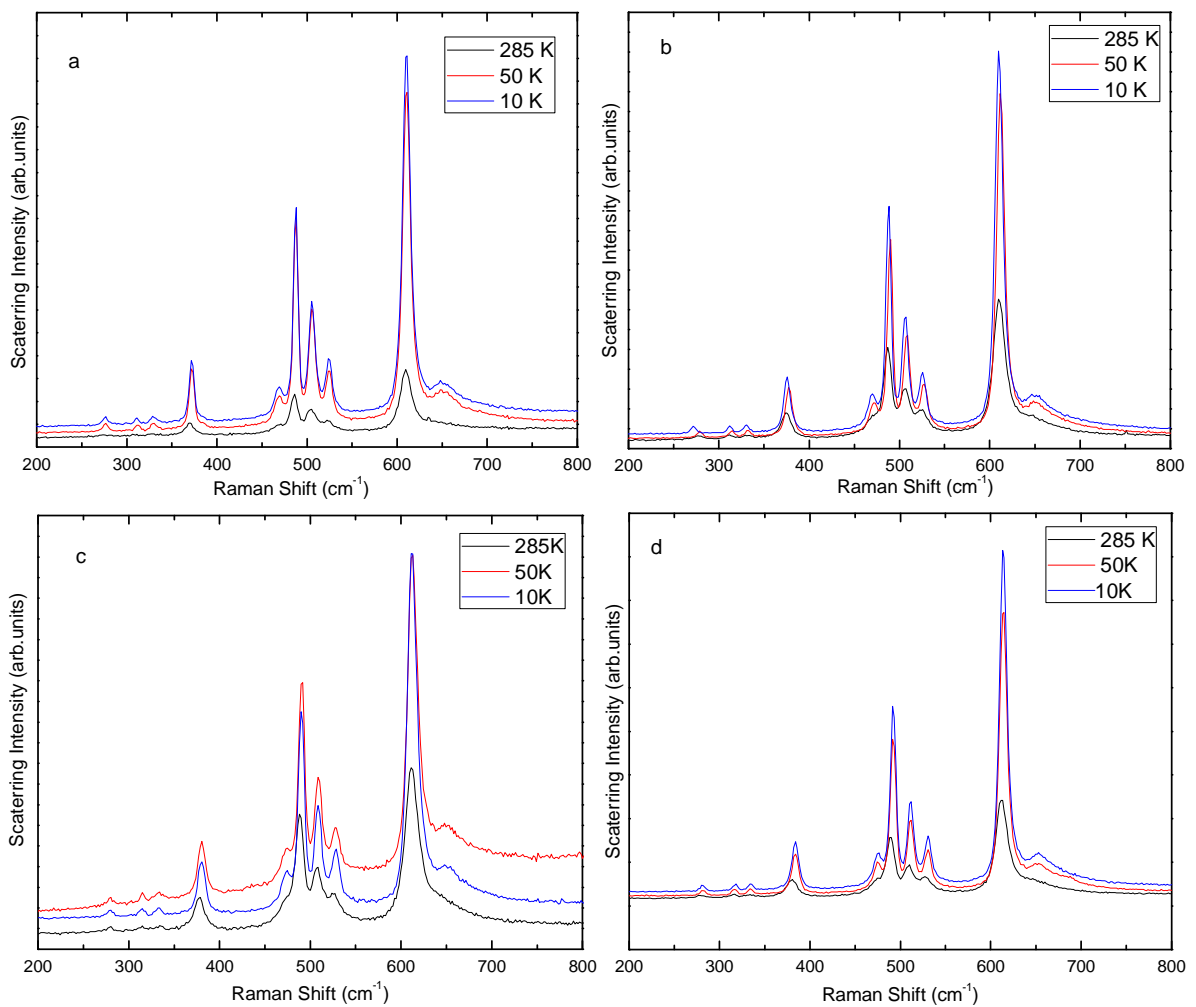


Figure.5.3: Raman spectrum of  $Gd_{1-x}Y_xMnO_3$  for a)  $x=0$ , b)  $x=0.2$ , c)  $x=0.3$  & d)  $x=0.4$  at select few temperature. The patterns have been shifted for clarity.

For all samples neither emergence of new modes nor disappearance of Raman modes is observed indicating absence of phase transformation at sub-ambient temperatures. In general, the width of the Raman peaks narrows down considerably as temperature is decreased. The Raman spectra were decomposed based on the allowed modes and accordingly fitted to Voigt function. Variation of the peak position of Raman modes with temperature for  $x=0, 0.2, 0.3$  and  $0.4$  are shown in Fig.5.4.

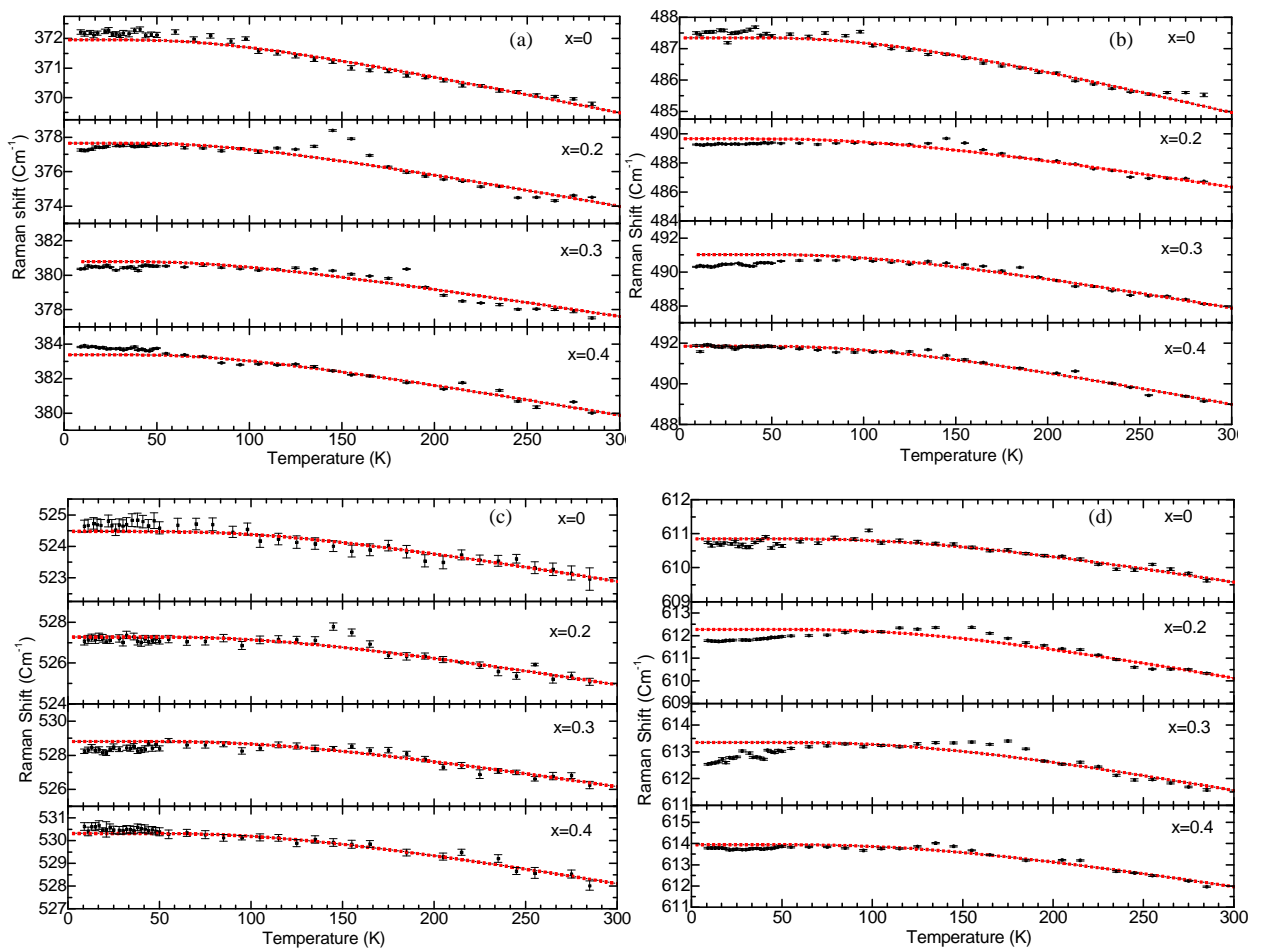


Figure.5.4: Variation of Raman modes with temperature for  $A_g(4)$ ,  $A_g(1)$ ,  $B_{2g}(3)$ , and  $B_{2g}(1)$  for all the composition. Red curve shows the fitting of anharmonic equation.

All the Raman modes shows shift to higher wave numbers with decreasing temperature. The modes in general shift faster initially as the temperature is lowered and flattens out below ~80 K. Total shift  $\Delta\omega_{total}$  ( $= \omega(10K) - \omega(300K)$ ) of the individual modes are shown in Fig. 5.5. Among all the modes, maximum hardening is observed for the  $A_g(4)$  mode and least for  $B_{2g}(3)$  mode. All modes exhibit a dip for  $x=0.3$  substitution in otherwise increasing trend of  $\Delta\omega_{total}$ .

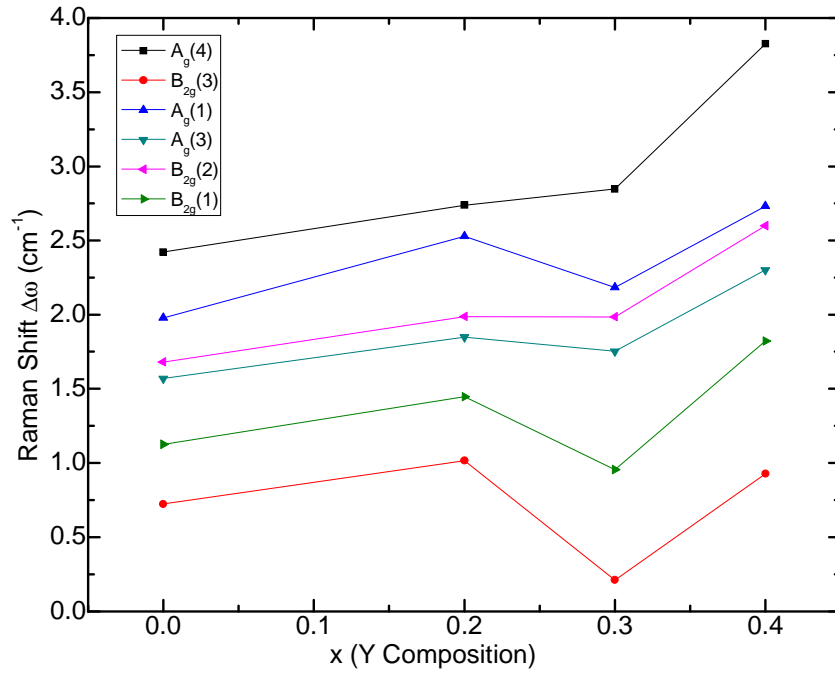


Figure.5.5: Total Raman shift of the individual modes for different composition.

In general, contributions to temperature dependent variation of phonon frequency  $\omega(T)$  is given by

$$\omega(T) = \omega(0) + (\Delta\omega)_{qh}(T) + (\Delta\omega)_{anh}(T) + (\Delta\omega)_{el-ph}(T) + (\Delta\omega)_{sp-ph}(T)$$

where  $\omega(0)$  is temperature independent contribution from harmonic vibration,  $(\Delta\omega)_{qh}$  corresponds to the change in phonon frequency due lattice parameter variations and is called quasi harmonic

part,  $(\Delta\omega)_{anh}$  accounts for changes due to anharmonic vibration. The term arises due to anharmonic shift at constant volume. The term  $(\Delta\omega)_{el-ph}$  is due to renormalization of electronic states near spin ordering temperature arising due to electron-phonon coupling. The last term  $(\Delta\omega)_{sp-ph}$ , arises due to the spin-phonon coupling arising due to the modulation of exchange integral by lattice vibrations. The fractional change in the volume is quite negligible so the quasi harmonic term can be neglected. As the samples are highly insulating, the electron-phonon renormalization contribution can also be safely neglected. This leaves two contributions  $(\Delta\omega)_{anh}$  and  $(\Delta\omega)_{sp-ph}$  for the consideration of  $\omega(T)$ . The expected variation of phonon frequency due to anharmonic phonon-phonon scattering is given by [11]

$$\omega(T) = \omega(0) - C \left[ 1 + \frac{2}{(e^{h\omega/kT} - 1)} \right]$$

where  $k_B$  is the Boltzmann's constant. The relation for  $\omega(T)$  was used to fit shift of the individual modes in the temperature interval of 70 to 300 K, i.e. in the paramagnetic region by treating  $C$  as a fitting parameter and extrapolated to cover the temperature range of measurement. The fitting is shown in Fig.5.4. A good fitting to the experimental data set could be obtained only down to 100K. Below ~100 K deviations as either anomalous hardening or softening of the modes is observed. The deviation from the anharmonic contribution evidences the spin-phonon coupling present in the system. It is pertinent to note that, while single crystals of  $GdMnO_3$  exhibit such deviations [12], same was not observed in polycrystalline sample [5]. Apart from this, no additional anomaly corresponding to other transition of  $Mn^{3+}$ -sublattice MT2 is observed. The deviation sets in at much higher temperature, about twice compared to that of magnetic transition temperature MT1 of the  $Mn^{3+}$ -sublattice. Such a behaviour has been reported not lonely in other ortho-manganite multiferroic systems [13], but also in double Perovskites [14], chromates [15] and in  $FeF_2$  and  $MnFe_2$  [16] as

well. The  $O_2$  in-phase symmetric stretching mode shows negative deviation in all the composition and also has the maximum deviation among all the Raman modes. This is because the  $Mn^{3+}$  spins within the  $MnO_2$  (ab) plane are ferromagnetically coupled and any symmetric moments of the  $O^{2-}$  ions should show stronger spin phonon coupling. The same has been shown for  $Eu_{1-x}Y_xMnO_3$  system and other  $RMnO_3$  systems [12].

Additional shift observed in certain Raman modes due to spin-phonon coupling was calculated as the difference between extrapolated anharmonic contribution with respect to the shift observed at 10K ( $= \omega_{ah}(10K) - \omega_{exp}(10K)$ ). In Fig. 5.6 variation of  $(\Delta\omega)_{sp}$  of certain modes with x is shown. Anomalous softening ( $\Delta\omega_{sp} < 0$ ) of  $B_{2g}(1)$  corresponding to in-phase stretching of Mn-O bond length is observed for all x. Such a feature has been reported for  $Eu_{1-x}Y_xMnO_3$  system [12].

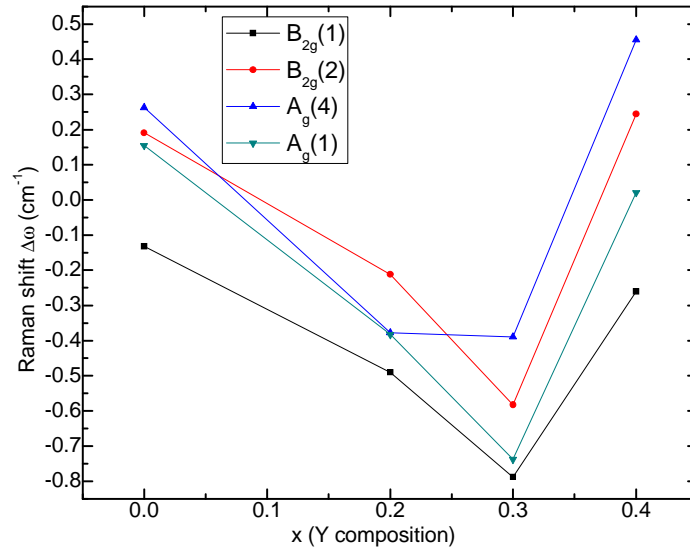


Figure.5.6: Total Raman shift between anharmonic extrapolated curve and experimental curve at 10K

Among the observed modes, least variation in  $\Delta\omega_{sp}$  with x is for the  $A_g(4)$  mode. For  $x=0.2$  and  $0.3$ , all the modes exhibit anomalous softening. For other concentrations, mixed

behavior is observed. The full width at half maximum (FWHM) of the Raman mode is related to the life time of the phonon. With decrease of temperature, the lattice parameters decrease due to anharmonicity, leading to changes in the life time. As per the standard model, the temperature dependence of FWHM,  $\Gamma(T)$  changes as [11]

$$\Gamma(T) = \Gamma(0) + A \left[ 1 + \frac{2}{(e^{h\omega/kT} - 1)} \right]$$

Accordingly,  $\Gamma(T)$  was fitted to above equation.

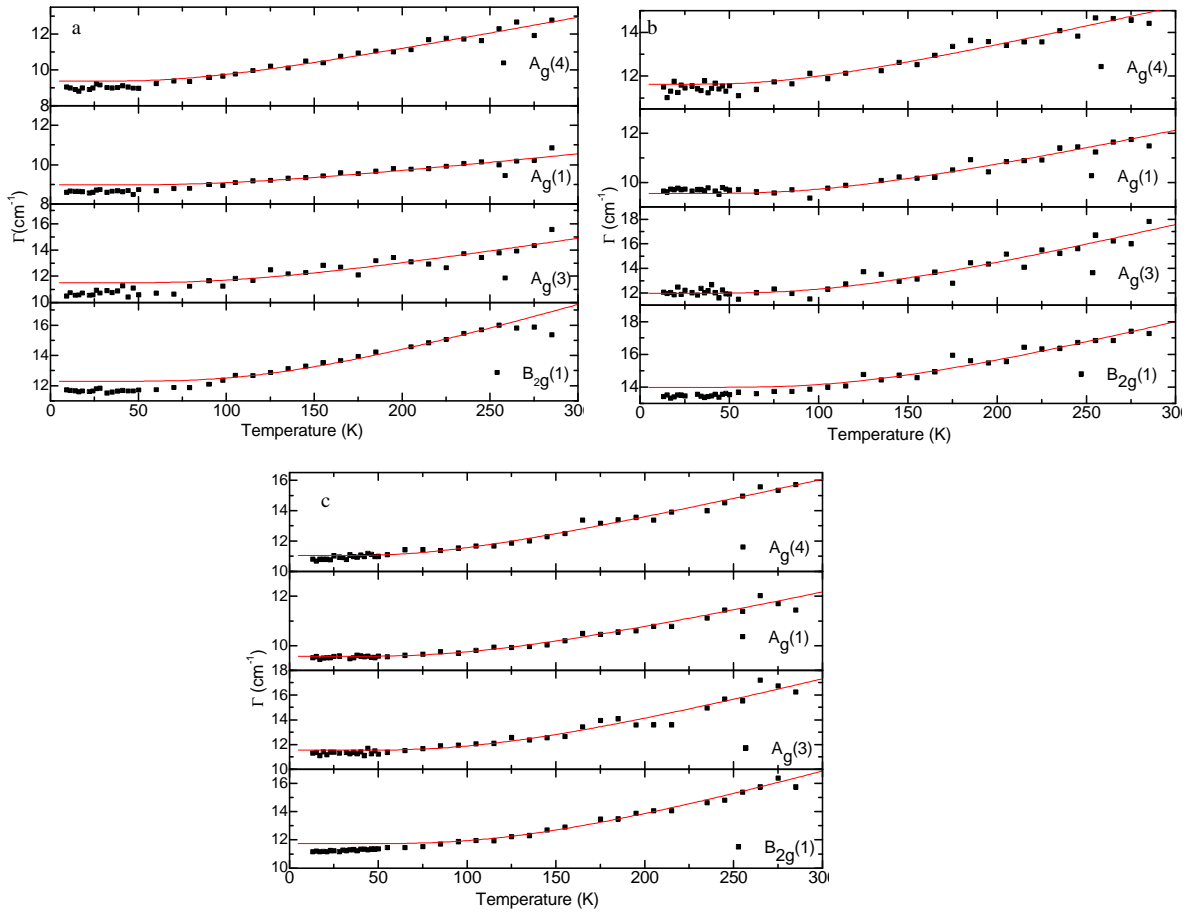


Figure.5.7: Variation of FWHM and their fitting (red curve) for  $\text{Gd}_{1-x}\text{Y}_x\text{MnO}_3$  ( $x=0, 0.3$  and  $0.4$ )

In Fig. 5.7, temperature variation of FWHM along with corresponding fit are shown for  $\text{Gd}_{1-x}\text{Y}_x\text{MnO}_3$  ( $x=0, 0.3$  and  $0.4$ ), with  $B_{2g}(1)$  mode, exhibiting maximum of anomalous softening. Except for  $A_g(1)$  mode of  $x=0.3$  sample, the  $\Gamma(T)$  of all modes of all the samples exhibit varying extent anomalous narrowing of than expected. This, in conjunction with anomalous variation in  $\omega(T)$  as discussed above, establishes spin-phonon coupling in the  $\text{Gd}_{1-x}\text{Y}_x\text{MnO}_3$ .

### 5.3. Band structure and phonon density calculation

To understand the effect of Y substitution on the vibration and electronic properties of  $\text{GdMnO}_3$  and how these affect the multiferroic nature of the material, detailed electronic structure and phonon dispersion calculations have been carried out. Density functional *ab-initio* calculations using plane wave methods as implemented in the WIEN2k code [17] was used for obtaining the electronic structure, while the lattice dynamics program GULP in Materials Studio [18] was used for calculating the phonon dispersions and the density of states of  $\text{Gd}_{1-x}\text{Y}_x\text{MnO}_3$ . The details of the calculation have been explained in chapter 2.

The spin polarized total and atom decomposed density of states (DOS) of  $\text{Gd}_{1-x}\text{Y}_x\text{MnO}_3$  ( $x = 0, 0.25, 0.5$  and  $1$ ) without the spin-orbit (SO) coupling are shown in Fig.5.8 and Fig.5.9 for the spin-up and spin-down cases. Spin-orbit interaction uses a second variational method with the scalar-relativistic orbitals as the basis. The number of eigenvalues doubles since SO couples the spin-up and spin-down states. The SO states are no longer separable and become a single state. Hence, the up- and down-spin density of states have been calculated without accounting for the spin-orbit coupling, while the band structures have been calculated for both the cases. The

compositions of the compound were chosen mainly keeping in mind the ease of computation. The crystal system has been assumed to be *Pnma* for the two end compounds. This finds support in the experimental observation that hexagonal  $\text{RMnO}_3$  systems (e.g.  $\text{YMnO}_3$ ) can be stabilized in orthorhombic crystal structure under high pressure synthesis. The figures have been plotted to show the contributions of all the atoms present in the unit cell for comparison across all the compositions. From the figures it is clear that in  $\text{GdMnO}_3$ , the contributions to the valence band in at the Fermi level ( $E_F$ ) are from the O  $2p$  and Mn  $3d$  states. Away from the Fermi level the predominant contribution is from the O and Mn levels in the  $\pm 6$  eV energy window from the Fermi level. The localized  $5f$  levels of Gd are beyond 6 eV from  $E_F$  in both in the valence band as well as the conduction band. The  $\text{YMnO}_3$  DOS plots look similar except for the absence of the strongly localized  $f$  bands. The Y levels do not contribute to the DOS much to the valence band states in the plotted energy range, but are seen to be prominent contributors to the conduction band states beyond 4 eV. The DOS of all the compounds is compared in Fig.5.10. It clearly shows the effect of increasing Y substitution. It can be seen from the figures that the  $E_F$  shifts to higher energy by a constant amount with increase in Y concentration. The Gd  $5f$  states do not show any effect of the Y substitution, but the Mn  $3d$  and O  $2p$  states broaden by a significant amount. Thus the band gap of the system decreases upon Y substitution. While, both the end compounds show a band gap of 2.1 eV for  $\text{GdMnO}_3$  and 2.2 eV for  $\text{YMnO}_3$ , the band gaps decrease to 1.4 eV for  $x = 0.25$  and 1.5 eV for  $x = 0.5$  compounds. All the band gap values have been quoted from the calculations where SO interactions have been accounted for.

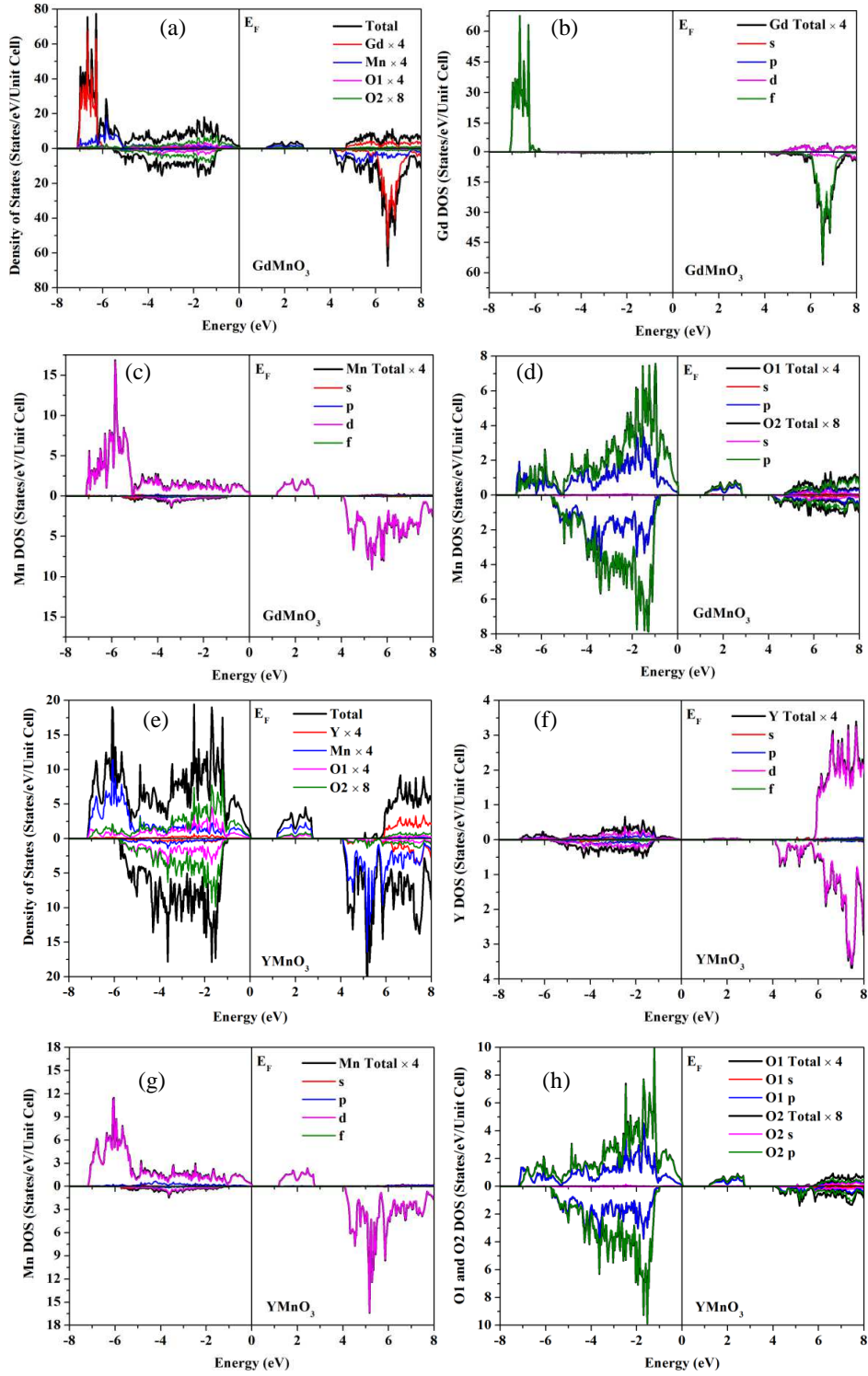


Figure.5.8: Partial and total density of states of (a)  $\text{GdMnO}_3$ , (b) Gd, (c) Mn and (d) O contribution to  $\text{GdMnO}_3$  DOS , (e)  $\text{YMnO}_3$ , (f) Y, (g) Mn and (h) O contribution to  $\text{YMnO}_3$  DOS.

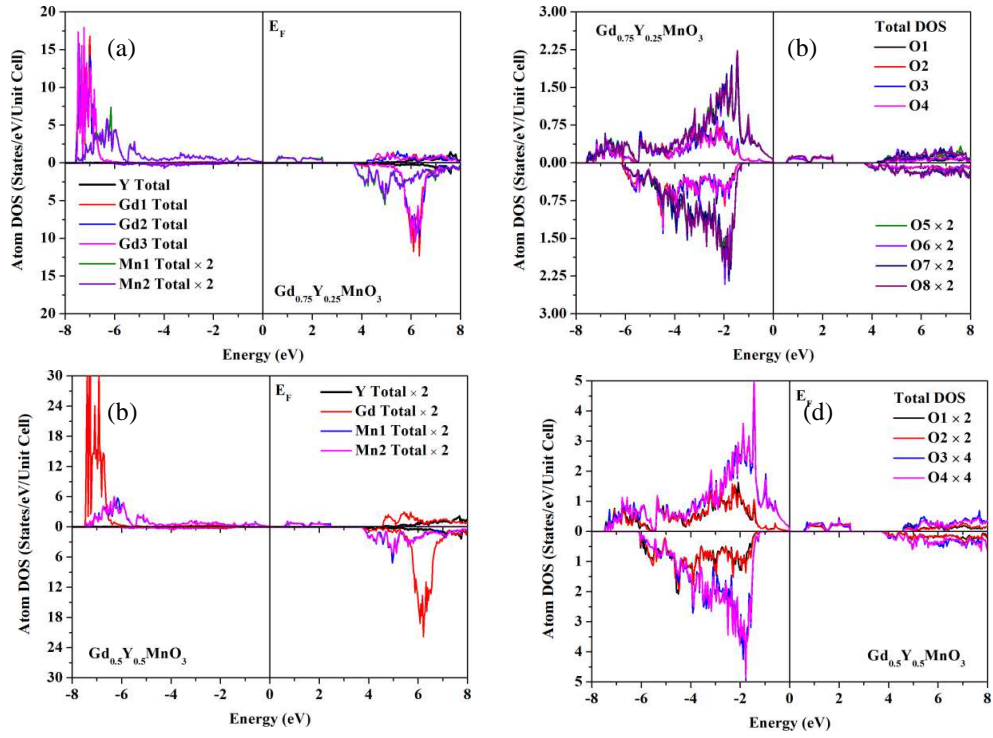


Figure.5.9: partial density of states of (a)  $\text{Gd}_{0.25}\text{Y}_{0.75}\text{MnO}_3$ , (b) O contribution to  $\text{Gd}_{0.25}\text{Y}_{0.75}\text{MnO}_3$  DOS, (c)  $\text{Gd}_{0.5}\text{Y}_{0.5}\text{MnO}_3$  and (d) O contribution towards  $\text{Gd}_{0.5}\text{Y}_{0.5}\text{MnO}_3$

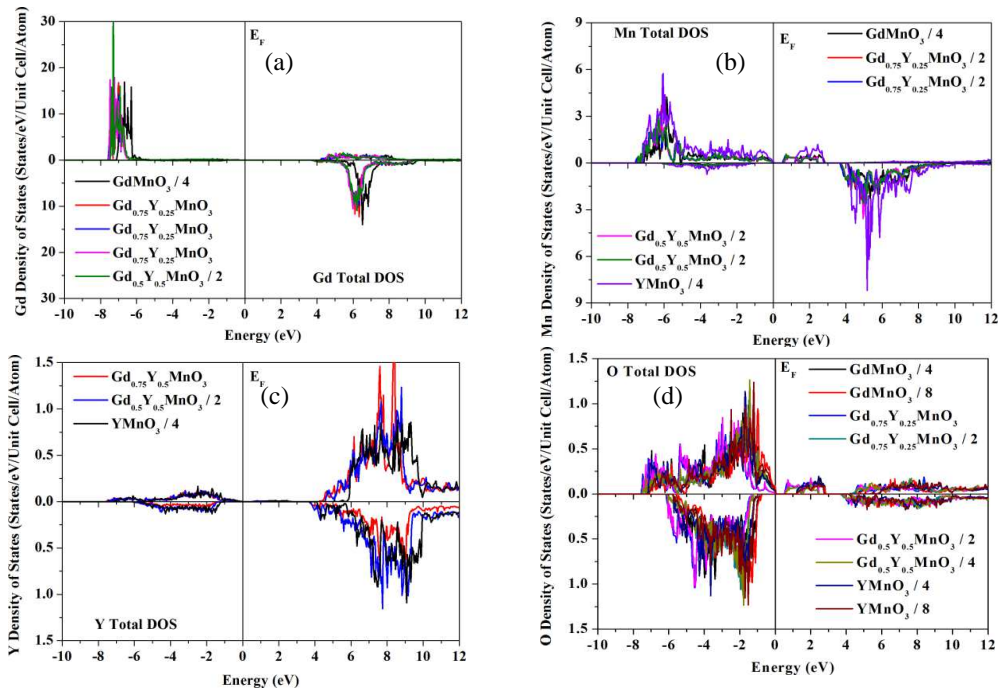


Figure.5.10: Total DOS of (a) Gd in  $\text{GdMnO}_3$ ,  $\text{Gd}_{0.25}\text{Y}_{0.75}\text{MnO}_3$  and  $\text{Gd}_{0.5}\text{Y}_{0.5}\text{MnO}_3$ , (b) Mn in  $\text{GdMnO}_3$ ,  $\text{Gd}_{0.25}\text{Y}_{0.75}\text{MnO}_3$ ,  $\text{Gd}_{0.5}\text{Y}_{0.5}\text{MnO}_3$  and  $\text{YMnO}_3$ , (c) Y in  $\text{YMnO}_3$ ,  $\text{Gd}_{0.25}\text{Y}_{0.75}\text{MnO}_3$  and  $\text{Gd}_{0.5}\text{Y}_{0.5}\text{MnO}_3$  and (d) O in  $\text{GdMnO}_3$ ,  $\text{Gd}_{0.25}\text{Y}_{0.75}\text{MnO}_3$ ,  $\text{Gd}_{0.5}\text{Y}_{0.5}\text{MnO}_3$  and  $\text{YMnO}_3$ .

The SO band structures of  $\text{Gd}_{1-x}\text{Y}_x\text{MnO}_3$  ( $x = 0, 0.25$  and  $0.5$ ) and  $\text{YMnO}_3$  in the  $Pnma$  space group along the high symmetry directions are shown in Fig.5.11. The Mn  $3d$  levels are seen to be hybridized with the O  $2p$  levels, which broaden on Y substitution in  $\text{GdMnO}_3$ . Apart from this no significant change in the band structures can be seen. All the compounds are seen to have a direct fundamental band gap at the  $\Gamma$  point.

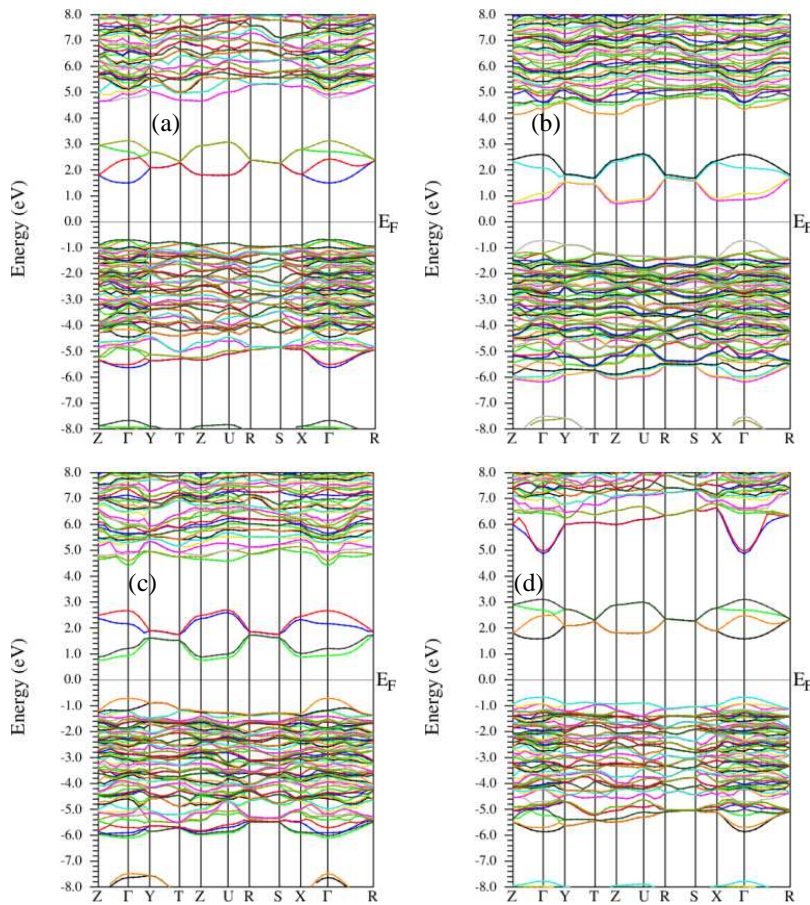


Figure.5.11: Electronic band structures of (a)  $\text{GdMnO}_3$ , (b)  $\text{Gd}_{0.25}\text{Y}_{0.75}\text{MnO}_3$ , (c)  $\text{Gd}_{0.5}\text{Y}_{0.5}\text{MnO}_3$  and (d)  $\text{YMnO}_3$ .

The relaxed lattice parameters, atom positions, various characteristics of the Mn-O octahedron and the Mn-O-Mn bond angles, along with the total magnetic moment per formula unit and the calculated fundamental band gaps are given in the table 5.2 below.

	<b>GdMnO<sub>3</sub></b>	<b>Gd<sub>0.75</sub>Y<sub>0.25</sub>O<sub>3</sub></b>	<b>Gd<sub>0.5</sub>Y<sub>0.5</sub>O<sub>3</sub></b>	<b>YMnO<sub>3</sub></b>
a (Å)	5.866	5.8536	5.8514	5.797
b (Å)	7.431	7.4190	7.4027	7.3606
c (Å)	5.318	5.3040	5.2928	5.2404
Y/Gd	0.0829, 0.25, 0.4816 (Gd) 0.9171, 0.75, 0.5184 (Gd) 0.4171, 0.75, 0.9816 (Gd) 0.5829, 0.25, 0.0184 (Gd)	0.0821, 0.2488, 0.4816 (Y) 0.9183, 0.7488, 0.5180 (Gd) 0.4182, 0.7488, 0.9820 (Gd) 0.5810, 0.2488, 0.0185 (Gd)	0.0829, 0.25, 0.4815 (Y) 0.9171, 0.75, 0.5185 (Y) 0.5832, 0.25, 0.0190 (Gd) 0.4168, 0.75, 0.9810 (Gd)	0.0834, 0.25, 0.4806 (Y) 0.9166, 0.75, 0.5192 (Y) 0.4166, 0.75, 0.9806 (Y) 0.5834, 0.25, 0.0194 (Y)
Mn	0, 0, 0 0, 0.5, 0 0.5, 0, 0.5 0.5, 0.5, 0.5	0, 0, 0 0, 0.4976, 0 0.4982, 0.9995, 0.5006 0.4982, 0.4981, 0.5006	0, 0, 0 0, 0.5, 0 0.5, 0, 0.5 0.5, 0.5, 0.5	0, 0, 0 0, 0.5, 0 0.5, 0, 0.5 0.5, 0.5, 0.5
O1	0.4683, 0.25, 0.6066 0.5317, 0.75, 0.3934 0.0317, 0.75, 0.1066 0.9683, 0.25, 0.8934	0.4622, 0.2488, 0.6060 0.5328, 0.7488, 0.3942 0.0309, 0.7488, 0.1040 0.9656, 0.2488, 0.8876	0.4615, 0.25, 0.6073 0.5385, 0.75, 0.3927 0.9672, 0.25, 0.8881 0.0328, 0.75, 0.1119	0.4619, 0.25, 0.6128 0.5381, 0.75, 0.3871 0.0381, 0.75, 0.1128 0.9619, 0.25, 0.8871
O2	0.3224, 0.0515, 0.2033 0.6776, 0.9485, 0.7967 0.1776, 0.9485, 0.7033 0.8224, 0.0515, 0.2967 0.6776, 0.5515, 0.7967 0.3224, 0.4485, 0.2033 0.8224, 0.4485, 0.2967 0.1776, 0.5515, 0.7033	0.3180, 0.0507, 0.2051 0.3180, 0.4469, 0.2051 0.6775, 0.9485, 0.7969 0.6775, 0.5491, 0.7969 0.1787, 0.9486, 0.7036 0.1787, 0.5490, 0.7036 0.8238, 0.0526, 0.2978 0.8238, 0.4450, 0.2978	0.3210, 0.0519, 0.2043 0.6790, 0.9481, 0.7957 0.6790, 0.5519, 0.7957 0.3210, 0.4481, 0.2043 0.1743, 0.9471, 0.7018 0.8257, 0.0529, 0.2982 0.8257, 0.4471, 0.2982 0.1743, 0.5529, 0.7018	0.3222, 0.0535, 0.1997 0.6778, 0.9464, 0.8003 0.1778, 0.9464, 0.6997 0.8222, 0.0535, 0.3003 0.6778, 0.5535, 0.8003 0.3222, 0.4464, 0.1997 0.8222, 0.4464, 0.3003 0.1778, 0.5535, 0.6997
<b>Mn-O Octahedron</b>				
V <sub>O</sub> (Å <sup>3</sup> )	11.08	11.02	10.97	10.82
l <sub>av</sub> (Å)	2.03	2.03	2.02	2.01
D	0.059	0.057	0.058	0.053
<λ>	1.0093	1.0089	1.0092	1.0085
σ <sup>2</sup> (degree <sup>2</sup> )	5.0	5.8	5.7	7.3
Apical Mn-O-Mn (°)	144.39	145.40	142.82	142.13
Planar Mn-O-Mn (°)	145.82	146.15	144.69	144.75
M/formula unit (μ <sub>B</sub> )	10.99 (Gd ≈ 7, Mn ≈ 3.8)	9.24 (Gd ≈ 7, Y ≈ 0, Mn ≈ 3.8)	7.50 (Gd ≈ 7, Y ≈ 0, Mn ≈ 3.8)	4 (Y ≈ 0, Mn ≈ 3.8)
E <sub>g</sub> (eV)	1.196 (no so), 2.1 (so)	0.518 (no so), 1.4 (so)	0.585 (no so), 1.5 (so)	1.213 (no so), 2.2 (so)
B <sub>0</sub> (GPa)	235.55	237.17	238.80	242.19
ε <sub>0</sub> (xx, yy, zz)	12.33, 23.19, 11.53	12.20, 25.57, 11.53	12.16, 28.30, 11.61	11.89, 35.89, 11.47
ε <sub>∞</sub> (xx, yy, zz)	2.17, 2.18, 2.17	2.18, 2.19, 2.17	2.19, 2.20, 2.18	2.20, 2.22, 2.20

Table 5.2: Lattice Parameters, atomic positions and Mn-O octahedra characteristics as obtained from the relaxed ground state configurations obtained from DFT. The fundamental band gaps and the magnetic moments per formula unit and for the individual atoms are also given. The table also shows the values of the bulk modulus and the static and high frequency dielectric constants obtained for the various compounds from the GULP lattice dynamical calculations.

It also shows the bulk modulus and the static and high frequency dielectric constants obtained from the lattice dynamical calculations. The polyhedral volume,  $V_O$ , average bond length,  $l_{av}$ , distortion index,  $D$ , quadratic elongation,  $\langle\lambda\rangle$ , and bond angle variance,  $\sigma^2$ , are defined as below [19].

$$D = \frac{1}{n} \sum_{i=1}^n \frac{|l_i - l_{av}|}{l_{av}}, \text{ where } l_i = \text{distance from the central atom to the } i^{\text{th}} \text{ coordinating atom,}$$

and  $l_{av}$  = average bond length.

$$\langle \lambda \rangle = \frac{1}{n} \sum_{i=1}^n \left( \frac{l_i}{l_0} \right)^2, \text{ } l_0 = \text{center-to-vertex distance of a regular polyhedron of the same}$$

volume.

$\sigma^2 = \frac{1}{m-1} \sum_{i=1}^m (\phi_i - \phi_0)^2$ ,  $m$  = (number of faces in the polyhedron)  $\times 3/2$  (i.e., number of bond angles),  $\phi_i = i^{\text{th}}$  bond angle, and  $\phi_0$  = ideal bond angle for a regular polyhedron ( $90^\circ$  for an octahedron).

The phonon dispersions for  $\text{GdMnO}_3$  and  $\text{YMnO}_3$  along were calculated along the path containing the high symmetry directions  $\text{W-L-}\Gamma\text{-X-W-K-}\Gamma$  and phonon density of states were calculated for the series of  $\text{Gd}_{1-x}\text{Y}_x\text{MnO}_3$  ( $0 \leq x \leq 1$ ) using GLUP program in Materials Studio package. The phonon dispersion curves of the end members  $\text{GdMnO}_3$  and  $\text{YMnO}_3$  are shown in Fig.5.12. No phonon gap can be observed in the dispersions. The phonon density of states for  $\text{Gd}_{1-x}\text{Y}_x\text{MnO}_3$  ( $0 \leq x \leq 1$ ) is compared in Fig.5.13. The peaks in the phonon density of states of  $\text{GdMnO}_3$  and  $\text{YMnO}_3$  are seen to occur at almost the same energy and it is seen that there is a gradual change in all the peak positions as we go from  $\text{GdMnO}_3$  to  $\text{YMnO}_3$  as a function of Y substitution. This is an indication of one mode behavior and is to be expected in the solid solution  $\text{Gd}_{1-x}\text{Y}_x\text{MnO}_3$  ( $0 \leq x \leq 1$ ) without the emergence of any new mode. This is also in agreement with the experimentally obtained spectrum for  $\text{Gd}_{1-x}\text{Y}_x\text{MnO}_3$  ( $0 \leq x \leq 0.4$ ) in the range of  $200 \text{ cm}^{-1}$  to  $800 \text{ cm}^{-1}$  discussed in previous section.

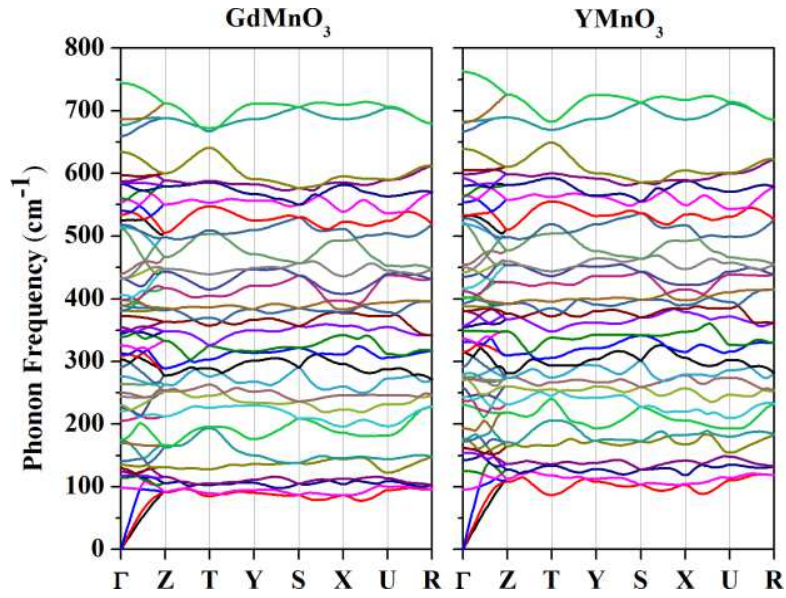


Figure.5.12: The phonon dispersion curves for  $\text{GdMnO}_3$  and  $\text{YMnO}_3$  along the high symmetry direction.

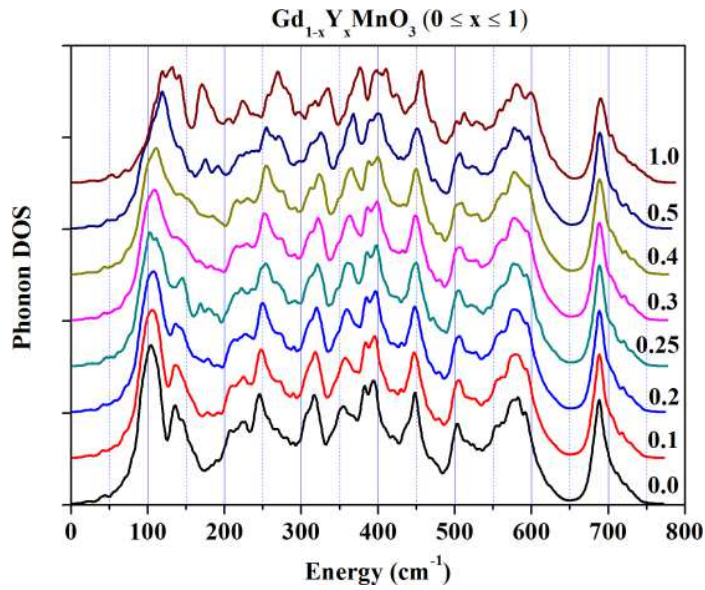


Figure.5.13: Phonon density of states for  $\text{Gd}_{1-x}\text{Y}_x\text{MnO}_3$  ( $0 \leq x \leq 1$ ).

We have also calculated the phonon DOS and dispersions of the end compounds using the VASP plane wave DFT package [20]. The total energy range for the phonons is smaller than that obtained from the lattice dynamical calculations, but it gives us the individual atomic contributions to the phonon density of states for  $\text{GdMnO}_3$  and  $\text{YMnO}_3$ , which are shown in

Fig.5.14. It is clear from the figure that the phonon modes at lower energies are predominantly contributed by Gd and Mn. These are the  $A_g(7)$ ,  $A_g(2)$  and  $B_{2g}(7)$  modes as observed experimentally and discussed in previous section. While the higher energy modes are due to  $O^{2-}$  ions. The phonon energies between the experimentally observed and those computed using GULP differs slightly but the overall pattern remains the same.

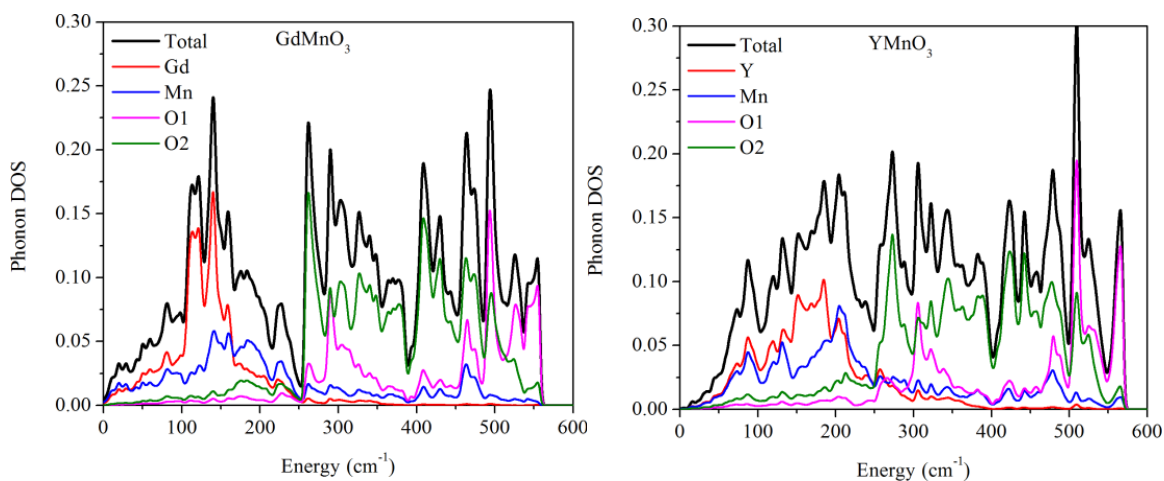


Figure.5.14: Individual atomic contribution to the density of states for  $GdMnO_3$  and  $YMnO_3$  as calculated from VASP.

The rest of the phonon density of states in middle and higher energy range is mainly due to the contributions from the Mn-O bonds and these correspond to the intense Raman modes observed in experiments. Thus the theoretical computation clearly reveals the nature of origin of Raman modes based on the atomic contribution.

## 5.4. Conclusion

The Raman modes of  $Gd_{1-x}Y_xMnO_3$  ( $0 \leq x \leq 0.4$ ) linearly shifts to higher wave numbers with increasing  $x$  evidencing increase in the orthorhombic distortion. Among these, the rotation mode i.e the  $A_g(4)$  mode exhibits largest shift while the symmetrical stretching  $B_{2g}(1)$  mode in

the *ab*-plane undergoes least shift. As the temperature is lowered, all the Raman modes shift to higher wave numbers and their full width at half maximum (FWHM) widths decreases. Both the hardening of the modes and narrowing of the peaks could be fitted to anharmonic model only up to 100 K. Below this temperature the modes exhibit either anomalous hardening or softening, riding over the harmonic contribution. Most of peaks exhibit anomalous narrowing below 100 K. Such an anomalous variation in the peak position, in the presence of anomalous reduction in FWHM clearly indicates the presence of spin phonon coupling present in the system.

The theoretically calculated phonon density of state also shows shift with increasing Y concentration. The individual atomic contributions to the phonon modes have been calculated by VASP which shows that the intense modes are mainly due to O<sup>2-</sup> ion movement.

## References:

- [1]. A. J. Millis, *Phys. Rev. B* **53** , 8434 (1996).
- [2]. W. Archibald, J.-S. Zhou, and J. B. Goodenough, *Phys. Rev. B* **53** , 14 445 (1995).
- [3]. A. J. Millis, P. B. Littlewood, and B. I. Shraiman, *Phys. Rev. Lett.* **74**, 5144 (1995).
- [4]. Silvia Picozzi and Claude Ederer, *J. Phys.: Condens. Matter* **21** 303201 (2009).
- [5]. J. Laverdière, S. Jandl, A. A. Mukhin, V. Yu. Ivanov, V. G. Ivanov, and M. N. Iliev, *Phys. Rev. B* **73** , 214301 (2006). Erratum *Phys. Rev. B* **74** , 179902 (2006).
- [6]. D A Mota , Y Romaguera Barcelay, P B Tavares, M R Chaves, A Almeida , J Oliveira, W S Ferreira and J Agostinho Moreira, *J. Phys.: Condens. Matter* **25**, 235602 (2013).
- [7]. E. Granado, A. García, J. A. Sanjurjo, C. Rettori, I. Torriani, F. Prado, R. D. Sánchez, A. Caneiro, and S. B. Oseroff, *Phys. Rev. B*, **60**, 11879 (1999).
- [8]. M. N. Iliev, M. V. Abrashev, H.-G. Lee, V. N. Popov, Y. Y. Sun, C. Thomsen, R. L. Meng, and C. W. Chu, *Phys. Rev. B*, **57**, 2872 (1998).
- [9]. S. Issing, F. Fuchs, C. Ziereis, E. Batke, A. Pimenov, Y. Vu. Ivanov, A. A. Mukhin and J. Geurts, *Eur. Phys. J. B* **73** 353(2010).
- [10]. M. N. Iliev, M. V. Abrashev, J. Laverdière, S. Jandl, M. M. Gospodinov, Y.-Q. Wang, and Y.-Y. Sun, *Phys. Rev. B* **73** 064302 (2006).
- [11]. M. Balkanski, R. F. wallis and E. Haro, *Phys. Rev. B* **28** 064302 (1983).
- [12]. S. Issing, A. Pimenov, Y. Vu. Ivanov, A. A. Mukhin and J. Geurts, *Eur. Phys. J. B* **78** 367(2010).
- [13]. W. S. Ferreira, J. Agostinho Moreira, A. Almeida, M. R. Chaves, J. P. Araújo, J. B. Oliveira, J. M. Machado Da Silva, M. A. Sá, T. M. Mendonça, P. Simeão Carvalho, J. Kreisel, J. L. Ribeiro and L. G. Vieira, P. B. Tavares and S. Mendonça, *Phys. Rev. B* **79** 054303 (2009).
- [14]. Raimundo Bezerra Macedo Filho, Alejandro Pedro Ayala and Carlos William de Araujo Paschoal , *Appl. Phys. Lett.* **102**, 192902 (2013).

- [15]. Venkata Srinu Bhadram, B. Rajeswaran, A. Sundaresan and Chandrabhas Narayana, *EPL* **101** 17008 (2013).
- [16]. D. J. Lockwood and M. G. Cottam, *J. Appl. Phys.* **64**, 5876 (1988).
- [17]. P. Blaha, K. Schwarz, G. K. H. Madsen, D. Kvasnicka and J. Luitz., *WIEN2K, An Augmented Plane Wave, Local Orbitals Program for Calculating Crystal Properties*, Karlheinz Schwarz, Technical Universität, Wien, Austria 2001 ISBN 3-9501031-1-2.
- [18]. J.D. Gale and A.L. Rohl, *Molecular Simulation*, **29**, 291-341 (2003).
- [19]. W. H. Baur, *Acta Crystallogr., Sect. B: Struct. Sci.*, **30**, 1195 (1974).
- [20]. G. Kresse and J. Hafner, *Phys. Rev. B* **47** RC558 (1993).

## Chapter 6

### Summary and scope for future work

Phase pure solid solutions of  $\text{Gd}_{1-x}\text{Y}_x\text{MnO}_3$  ( $x=0.2, 0.3$  &  $0.4$ ) were synthesized and their structural, dielectric, magnetic, magnet-caloric and vibrational properties were studied as a function of temperature. These investigations have helped in understanding some of the underlying properties of the system better. These investigations have also provided a greater clarity as to the underlying processes occurring in the system. We shall now recapitulate the central results in a nutshell.

The variation of structural parameters with composition was estimated through the Rietveld refinement of the XRD data. This is a rich source of information as for instance the nexus between Yttrium concentration and the Mn-O-Mn bond angle could be clearly brought out. The lattice parameter was found to decrease with increasing Yttrium concentration owing to the smaller ionic radius of  $\text{Y}^{3+}$  compared to that of  $\text{Gd}^{3+}$ . The reduction of the average ionic radius of the rare earth due to substitution with Y results in increased orthorhombic distortion, which in turn reduces the average Mn-O-Mn bond angle. The Mn-O-Mn bond angle is found to decrease from  $145.594(2)$  to  $143.75(1)$  as  $x$  increase from  $0.2$  to  $0.4$ . This is an important piece of information since this value falls more or less in the window range of bond angles that is favorable for the system to exhibit multiferroic properties. From the thermomagnetisation studies, specific magnetic transitions could not be identified. This is due to a substantial paramagnetic contribution coming from  $\text{Gd}^{3+}$  which carries a larger magnetic moment than  $\text{Mn}^{3+}$ . However, from the plot of inverse susceptibility with temperature, an antiferromagnetic (AFM) interaction is inferred with the Cuire-Weiss constant  $\theta_N \sim 32$  K. The nominal decrease in

$\theta_N$  ( $\sim 4$  K) is observed. On the other hand, specific heat studies confirmed the occurrence of two magnetic transitions: A  $\lambda$ -like transition around  $\sim 41$  K, associated with the paramagnetic to (collinear) sinusoidal antiferromagnetic transition of the  $\text{Mn}^{3+}$  sublattice  $T_{N1}^{Mn}$  and a second transition near 8 K due to magnetic ordering of  $\text{Gd}^{3+}$  sublattice in a canted antiferromagnetic structure  $T_N^{Gd}$ . While  $T_{N1}^{Mn}$  decreases marginally with  $x$ , no detectable change in  $T_N^{Gd}$  was observed. Apart from this, no other magnetic transition could be observed in the specific heat curve but for a weak anomaly about 18 K for  $x = 0.3$  composition alone.

Temperature dependent dielectric studies showed an anomaly in the form of a peak around  $\sim 18$  K for all the composition. This is associated with an improper ferroelectric transition driven by linear sinusoidal to cycloid AFM transition of  $\text{Mn}^{3+}$  sublattice ( $T_{N2}^{Mn}$ ), whereas, for the parent compound  $\text{GdMnO}_3$  a step like feature has been reported. This is associated with a linear sinusoidal to A-type AFM transition, which does not result in a ferroelectric transition. This establishes that the reduction of average ionic radius of the R-site by the substitution of Y results in a ferroelectric transition in the otherwise paraelectric  $\text{GdMnO}_3$ . The associated peak is slightly broader in comparison with those reported for single crystals of other systems. This is due to the polycrystalline nature of the samples used in the present study and also due to the temperature dependent dielectric variations along all the three crystallographic axes. Apart from this peak, another peak is observed at around 8 K for all compositions. This peak originates from the magnetic ordering of  $\text{Gd}^{3+}$  sublattice. This ordering also affects the dielectric property, as has been reported for the parent compound.

The dielectric relaxation behavior was studied both using the Arrhenius law as a function of temperature and by fitting the frequency dependent imaginary part of dielectric permittivity  $\epsilon''(\omega)$  by Cole-Cole function. It was seen that the plots could not be fitted to a single activation

energy  $E_a$  for the entire temperature range but required the use of three different values for  $E_a$ , corresponding to three different temperature ranges. The first change is observed at about  $T_{N1}^{Mn}$  for all the compositions of the  $Mn^{3+}$  sublattice. The second change of activation energy occurs at around 26 K, which corresponds neither to the magnetic transition of  $Gd^{3+}$  sublattice nor to that of  $Mn^{3+}$ . This needs to be further probed. The estimated activation energies match with that of the normal dielectric relaxation behavior. The fitting of  $\epsilon''(\omega)$  at different temperatures by Cole-Cole functions clearly establishes that the function does not follow the Arrhenius law over the entire temperature regime of study. This establishes that the dielectric process may not be a simple thermally activated one. The observed variation (bending) of relaxation time suggests that some tunneling process is probably involved. It is also germane to point out that the relaxation time is seen to slightly slow down close to 18K near the ferroelectric transition temperature.

The temperature dependence of the lattice parameters of  $Gd_{1-x}Y_xMnO_3$  was investigated with low temperature powder X-ray diffraction studies. For all the compositions, lattice parameter variations exhibit the expected positive thermal coefficient down to 100 K. At about  $T_{N1}^{Mn}$ , anomalous variations were observed for all compositions, indicating the presence of a magneto-elastic coupling. Except for  $x=0.3$ , a mixed variation of the lattice parameters was observed at about  $T_{N2}^{Mn}$ . For  $x=0.3$ , all parameters exhibit a considerable increase at around  $T_{N2}^{Mn}$  as the temperature is lowered, a feature observed for other reported systems as well.

The magneto-caloric studies on  $Gd_{1-x}Y_xMnO_3$  show that the system exhibits both normal and inverse magnetocaloric effect (MCE). As with the case of other multiferroics, the present system also shows huge MCE with an entropy change  $\Delta S$  of -16.102 mJ/gm-K and adiabatic temperature change  $(\Delta T)_{ada}$  of 5.4 K for  $x = 0.2$  composition for an applied magnetic field of 10T. Thus these materials would find good use in hydrogen liquefaction and space applications,

both of which involve low temperatures. The present work also demonstrates that the system shows magnetic field induced transition of the  $Gd^{3+}$  sublattice from antiferromagnetic to ferromagnetic ordering. From a change in the sign of both  $\Delta S$  and  $\Delta T$ , it is inferred that  $Gd^{3+}$ -sublattice undergoes AFM to FM transition for  $H \gtrsim 0.5 T$ .

Vibrational properties of the system were studied by Raman spectroscopy. It clearly showed that the orthorhombic distortion of the system increases with increasing Y concentration indicated by the shifting of Raman modes to higher wave number. All the Raman modes of the system harden with considerable decrease in the full width at half maximum (FWHM) as the temperature is lowered. The temperature dependence of the position of the modes and that of the FWHM could be fitted to an anharmonic model down to 100 K. At still lower temperatures, anomalous softening/hardening of the modes is observed to ride over the anharmonic variation. However, most of the modes exhibit an anomalous narrowing just below 100K. Anomalous hardening/softening of the modes along with anomalous narrowing in the full width at half maximum of the corresponding modes, establishes the presence of spin-phonon coupling in the present system. It is to be emphasized here that though spin-phonon coupling is not a prerequisite for a multiferroic compound, it is nevertheless present in most of the multiferroic materials. The observed deviations start much above the magnetic transition temperature  $T_{N1}^{Mn}$  revealing the spin correlations present even in the paramagnetic phase. Importantly, the  $B_{2g}(1)$  related to  $ab$ -plane exhibits anomalous softening for all x. Ab-initio calculations were carried out to find both the phonon dispersion and phonon density of states. It is observed that the Raman spectrum matches well with the calculated Phonon density of states. The Raman active modes were also calculated and the origin of specific Raman modes were identified with individual atomic contributions.

## Scope for future work

All the studies have been carried out on polycrystalline samples. As the physical properties of this class of materials are anisotropic, it would be better single crystals are used. It would give better understanding on the dielectric and vibrational properties. Neutron diffraction, an indispensable tool to study the magnetic structure and sublattice magnetization could not be employed on Gd-based compounds. This is due strong absorption of neutron by Gd. The element specific X-ray magnetic circular dichoric (XMCD) phenomenon offers an alternate method carry out such studies. It will be worthwhile to carryout XMCD studies across magnetic transition temperatures  $T_{N1}^{Mn}$ ,  $T_{N2}^{Mn}$  and  $T_N^{Gd}$ .

